TERNARY II-VI 1D NANOMATERIALS: SYNTHESIS, PROPERTIES AND APPLICATIONS

LU JUNPENG

(B. Sc, SHANDONG UNIVERSITY)

A THESIS SUBMITTED

FOR THE DEGREE OF DOCTOR OF PHILOSOPHY

DEPARTMENT OF PHYSICS

NATIONAL UNIVERSITY OF SINGAPORE

2013

DECLARATION

I hereby declare that this thesis is my original work and it has been written by me in its entirety. I have duly acknowledged all the sources of information which have been used in the thesis.

This thesis has also not been submitted for any degree in any university previously.

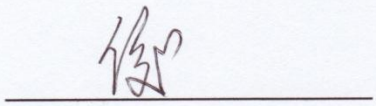

Lu Junpeng

3 August 2013

ACKNOWLEDGEMENTS

I would like to take this opportunity to acknowledge all the people who have kindly helped and encouraged me in the last four years. It would never be possible for me to complete this thesis without their generous assistance.

First and foremost, I would like to express my sincere gratitude to my supervisor Prof. Sow Chorng Haur for his patient guidance, support and encouragement. I have been motivated and inspired by him during the course of my Ph.D. I am extremely thankful to him for giving total freedom in selecting research projects and providing thoughtful suggestions. He guided me into the fantastic world of nanoscience and nanotechnologies. His expertise and integral view towards research lead us always walk in the front of nano-research frontiers. He always offered me high advice and encouragement every time when I came across failures or difficulties not only in my research but also in my daily life. He also reviewed and revised all my research manuscripts and this thesis with greatest diligence.

I am also grateful to Mr. Zheng Minrui who taught me many experimental skills and offered me numerous advice and suggestions during the course of my Ph.D. We almost spent every working day together over the last four years and have built up solid friendship. I am also grateful to Dr. Deng Suzi and Ms. Lim Xiaodai Sharon for their kind impartation in some experimental skills such as hydrothermal growth techniques and focused laser beam operation.

I also would like to thank others group members Mr. Lim Kim Yong, Dr. Binni Varghese, Mr. Yun Tao, Dr. Lim Zhi Han, Dr. Lee Kian Keat, and Ms. Loh

Pui Yee for giving me a lot of valuable suggestions and assistance on my research projects.

I also want to express my thanks to Dr. Zhang Xinhai for his inspiration and constant support. I am grateful to him for providing ultrafast research facilities which are essential to my project. Fruitfully discuss with him have helped me a lot for the successful completion of my thesis.

I am also grateful to Prof. Subodh Mhaisalkar, Dr. Nripan Mathews, and Dr. Sun Cheng at Nanyang Technological University for the successful collaboration at different stages of my study.

I would like to thank all technical staff in Physics department for their invaluable help. Especially, I would like to thank Ms. Foo Eng Tin, Mr. Chen Gin Seng, and Mr. Lim Geok Quee for extending help for assisting with lab suppliers and rectifying instrumental problems.

Personally, I would like to thank my family. I am grateful to my parents for raising me up and for the continuous support, encouragement and love. The love always gives me power and pushes me to work harder when I was depressed in difficulties. Finally, I would like to express my special thanks to my wife, Hongwei, who has been with me over the last seven years. As a partner both in life and in research, she offers me consistent understanding, care, support and love. Without her help, I could not complete the fundamental optical property study of the nanostructures. Thanks for the ultrafast spectroscopy measurements in research and thoughtful kindness in life. I wish all our dreams come true.

TABLE OF CONTENTS

ACKNOWLEDGEMENTS iii
TABLE OF CONTENTS v
ABSTRACT viii
LIST OF TABLES x
LIST OF FIGURES xi
Chapter 1 Introduction to Ternary II-VI Nanostructures 1
1.1 Introduction 1
1.2 Controlled synthesis of ternary II-VI 1D nanostructures 4
1.2.1 Vapor phase route 4
1.2.2 Liquid phase route 15
1.3 Physical Properties and Potential Applications of Ternary II-VI 1D Nanostructures 19
1.3.1 Electrical Properties and Potential Applications 19
1.3.2 Optical Properties and Potential Applications 22
1.3.3 Optoelectronic Applications 25
1.4 Objective and Scope of the Present Work 27
1.5 Organization of the Thesis 30
Chapter 2 Experimental Facilities and Techniques 31
2.1 Growth Technique 31
2.2 Characterization Tools and Techniques 32
2.2.1 Scanning Electron Microscopy (SEM) 33
2.2.2 Transmission Electron Microscopy (TEM) 33
2.2.3 X-Ray Diffraction (XRD) 34
2.2.4 X-Ray Photoelectron Spectroscopy (XPS) 35
2.3 Optical Spectrum Techniques 36
2.3.1 Raman Spectroscopy 36
2.3.2 Photoluminescence (PL) Spectroscopy 37
2.3.3 Terahertz Time-Domain Spectroscopy (THz-TDS) 38

2.3.4 Optical Pump-Terahertz Probe (OPTP) Spectroscopy 41
2.4 Device fabrication processes and characterization tools 43
2.5 Laser pruning technique 45
Chapter 3 Growth of Ternary II-VI 1D Nanostructures and Their Hybrids 47
3.1 Introduction 47
3.2 Experimental Method 51
3.3 Results and Discussions 54
3.3.1 Growth of CdS_xSe_{1-x} Nanobelts 54
3.3.2 Growth of ZnS_xSe_{1-x} Nanowires 59
3.3.3 Growth of Ternary Hybrid Nanostructures 63
3.4 Conclusions 68
Chapter 4 Fundamentals of Optical Properties in Ternary II-VI 1D Nanostructures 70
4.1 Introduction 70
4.2 Experimental Method 71
4.3 Results and Discussions 73
4.3.1 Exciton Complex 73
4.3.2 Complex photoconductivity 88
4.3.3 Phonons 94
4.4 Conclusions 102
Chapter 5 Applications of Ternary II-VI 1D Nanomaterials as FETs and Photodetectors 103
5.1 Introduction 103
5.2 Experimental Method 103
5.3 Results and Discussions 105
5.3.1 Field-Effect Transistors (FETs) 105
5.3.2 Photodetectors/sensors 116
5.4 Conclusions 121
Chapter 6 Direct Laser Pruning of CdS_xSe_{1-x} Nanobelts en Route to a Multicolored Pattern with Controlled Functionalities 122
6.1 Introduction 122
6.2 Experimental Method 123

6.3 Results and Discussions 124
6.4 Conclusions 141
Chapter 7 Conclusions and Future Works 143
7.1 Summary 143
7.1.1 Synthesis of Nanostructured Ternary Zinc and Cadmium Chalcogenides 143
7.1.2 Investigation of Optical Properties 144
7.1.3 Demonstration of Potential Applications 145
7.1.4 Modified Properties and Versatility 145
7.2 Further Works 146
7.2.1 Extension of Growth 146
7.2.2 Investigation of Optical Property and Potential Applications of Complex Nanostructures 146
7.2.3 Extension of the Modification by Laser Pruning 147
BIBLIOGRAPHY 149
APPENDIX 167

ABSTRACT

Ternary alloyed one-dimensional (1D) nanostructures from II-VI semiconductors are of prime interest due to their tunable band gaps with strong promise for augmented multifunctional optoelectronic devices with flexible novel performance. However, due to technical difficulty caused by the complexity of multicomponent phase diagrams, only a few reports have presented the creation of such 1D nanostructures. The common challenge in the synthesis of alloyed 1D nanostructures lies in achieving desired composition with highly uniform stoichiometry, which is largely attributed to the effect of temperature gradient. The aim of this thesis was to develop a simple and yet effective one-step approach with a specially designed substrate holder to synthesize single crystalline ternary 1D nanonstructures with uniform chemical stoichiometry and accurately controllable compositions ($0 \leq x \leq 1$). Based on this, the corresponding optical properties and optoelectronic applications were also systematically studied.

The micro-morphologies and detailed structures of these nanobelts were studied by scanning electron microscopy, high resolution transmission electron microscopy, X-ray diffraction, micro-Raman spectra and energy-dispersive X-ray spectroscopy. The elements distribution was explored using elemental mapping. Ultrafast optical spectroscopy techniques were employed to probe the fundamentals of optical properties. Moreover, large-scale network field effect transistors (FET) based on these nanostructures were fabricated through a lithography-free method.

All the characteristic results indicate that the nanobelts exhibit high quality single crystalline wurtzite structure. Photoluminescence spectra obtained from these nanostructrues show that the near-band-edge energy can be systematically modulated in the range of UV to NIR. Functional Electrical application of these nanobelts was achieved by a fabricated nanonet FET. Lower threshold voltage and much higher ON-OFF ratio than binary nanostructures based FET were obtained. These nanonet FETs also show potential as photosensor with rapid photoelectrical response to light illuminations. The good performance shown by the ternary nanostructure devices indicates their great potential in nanoscaled photoelectronics applications.

Overall, the growth method described in our work is demonstrated a proper strategy for ternary 1D nanonstructures synthesis with uniform chemical stoichiometry and accurately controllable compositions. The achievement of uniform ternary products will greatly promote the structural characterization of multiplex alloys by excluding the impact of composition gradient. The higher photoconductivity revealed by the fundamental optical property study would facilitate the possibility for implementation of ternary nanobelts in optoelectric devices. The reported approach is expected to be suitable to other ternary compounds.

LIST OF TABLES

Table 5.1 Summary of Device Behavior at Different Light Intensity Illumination 113

LIST OF FIGURES

Figure 1.1 Schematic of VLS and VS synthesis processes. 13

Figure 2.1 Schematic diagram and photo image of horizontal tube furnace in our lab. 32

Figure 2.2 Schematic diagram of Bragg diffraction. 35

Figure 2.3 Schematic diagram of micro-Raman spectroscopy. 37

Figure 2.4 Schematic diagram of PL spectroscopy. 38

Figure 2.5 Schematic diagram of THz-TDS. 39

Figure 2.6 (a) Schematic diagram of OPTP set-up. (b) Schematic illustration of the photoexcitation effect on the transmission of THz pulse. 42

Figure 2.7 (a) Schematic of the direct contact transfer process to fabricate aligned nanowire/belt networks. (b) Illustration of the process of fabrication of networks on patterned substrate. 44

Figure 2.8 Optical photo picture of the home-built contact transfer set-up. 45

Figure 2.9 Schematic illustration of the focused laser beam set-up. 46

Figure 3.1 Schematic diagram of VLS growth process. 50

Figure 3.2 (a) Schematic diagram of alloyed nanobelts growth reactor set-up. (b) Nanobelts grown on horizontally placed substrate showing different colors from left to right, indicating wide composition range in the alloyed compounds. (c) Design model of substrate holder. (d) Optical images of five samples with different composition grown on the substrates. Sulphur concentration decreasing from left to right. 52

Figure 3.3 (a)-(e) SEM images of five CdS_xSe_{1-x} samples with different compositions. The scale bar is 2 μm. (f)-(j) Respective EDS of these as-synthesized CdS_xSe_{1-x} nanobelts. x value decreasing from 1 to 0 from (f) to (j). (k)-(o) Elemental mappings of these samples. Cd, S and Se elements distributions are homogeneous. 56

Figure 3.4 TEM images of CdS_xSe_{1-x} with x values about (a) 0.8 and (b) 0.2. Inserts are their corresponding SAED patterns. HRTEM images of CdS_xSe_{1-x} nanobelts with x values of (c) 0.8 and (d) 0.2. 58

Figure 3.5 Normalized XRD patterns of CdS_xSe_{1-x} nanobelts ($0 \leqslant x \leqslant 1$). Spectra (a) and (e) for CdS and CdSe respectively. Spectra (b)-(d) for CdS_xSe_{1-x} samples with different x values. 59

Figure 3.6 SEM images of two ZnS_xSe_{1-x} samples with different compositions (a) $x = 0.38$. (b) $x = 0.18$. EDS spectra of (c) $ZnS_{0.38}Se_{0.62}$ and (d) $ZnS_{0.18}Se_{0.82}$. (e) and (f) the corresponding HRTEM of two samples. Inserts are their SAED patterns. Optical images of (g) uniform sample and (h) non-uniform sample..... 61

Figure 3.7 Normalized XRD patterns of ZnS_xSe_{1-x} nanowires ($0 \leqslant x \leqslant 1$). Spectra (a) and (f) for ZnS and ZnSe respectively. Spectra (b)-(e) for ZnS_xSe_{1-x} samples with different x values. 62

Figure 3.8 SEM images of (a) ZnO and (b) ZnO/CdS_xSe_{1-x} nanowire arrays, insert of (b) shows the high magnification SEM image. Low resolution TEM images of ZnO/CdS_xSe_{1-x} nanowires arrays with (c) thicker shell and (d) thinner shell. HRTEM images of (e) selected area in (c), and (f) selected area in (d). Inserts of (f) show the atomic resolution of the ZnO core and CdS_xSe_{1-x} shell. 64

Figure 3.9 EDX mapping elemental line scanning profile of the ZnO/CdS_xSe_{1-x} core/shell nanowire. 65

Figure 3.10 (a) Schematic diagram of special designed source-movable tube furnace. (b) Fluorescence microscopy image of composition gradient CdS_xSe_{1-x} nanowires. 68

Figure 4.1 Recombination processes in semiconductors. (a) Band-to-band recombination. (b) Band-to-acceptor transition. (c) Donor-to-valence transition. (d) Donor-to-acceptor-pair transition. (e) Recombination *via* a deep center. (f) Non-radiative recombination *via* an intermediate state. (g) Band-to-band Auger recombination. 74

Figure 4.2 (a) Band gap engineering of ternary semiconductors. (b) PL spectra of CdS_xSe_{1-x} nanobelts of different compositions. (c) Band gap energy as a function of composition. 77

Figure 4.3 (a) Normalized PL spectra of CdS_xSe_{1-x} nanobelts at 300 K (up) and 30 K (down), respectively. (b) Temperature-dependent PL spectra of $CdS_{0.65}Se_{0.258}$ nanobelts from 5 K to 300 K..... 79

Figure 4.4 Time-resolved PL spectra with fits of five CdS_xSe_{1-x} nanobelt samples at different temperature. 82

Figure 4.5 THz frequency regime in electromagnetic spectrum..... 84

Figure 4.6 Excitation fluence dependence of time-dependent differential THz transmission for (a) CdS and (b) CdS_xSe_{1-x} nanobelts. The solid lines are best exponential fitting results..... 85

Figure 4.7 (a) Fast decay time τ_1 as a function of photocarrier density. (b) $\Delta T/T_o$ at $t = 300$ ps as a function of excitation fluence. 87

Figure 4.8 Time-dependent THz pulses transmitted through (a) CdS and (b) CdS_xSe_{1-x} nanobelts. The black and blue curves represent the transmitted THz pulses before and after photoexcitation, respectively. 90

Figure 4.9 Complex photoconductivity of six samples (x= (a) 1, (b) 0.87, (c) 0.75, (d) 0.65, (e) 0.29, and (f) 0, respectively) recorded at t = 3.5 ps. The solid lines are Drude-Smith fitting curves. 92

Figure 4.10 (a) Real part of photoconductivity at 2 THz plotted as a function of composition. (b) Photocarrier density (ΔN) and photocarrier mobility plotted as a function of composition. 94

Figure 4.11 Raman spectra of (a)-(d) CdS_xSe_{1-x} nanobelts, and (e)-(f) ZnS_xSe_{1-x} nanowires. 98

Figure 4.12 Low-frequency phonon resonance in ternary CdS_xS_{1-x} nanobelts probed by THz-TDS under equilibrium and non-equilibrium conditions. 101

Figure 5.1 (a) Schematic illustration of a single nanowire FET. (b) and (c) FET performance characteristics of CdS_xSe_{1-x} single nanobelt FET (reprinted from Ref. [136] by permission of the American Chemical Society). 107

Figure 5.2 (a) Schematic illustration of the nano-network FET fabrication process. (b) SEM image and schematic (insert) of the parallel aligned CdS_xSe_{1-x} nanonet-FET. I_{ds}-V_{ds} output curves of (c) $CdS_{0.8}Se_{0.2}$ and (e) $CdS_{0.65}Se_{0.35}$ at V_{gs} from 5 V to 30 V. Transfer characteristics of (d) $CdS_{0.8}Se_{0.2}$ and (f) $CdS_{0.65}Se_{0.35}$ under different light intensity. 110

Figure 5.3 I_{ds}-V_{ds} output curves of (a) CdS and (c) CdSe nanobelt networks FET at V_{gs} from 5 V to 30 V. Transfer characteristics of (b) CdS and (d) CdSe under different light intensity illumination. 112

Figure 5.4 (a) SEM image and schematic illustration (insert) of the horizontal aligned ZnS_xSe_{1-x} nanowire network-FET. (b) Typical I-V measurement of the ZnS, ZnSe, and $ZnS_{0.42}Se_{0.58}$ nanowire networks. (c) I_{ds}-V_{ds} output curves of $ZnS_{0.42}Se_{0.58}$ network-FET at V_{gs} from 0 V to 40 V. 115

Figure 5.5 (a) Schematic diagram of time response measurement setup. (b) Spectrum of the light source. 118

Figure 5.6 Photosensitive behaviors of (a) $CdS_{0.8}Se_{0.2}$, (b) $CdS_{0.65}Se_{0.35}$, (c) CdS, and (d) CdSe nanonets. 119

Figure 5.7 Photosensitive behavior of $ZnS_{0.42}Se_{0.58}$ nanowire network. 120

Figure 6.1 (a) Schematic of the optical microscope-focused laser beam set-up for micro-patterning. (b) SEM and (c) fluorescence microscopy images of a “Dragon” patterned *via* a 660 nm laser with a power of 30 mW. 126

Figure 6.2 (a) (*i*) SEM, (*ii*) optical microscope and (*iii*) fluorescence microscope images of a "Flower" patterned on $CdS_{0.75}Se_{0.25}$ nanobelts film *via* a 660 nm laser with a power of 20 mW. (b) (*i*) SEM, (*ii*) optical microscope and (*iii*) fluorescence microscope images of a multiple boxes patterned on $CdS_{0.79}Se_{0.21}$ nanobelts film. Multi-colored pattern with four different colors obtained by carefully control the laser power. 127

Figure 6.3 (a) SEM images of five micro-squares patterned on $CdS_{0.71}Se_{0.29}$ nanobelts *via* different laser powers. [V (30 mW), IV (25 mW), III (20 mW), II (15 mW) and I (10 mW)]. (b) Corresponding fluorescence images of five micro-squares patterned, I to V *versus* the laser power from 10 to 30 mW. (c) PL spectra of as-grown region and three representative patterned micro-squares. (d) PL peak position shifts as a function of laser power. 129

Figure 6.4 (a) SEM image of the micro-channels pattern. Magnified view in insert shows two distinct 1μm channels separated by a width of 10 μm. (b) A cross sectional SEM image of a channel reveals the high resolution of the focused laser beam technique. (c and d) Magnified images of the boundary of laser modified region (left) with pristine region (right). The powers of the laser used were 30 mW and 10 mW respectively. (e) and (f) Cross sectional SEM views of the samples shown in (c) and (d) respectively. 131

Figure 6.5 EDX spectra of $CdS_{0.69}Se_{0.31}$ nanobelts (a) before and (b) after laser modification. XPS spectra of these nanobelts (c) before and (d) after laser modification. XRD patterns of $CdS_{0.69}Se_{0.31}$ nanobelts (e) before and (f) after laser modification. 134

Figure 6.6 (a) PL spectra of pristine sample $CdS_{0.75}Se_{0.25}$ (blue curve) and sample after laser pruned in helium environment (red curve). (b) PL spectra of an as-grown $CdS_{0.75}Se_{0.25}$ sample (yellow curve) and three other samples after annealing with increasing temperatures of 650^{o}C, 850^{o}C and 1050^{o}C for 0.5 minute. Insets show the corresponding images of the samples captured by a fluorescence microscope. 136

Figure 6.7 (a) Schematic of the set-up for the studies on acid-exposure . PL spectra of (b) pristine and (c) pruned region before and after acid exposure. Fluorescence microscope images of a micro-Tai Chi pattern (d) before and (e) after acid exposure. 138

Figure 6.8 (a) Typical *I—V* curves acquired with two-probe measurements for the pristine nanobelts film and its laser pruned counterpart. Typical *I—V* curves under 660 nm laser irradiation of (b) pristine and (c) pruned nanobelts film. Typical *I—V* curves under 808 nm laser irradiation of (d) pristine and (e) pruned nanobelts film. (f) On/off photocurrent response of pristine nanobelts (pink curve) and laser pruned nanobelts (green curve) to 660 nm laser. (g) On/off photocurrent response of pristine nanobelts (light blue curve) and laser pruned nanobelts (brown curve) to 808 nm laser. 141

Chapter 1

Introduction to Ternary II-VI Nanostructures

1.1 Introduction

Quasi-one-dimensional (1D) semiconductor nanowires and nanobelts have attracted great attention due to their potential in the fabrication of nano-scaled novel electronic, photoelectronic and electromechanical devices. These devices include field-effect transistors[1], photodetectors[2], solar cells[3], and piezo nanogenerators[4, 5]. Numerous groundbreaking and fascinating advances have been demonstrated on the potential applications of 1D nanostructure systems. This is in part due to the fact that these nanowires manifest various size- and morphology-dependent intrinsic properties where the relevance of quantum confinement effects is greater.[6-11] Band gap engineering is an attractive technique for the control of optical properties of semiconductor en route to potential applications. Utilizing the quantum confinement effect, altering the band gap by controlling the dimension of materials is a common approach. In particular, this approach has been favored in the studies of one dimensional (1D) semiconductor nanomaterials because of the ease in achieving confinement in the other two-dimension for these nanomaterials. Due to the rapid development of modern growth techniques, such as chemical vapor deposition, molecular beam epitaxy and hydrothermal approach, precise control of the size of 1D materials is now routinely achieved.[12] Through these methods, nanomaterials with unique optical and electrical properties can be synthesized.[13-16] However, for some applications, extreme reduction of the

diameter of nanowires may not be desirable. For example, in nano-laser application,[17-19] one may encounter the disappearance of Fabry-Perot cavity for ultra-thin nanowires as reasonably large dimension is required to avoid the diffraction limit. Thus, alternative approaches to modify and control the band gap of a semiconductor material are clearly desirable. For this purpose, band gap engineering by tuning the constituent composition of certain semiconductor alloys has been reported.[20, 21]

II-VI compound semiconductors, especially cadmium chalcogenides: CdS, CdSe, CdTe and zinc chalcogenides: ZnO, ZnS, ZnSe, ZnTe, are among a typical class of materials that has been intensively investigated in the field of 1D nanostructures.[22-28] These materials are recognized with great promise due to their high light sensitivity and quantum efficiency.[22] In addition, the range of their wide direct band gap indicates the possibility to fabricate optoelectronic devices to response to various electromagnetic spectrums. Nevertheless, the response range and flexibility of these devices are limited by the distinct band gap for individual material. Therefore, alloying of 1D semiconductors with various band gaps is an emerging method to achieve precisely control and continuously tuneable band gaps. Meanwhile, techniques to prepare high quality ternary 1D nanostructures with good control and reproducibility have been made achievable by fastidious investigations in the research field within the recent years. Great progress within the last decade in the field of alloyed nanostructures, as an important part in the cutting-edge nanotechnology, has potentiated the expectation of the vital function that ternary 1D nanostructures would possibly hold in the future. Ternary alloyed

nanostructures based on II-VI compound semiconductors have been prepared as an emerging building block of ultra-broad wavelength tuneable nanolasers, color engineered light devices and displays, full spectrum solar cells and multispectral photodetectors.[29] On the strength of good crystallinity, unique properties and possible device applications, this chapter will therefore provide a comprehensive summary on the preparation techniques and material systems of ternary alloyed II-VI nanostructures. This is followed by fundamental of optical and photoelectrical properties relevant to ternary II-VI materials, and their promising potential in photonics and optoelectronics applications.

In this chapter, an overview of the research activities on II-VI compound semiconductor nanostructures is presented. The content is organized as following. After this brief introduction, various established techniques for II-VI 1D nanostructure synthesis are described. The relative advantages and shortcomings of each synthesis methods are highlighted. Following this, the electrical and optical properties of II-VI compound nanostructures are discussed. The unique properties displayed by the ternary alloys are emphasized. In addition, the potential applications resulted from the properties of ternary II-VI nanostructures are also displayed. Subsequently, the scope and objectives of the work presented in the thesis are outlined. This chapter ends with a short note on the organization of the rest of the thesis.

1.2 Controlled synthesis of ternary II-VI 1D nanostructures

Since the discovery of carbon nanotube in 1991, the amazing physical properties exhibited by this 1D nanostructure stimulated interest on semiconductor nanomaterials as well. In the last two decades, abundant methods have been developed to synthesize II-VI nanostructures with accurate control on their crystal structure, size, shape, dimensionality, and chemical composition. According to the physical form of the medium in which the synthesis process is carried out, the growth techniques can be broadly classified as vapor phase growth and liquid phase growth. In the following section, we will review various synthesis techniques with special emphasis on the recent developments in the research field.

1.2.1 Vapor phase route

In vapor phase route, nanostructures are synthesized from precursor reactants in gaseous state. By vapor phase techniques, contamination free nanostructures with high crystalline quality can be synthesized. The major merit of the vapor phase route is the feasibility of organizing and manipulating the products during their growth processes. In addition, complex and hybrid nanostructures with multiple functionalities can be facilitated by these vapor phase growth techniques. The much needed impurity doping or polybasic alloying, which is essential for various nano-scaled device fabrications, can be easily realized in these vapor growth methods. The vapor phase growth techniques are customary further divided in terms of governing mechanisms. Different vapor

phase growth approaches utilized for the synthesis of II-VI compound semiconductor nanostructures are elaborated in the following section.

i. Vapor Liquid Solid (VLS) route

The growth of 1D nanostructures which is so-called nanowhiskers from gaseous state reactants has been developed for more than 50 years.[30, 31] The metal film coated on substrates will melt and form small droplets when annealed above a certain temperature. These small droplets act as catalyst for the growth of nanostructures. Vapor species of the materials will adsorb on the surface of the metal droplet due to the high sticking coefficient of liquid. An eutectic liquid alloy forms and it facilitates the diffusion of the adsorbed species from surface to bulk of the metal droplet. When the adsorption is supersaturated, nucleation occurs due to the phase segregation at the droplet-substrate interface. Subsequent 1D growth occurs as further gas molecules adsorb into the nuclei. The metal droplet facilitates the 1D axial growth at the liquid alloy and solid interface and suppresses the growth in other directions due to the higher energy required than that of the crystal step growth. [32] The metal droplets will solidify to form a nanoparticle and remain on the tip of the resultant 1D nanostructure during the cooling progress, which is an assertive evidence of the VLS growth mechanism.

The diameter of the 1D nanostructures is largely depended on the size of the droplet. The minimum equilibrium size of the metal droplet can be calculated as following according to the thermodynamic consideration.[33, 34]

$$r = \frac{2V_l\sigma_{lv}}{k_bT\ln s} \tag{0.1}$$

where V_l is the atom volume in liquid, σ_{lv} is the vapor-liquid surface energy, T is the temperature, and s is the degree of adsorption supersaturation. The equation limits the achievable size of the 1D nanostructures synthesized by VLS approach.

Chemical vapor deposition (CVD) is a common technique that can be utilized to synthesize 1D nanostructures by VLS route. Horizontal tube furnace with vacuum sealed quartz tube is usually employed as the reaction chamber. A mechanical pump is connected to one end of the quartz tube to supply the vacuum condition whilst the other end of the tube is connected to mass flow controllers with gas sources. The substrates coated with metal catalyst film (normally, Au) are placed at the downstream zone of the tube chamber. After the temperature ramping, the vapor phase precursor species are carried at optimal flow rate towards the substrate. The pressure inside the quartz tube is controlled and maintained by the gas flow rate.

The precursor vapor supply is an important aspect in the VLS based 1D nanostructure synthesis. In the oxide nanostructures synthesis, the reactant vapors can be produced through thermal evaporating the corresponding metals in the presence of oxygen.[35-38] Yang and co-workers initiate similar method to successfully synthesize II-VI compound oxide (ZnO nanowires) by VLS route.[39, 40] They produce the reactant vapors by carbothermal reduction of ZnO powder. The Zn vapor was transported to the lower temperature zone where the oxygen gas was provided. This is a proper method to synthesize the oxide nanowires with

high single crystalline quality and small diameters. However, this method is limited in the synthesis of other II-VI chalcogenides compounds because the flow of S, Se and Te gases is not as easily controlled as oxygen supply. Therefore, direct thermal evaporating the solid source powders with same chemical composition of the product nanostructures is the most commonly used method to synthesize II-VI chalcogenides 1D nanostructures. A number of researchers have employed the direct thermal evaporation assisted VLS method to synthesis II-VI 1D nanostructures of CdS, CdSe, ZnS, ZnSe and ZnTe.[41-45] Due to the requirement of desirable nanomaterials with tuneable band gaps in the optoelectronic applications, ternary II-VI 1D nanostructures were thus developed and synthesized by Pan and co-workers employing the VLS growth method with CVD technique.[46] Through this approach, high quality single crystalline CdS_xSe_{1-x} nanowires can be obtained. Other ternary II-VI 1D nanostructures of $Zn_xCd_{1-x}S/Se$ and $Mn_xCd_{1-x}S$ were also synthesized using the similar routes.[47-49] A special case among the thermal evaporation assisted VLS methods called self-catalytic VLS occurs when the constituent metal of the target itself functions as the catalyst, such as Zn in the synthesis of zinc chalocogenides. This can eliminate the unintentional contamination caused by the foreign catalyst. Many binary II-VI compound semiconductor nanostructures such as zinc chalocogenides (ZnO and ZnSe nanowires),[50, 51] cadmium chalocogenides (CdS, CdSe and CdTe nanowires),[52] and lead chalocogenides (PbS and PbSe nanowires)[53, 54] have been produced by the self-catalytic assisted VLS route. Most recently, Xiong and co-workers extended this method in the synthesis of ternary II-VI 1D

nanostructures.[55] They successfully prepared the vertically aligned CdS_xSe_{1-x} nanowire arrays on mica substrate due to the epitaxial growth.

Laser ablation is another effective approach for the production of reactant vapor. The laser ablation assisted VLS technique was first developed by Lieber's group.[56] In the laser assisted VLS route, the vapors are produced by evaporating the target with the same chemical composition of the product using a high power intensity laser beam. Compared with the direct thermal evaporation, the laser ablation can evaporate the solid sources much faster and supply the vapor reactants in a shorter time. The laser ablation assisted VLS approach has been employed for the synthesis of II-VI compound semiconductor nanostructures including ZnO nanowires,[57] ZnS nanowires,[58] ZnSe nanowires[59] and CdS nanowires[60]. On top of the binary nanostructure synthesis, Lee and co-works also reported the synthesis of ternary CdS_xSe_{1-x} nanoribbons using the laser ablation assisted VLS approach.[61, 62]

Different from the typical horizontal tube furnace, metal organic chemical vapor deposition (MOCVD) is a deposition technique in which at least one of the precursor gases is metallic atom attached to an organic compound with sufficiently high vapor pressure. The precursor gas undergoes pyrolytic reactions in a chamber at elevated temperatures, where the metallic atom is deposited on the substrate while the organic compound is removed from the reaction chamber. MOCVD grown nanostructures by VLS route have also been demonstrated in synthesis of II-VI compound semiconductor nanowires.[63-67] For the ternary II-VI 1D nanostructures synthesis, Liang and co-workers reported the epitaxial growth

of vertically aligned ZnS_xSe_{1-x} alloy nanowire arrays on GaAs (111)B substrate using MOCVD technique.[68] Compared to typical horizontal tube furnace, MOCVD can accomplish mass production due to the high intake of precursor vapor and it is possible to use large area substrates to harvest large scale nanostructures. Nevertheless, the use of complex chemistry will increase the production cost, whilst the use of highly toxic precursor gases is also an intractable issue.

The main merit of the VLS route is that it facilitates single crystalline nanostructures with high quality. In most occasions, the as-grown nanostructures are dislocation free by the VLS method. The dimensionality and morphology of the synthesized nanostructures highly depend on the thickness of the catalyst, pressure, evaporation and deposition temperature, carrier gas speed, and duration time.[37, 69, 70] In addition, the VLS route has the ability of flexibly manipulating and positioning the nanostructures by controlling and patterning the catalyst location.[71] However, as mentioned above, the existence of metal catalyst on the tip of the nanowires could affect the physical and chemical properties of the ternary nanostructures. In order to avoid the influence of the catalyst, catalyst-free growth method in gaseous reaction media were developed and employed for II-VI nanostructures.

ii. Vapor-Solid (VS) route

VS growth is often classified into the growth of 1D nanomaterials without using of any catalyst. It is a spontaneous condensation conversion process of

vapor into solid material induced by the decrease in supersaturation or the decrease in Gibbs free energy from crystallization.[25] Competition between kinetics of crystal growth and surface energy minimization determines the prevailing morphology during the VS growth process.[72] When the vapor species condensed on the substrate, the anion-cation adatoms form a small nucleus while maintaining the structural symmetry and balance of local charge. Due to the difference in the kinetic parameters of each crystal plane, anisotropic growth will be facilitated and the nucleus will guide well-defined, low index crystallographic faces.[26] The probability of the nuclei formation during the VS process can be described as,[73]

$$P_n = A\exp\left(\frac{-\pi\sigma^2}{k_B{}^2T^2\ln(p/p_o)}\right) \qquad (0.2)$$

where A is constant, σ is surface energy, k_B is Boltzmann constant, T is temperature, p is the pressure and p_o is the equilibrium vapor pressure.

Similar to VLS route, the typical horizontal tube furnace based CVD technique can be utilized for nanostructure synthesis *via* VS approach. The solid source powders are normally located at the upstream of the tube chamber. The substrates are placed downstream where the temperature is lower. The respective source powders are first thermal evaporated at high temperature to form reactant gases which are then transported to the substrates by carrier gas. The resultant morphology of the products is greatly affected by the source material, substrate temperature, carrier gas flow rate, and processing pressure.[74-81] Wang and co-workers initiated the VS approach to successfully synthesize metal oxides

nanobelts by direct evaporating respective metal oxide powders on silicon substrate without metal catalyst.[74] In addition to synthesizing metal oxide nanostructures, II-VI compound semiconductors including ZnO, ZnS and CdS nanowires were also synthesized using the VS route.[82-84]

During the VS growth process, when the temperature is sufficiently high, accumulation of arriving atoms onto the smooth low-index surface is hampered by the high diffusivity of the adatoms, thus enable the expansion of surface area as more atoms stick on the rougher growth face to form nanoribbons or other complex morphologies. Therefore, the versatility of fabrication complex hybrid nanostructures through VS approach has been established. Such property facilitates the research activities towards achieving integration of nanostructure assembly with high density. For example, II-VI nanostructures of ZnO comb-like morphology has been reported following the VS route.[85] More complicated nanostructures such as hierarchical saw-like ZnS nanowire-ZnO nanobelt heterostructures were prepared by Shen and co-workers.[86] They used SnS and Zn powders as the source precursors. The ZnO was first deposited and formed the uniform nanobelts on the support substrates. Then ZnS was deposited and regrew on the edge of the ZnO nanobelt to form the "sawtooth". For the ternary II-VI 1D nanostructure synthesis, Hark and co-workers demonstrated the tetrapod-like ZnS_xSe_{1-x} nanowires synthesis employing the VS growth method with a horizontal tube furnace.[87] They used Zn powder as the group II precursor material placed at the center of the tube furnace and the mixture of Se and SeS_2 powder (mass ratio of 3:1) was employed as the group VI source material which was put

at the upstream of the furnace. Most recently, Park and co-workers obtained the vertically aligned radial ZnO-CdS_xSe_{1-x} and TiO_2-CdS_xSe_{1-x} heterostructures by coating CdS_xSe_{1-x} outerlayer on ZnO or TiO_2 nanowires *via* a VL route.[88] Firstly, ZnO or TiO_2 nanowires were synthesized using a horizontal tube furnace and the CdS_xSe_{1-x} shell was deposited in a second vapor deposition step. To fabricate vertical nanostructure arrays, lattice matching foreign substrates can be chosen to support the heteroepitaxial growth. Alternatively, seed layers can be deposited on the substrate to facilitate the homoepitaxial growth.[89, 90] Moreover, modification of substrate surface roughness can also effectively promote the alignment of nanostructures synthesized *via* VS route.[91] The schematic illustration of VLS and VS growth processes is shown in Figure 1.1.

However, the exact physical mechanism of the anisotropic growth of nanostructures by VL approach is confusing until now. The growth direction of the nanostructures largely depends on the anisotropic growth rates of different crystal surfaces. Certain crystal surface with relatively higher energy facilities the faster growth to minimize the total energy and resulting in the anisotropy of the growth. In addition to the influence of the surface energy, the existence of defects such as screw dislocations can also promote the nanostructure growth in VS process. As discussed above, the vertically aligned nanostructure arrays will extend the application area of the materials and facilitate the integration in the nanostructure device assembly. Nevertheless, the synthesis of vertical nanostructure arrays *via* both the VS and VLS routes are highly determined by the epitaxial relationship with the substrates. Therefore, growth technique which can

direct the growth was developed and employed to synthesize the 1D nanostructures with vertical alignment.

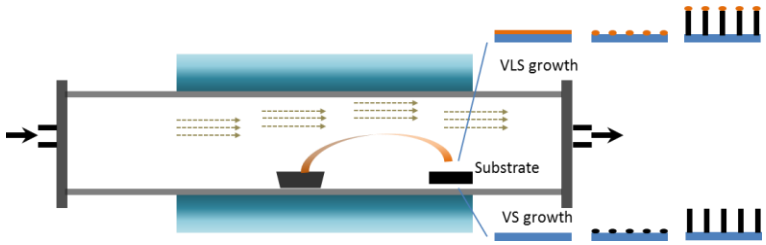

Figure 1.1 Schematic of VLS and VS synthesis processes.

iii. Template Assisted route

Taking advantage of proper templates to guide the growth alignment is a versatile approach for monodisperse nanostructure synthesis. Under the assistance of templates, various compositions of materials could be constructed at the nanoscale. Either the positive templates (such as CNTs and nanowires) or negative templates (such as anodic alumina (AAO) and track etched polycarbonate films) can work as scaffolds to guide the crystal growth direction.

The early research efforts on the synthesis of nanostructures *via* template assisted route focused on positive synthesis use CNTs as the template.[92] In this method, first vertically aligned CNTs were prepared. Then the desired materials were coated on the surface of the CNTs. The resultant nanostructures were obtained by removal of the CNTs *via* chemical etching or thermal heating. Besides CNTs, other 1D nanostructures were also employed as the positive template to synthesize various aligned nanostructures. For example the vertically oriented MgO nanowire has been reported as the template to synthesize titanate

and superconducting YBCO nanostructure by pulsed laser deposition.[37, 93] Recently, vertically aligned ZnO nanowire arrays were employed as the template to synthesize II-VI compound semiconductor nanotubes. Vertically aligned ZnS nanotube arrays were synthesized by this method.[94] The vertically aligned ZnO-ZnS core-shell nanowire arrays were prepared by deposition ZnS on the ZnO template. Then the ZnO core was removed by 20 wt% acetic acid solution to form ZnS nanotube arrays. Furthermore, the nanowire templates can be effectively employed for the synthesis of complicated ternary nanostructures. ZnO was coated on the well aligned β-Ga_2O_3 template by MOCVD and subsequently annealed in O_2 atmosphere, after which ternary single crystalline $ZnGa_2O_4$ nanowires can be created.[95] Similarly, ternary Zn_2TiO_4 nanowires can by synthesized via coating Ti on ZnO nanowire template and subsequent annealing at low vacuum condition.[96] Besides the formation of ternary nanowires, the ternary nanotube can be prepared by the similar template method. For example, coating Al_2O_3 on ZnO nanowire template by ALD technique and annealing the core-shell structure will produce ternary $ZnAl_2O_4$ nanotubes due to nanoscale Kirkendall effect.[97]

By vapor phase techniques, contamination free nanostructures with high crystalline quality can be synthesized. The major merit of the vapor phase route is the feasibility of organizing and manipulating the products during their growth processes. In addition, complex and hybrid nanostructures with multiple functionalities can be facilitated by these vapor phase growth techniques. The much needed impurity doping or polybasic alloying, which is essential for various

nano-scaled device fabrications, can be easily realized in these vapor growth methods. Nevertheless, due to the high growth temperature of the vapor growth routes and the high dependence of the chemical composition on the deposition temperature, the low temperature growth techniques are desirable for the ternary nanostructure synthesis.

1.2.2 Liquid phase route

II-VI compound semiconductor nanostructures with controlled morphology, size and dimensionality can be created by liquid phase methods in the solution using relatively simple equipment. In liquid phase route, the precursors are dispersed or dissolved in appropriate solvents. The nanostructure nucleation and growth are largely determined by the pH value, and temperature. Under the effect of nano entities suitable surfactants on the large surface energy, the nanostructure growth can be stabilized and directed. The morphology and shape of the products can be controlled by properly optimize the growth parameters and choosing suitable surfactants to direct the crystal growth. The more precise control of the growth direction can be realized by the template assisted solution method. In this method, the crystal growth direction is confined inside the nanopores or channels of the negative template. Solution phase synthesis methods exhibit many advantages as compared to VS and VLS techniques, such as reasonable low temperature (< 250 ºC) and low cost, scalability, and ease of handling. Therefore, solution synthesis methods facilitate a greater choice of substrates.[98] In the following sections, a brief overview on these techniques will be presented.

i. Solution-Liquid-Solid route

Solution-liquid-solid (SLS) technique is a typical solution synthesis method of crystalline semiconductor 1D nanostructures. Different from the vapor phase methods, the precursors are transported through the solution rather than a vapor phase,[99] but the entire growth process is analogous to that of VLS technique. In the SLS synthetic progress, organometallic precursors are utilized to supply desired species to an organic solvent, and a metal with low melting point acts as the catalyst. The increased solution temperature facilitates the formation of liquid-metal droplets, which catalyze the disassembly of the precursors. The desired elements dissolve into the droplets until supersaturation is reached. Then nucleation occurs and facilitates the growth of 1D nanostructures. The II-VI compound semiconductor 1D nanostructures synthesized by SLS route include ZnO nanowires,[100] diameter-controlled CdSe quantum wire,[101] CdTe and ZnTe nanowires,[102, 103] CdSe and PbSe branched-wire structures.[104] In addition, the SLS growth method has also been demonstrated for ternary II-VI 1D nanostructures of PbS_xSe_{1-x} nanowires. Kuno and co-workers have synthesized high-quality PbS_xSe_{1-x} (x = 0.23, 0.39, 0.49, 0.69, and 0.9) nanowires using SLS method with $Pb(S_2CNEt_2)_2$ and $Pb((SePPr_2)_2N)_2$ as single-source precursors.[105] These nanowires exhibited well confined diameters grown along <002> direction and with an underlying rock salt crystal structure.

ii. Hydrothermal route

Hydrothermal route is a method of synthesis nanostructures using closed-system in hot water under high pressure. The synthesis process is produced in an apparatus consisting of a steel pressure vessel called autoclave, in which the solution is applied and the physical and chemical processes are performed. A gradient of temperature is supplied by a commercial oven so that the high pressure can be generated inside the closed autoclave. The possible merits of the hydrothermal route over other types of liquid growth methods include the ability to synthesize nanostructures which are not stable near the melting point. On top of this, nanostructures with high vapor pressure near their melting points can also be synthesized by the hydrothermal route. The hydrothermal method is also particularly suitable for the large volume growth of good-quality nanostructures while maintaining good control over their composition. The main disadvantage of the hydrothermal growth method is the underlying danger caused by the high pressure.

Most of the zinc chalcogenides and cadmium chalcogenides nanostructures including ZnO nanowires,[106] ZnS nanowires,[107] ZnTe nanocrystals,[108] CdS nanowires,[109] CdSe nanowires[110] and CdTe nanowires[111] have been synthesized *via* the hydrothermal approach. Moreover, the effective hydrothermal method has been extended to synthesize the ternary II-VI 1D nanostructures. The growth of ternary $Zn_{1-x}Mn_xO$ nanowires[112] and Mn doped ZnSe nanowires[113] have been demonstrated using hydrothermal route.

iii. Template Assisted Liquid Phase Route

Filling of nanopores/channels of the negative templates *via* the solution based techniques is effective approach to synthesize II-VI compound semiconductor nanostructures. The template can be subsequently removed by proper etching techniques yielding the desired nanostructures. As mentioned above, AAO is the most commonly used negative template for nanostructure growth. The AAO templates are prepared by anodizing Al foils in various acid solutions. AAO is an ideal template for nanostructure growth due to its high thermal, mechanical and chemical stability. Porous AAO templates with controllable nanopore density and various pore sizes can be produced now.

Template assisted electrochemical route is a feasible low temperature method to synthesize the II-VI compound nanostructures. The synthesis is carried out in a three electrode electrochemical bath. The AAO template is configured as the cathode which will be deposited by the products. A metal coating on the AAO surface is essential to make the template conducting as an electrode. The solution with dissolved precursors is used as the electrolyte. The reported II-VI compound nanostructures of nanowires or nanorods synthesized by the template assisted electrochemical route include ZnO,[114] ZnS,[115] CdS,[116] CdSe,[117] CdTe,[118] PbSe[119] and PbTe.[120] For the ternary 1D nanostructure synthesis, vertically aligned ZnCuTe nanowire arrays[121] and ordered single-crystalline $CuInSe_2$ nanowire arrays[122] have been prepared by the liquid phase method with AAO as the hard template. The main drawback of the solution based synthesis method is that the contaminants and impurities adsorbed on the nanostructure surface will

significantly affect and confuse the physical properties of these nanostructures. Meanwhile, the stoichiometry of the ternary products is difficult to be accurately controlled by the liquid phase route due to the complexity of the organic precursors.

Summarized from the above, good uniformity and stoichiometry selectivity are the challenges faced by the vapor phase growth technique and liquid phase growth technique, respectively. Products with varied stoichiometry would obscure the characterization of the samples which ideally should be samples with pure stoichiometry. Therefore, it is necessary to develop an easy and feasible way to synthesize ternary II-VI 1D nanostructure with uniform composition and controllable stoichiometry on a reasonably large substrate.

1.3 Physical Properties and Potential Applications of Ternary II-VI 1D Nanostructures

1.3.1 Electrical Properties and Potential Applications

The electrical properties of nanostructures show deviation from their bulk counterparts. The variation of the electrical properties with dimensionality can be attributed to the difference of electronic density of states. In short, the density of states have the dependence of $\rho \propto E^{\frac{D}{2}-1}$, where D = 1, 2, 3 is the dimensionality and E is the energy.[123] In addition, the band gap of the nanostructures can be blue shifted with reduction in size due to the spatial confinement. The relationship of the band gap and the size of the nanostructures can be briefly expressed as

$\Delta E \propto \frac{1}{d^2}$, where d is the characteristic size of the nanostructure. For nanostructures with different dimensionality, the band gap shift changes differently with size due to the difference in confinement degree.[123, 124] Therefore, the electrical properties of the nanostructures are highly determined by the corresponding size and dimensionality. Moreover, the electronic transport in nanostructures can be appropriately affected by the high electron scattering at the boundaries.[125] Thus the resistivity of the nanostructures will increase as compared to their bulk form due to the large surface scattering. This demonstrates the electronic transport property of the nanostructures sensitively depends on the nanostructure surface and surrounding medium.[126]

The electrical properties of 1D nanostructures are normally tested by two-probe or four-probe measurements *via* fabricating metal electrodes on them with the electrode gaps from nano to micron scale. The individual nanostructures are transferred to a substrate and then the proper metal electrodes are deposited on to the nanostructures using suitable masking or lithography techniques. In some special cases, the position of the nanostructures can be precisely controlled across the electrodes by the aligning strategies.[127, 128]

The variety of crystal structures (electronic band structures) makes the II-VI compound nanostructures with different electrical behavior. The previous investigation suggested that for most of the nanostructured II-VI compound, the electrical properties resemble the bulk counterparts (insulating, semiconducting or metallic). However, the significant quantitative deviations from the properties of

their bulk form are often observed. From the previously reported I-V characteristics of the II-VI compound 1D nanostructures, the CdO nanoneedles[129] were demonstrated to exhibit metallic behavior, whilst the ZnO nanowires[130] and CdS nanowires[131] showed semiconducting characteristics.

The quantitative information of the electrical property including carrier type, carrier mobility and carrier density can be calculated from measuring the corresponding field-effect transistors (FETs) fabricated based on the 1D nanostructures. In a typical FET architecture, an individual nanowire is transferred onto a heavily doped Si substrate coated with dielectric layer (normally, SiO_2 or Si_3N_4). The fabrication is completed by deposition of suitable metal electrodes on the 1D nanostructures using focused ion beam (FIB) or electron beam lithography (EBL) techniques. The metal contacts on either end of 1D nanostructures can work as the source (S) and drain (D) electrode, respectively. The electrode connected to the heavily doped Si substrate can function as the back gate electrode. According to the typical working principle, the output current (I_{ds}) through the 1D nanostructures can be controlled and modified by altering the back gate voltage (V_g).

The FET devices fabrication and performance characterization of many II-VI compound 1D nanostructures have been demonstrated recently. For example, abundant research activities have carried out on ZnO nanowire FETs. Maeng and co-workers fabricated the ZnO nanowire FET and demonstrated its performance was largely determined by the environments.[132] Moreover, recent studies indicated that the surface morphology could largely affect the performance of

single ZnO nanowire FET. Hong and co-workers obtained different performance characterization from the ZnO nanowire FETs with corrugated and smooth surfaces.[133] Besides abundant reports on the ZnO FETs, another II-VI compound semiconductor of CdS nanostructures also attracted many attentions from the researchers. Duan and co-workers demonstrated the high-performance FET fabricated from CdS nanoribbons in 2003.[134] Following the similar idea, Ma and co-workers improved the architecture to form a metal-semiconductor FET on single CdS nanobelts.[135] This FET device was demonstrated with multifunctional performance accompanied with nano-Schottky diodes function. Due to the tuneable electronic band structures, the ternary II-VI 1D nanostructures are expected to show tuneable and controllable electrical properties. In this case, the 1D FET devices will be promoted towards practical applications. Li and co-workers reported the ternary nanoscaled FET fabricated from an individual $CdS_{0.25}Se_{0.75}$ nanoribbon.[136] Their results revealed that the ternary CdS_xSe_{1-x} nanoribbon FET showed better performance and higher carrier mobility than that of binary CdS and CdSe nanoribbons.

1.3.2 Optical Properties and Potential Applications

In the low dimensional materials, the near band edge energy states are densely packed due to the dimensionality confinements. This promotes the probability of optical transition to occur. II-VI compound semiconductor nanostructures, especially those with direct band gaps were demonstrated to process attractive optical properties and can be served as nanoscaled photonic components.[137-139] Abundant research activities have been carried out on nano-

photonics of II-VI compound 1D nanostructures including their lasing properties, waveguide demonstrations etc.[17, 140-142] The tuneable optical properties of ternary II-VI 1D nanostructures attracted great attentions and better performance photonics applications facilitated by the tuneable band gaps have been demonstrated. For example, many researchers have demonstrated the optically pumped stimulated emissions (SE) from 1D ternary alloyed II-VI compound nanostructures.[143] As mentioned above, excitonic emission is desirable for decreasing the threshold of lasing. The exciton binding energy of typical II-VI semiconductors, such as, CdS (~28 meV),[144] ZnS (~40 meV),[145] and ZnO (~60 meV),[146] is larger than the thermal energy at room temperature, which facilitate the excitonic emission at room temperature. As is well known, lasing action requires a proper optical cavity to obtain positive feedback. In the case of 1D nanomaterials, the cavity is usually achieved by either pumping in a single wire/ribbon (Farby-Perot or whispering gallery mode lasing) or realizing random lasing in an ensemble of densely distributed nanowires/nanoribbons. Both of the cases need not only a suitable pumping scheme but a desirably controlled sample fabrication or manipulation. The first observation of lasing from ternary CdS_xSe_{1-x} nanowhiskers was reported by Pan *et al*.[147] An individual nanowhisker was pumped by the nanosecond pulses (Nd: YAG, 355 nm) at room temperature. Besides the demonstration of lasing in CdS_xSe_{1-x} nanostructures, lasing in other ternary II-VI nanomaterials, such as ZnS_xSe_{1-x} nanowires[148] and $Zn_xCd_{1-x}S$[47, 61] nanoribbons, were also observed.

In photonics, a waveguide is an element that is functionalized to confine and route electromagnetic waves into specific directions. 1D nanostructures are expected to function as waveguides due to the cavities, ability to guide and manipulate light on sub-wavelength scale. The high aspect ratio of 1D nanostructures also enables them to accomplish their role as light interconnections.[138] Several inherent properties of ternary II-VI 1D nanostructures are immediately recognized to be alternative for waveguide application. Ternary II-VI semiconductors have wide tuneable band gaps and large dielectric constants, which facilitate higher refractive index than the surroundings to enable transmission of light *via* total internal reflection with high efficiency. Several demonstrations of waveguiding based on ternary II-VI 1D nanostructures have been reported by Pan and Zou groups in the last decade.[147, 149] Active waveguiding where the nanostructures are operated near the band edge was demonstrated in the CdS_xSe_{1-x} nanoribbons.[150] Band edge PL emission, excited within the body of the nanoribbons, was propagated along the ribbon to be emitted at its end while no appreciable emission was observed in other region. The development in nanowire/ribbon waveguides is anticipated to open the possibility for implementation of 1D nanostructures in highly integrated and compact photonic circuits, which have the potential to alleviate the speed limitation and power dissipation in electronics, and will revolutionize communication and computing systems. Therefore, efficient injection, propagation, and manipulation of light on sub-wavelength scale based on 1D

nanostructures is definitely an essential research direction to accomplish the encouraging potential of ternary II-VI 1D nanostructure waveguides.

1.3.3 Optoelectronic Applications

The wide variety of electrical and optical properties shown by the ternary II-VI 1D nanostructures are expected to facilitate more attractive photoelectrical properties. Thus, the ternary 1D nanostructures will function as the building blocks for comprehensive nanoscaled optoelectronic devices. Among these devices, photosensors are critical component in optoelectronic circuits.[151-157] As discussed above, the ternary II-VI nanostructures have the controlled and designed band gaps from UV to NIR, which make the ternary nanostructures promising candidates as photosensors. Park and co-works reported the CdS_xSe_{1-x} nanowire photosensors based on a network-bridge structure.[158] More recently, Javey and co-workers reported the tuneable photodetectors fabricated from different stoichiometry CdS_xSe_{1-x} nanowires by contact printing method.[159]

Electroluminescence (EL) is a physical phenomenon in which light emission is driven by electricity. The process consists of carrier injection and radiative recombination. EL property of semiconductors has attracted great attentions due to the possibility that it could be easily integrated into electronic circuits to provide wide applications on lighting and displays. Current investigations focused on resolving the main challenges of improving the conversion efficiency and device stability. Ternary II-VI compound nanowires and nanoribbons are ideal candidates with EL phenomenon for electronic

applications because of their inherent properties such as tuneable large band gap coverage, controllable direct band gap, large aspect ratio, small size, and high crystalline quality. Continually tuneable large band gap coverage facilitate them to be utilized covering various spectrum range from UV to IR while controllable direct band gap is the essential requirement for desired color light emission. Large aspect ratio can provide the flexibility to manipulate the integration, and the small size of the materials is possible to facilitate a smaller emission beam spot. In addition, the high crystalline quality would enhance the radiative recombination efficiency. Fan and co-workers have demonstrated the architecture of an LED based on the heterostructure of n-CdS_xSe_{1-x} nanowires/p-SiC substrate.[160] The multicolored visible light emission from yellow to red was achieved by varying the chemical composition.

Solar energy is one of the most abundant but least harvested renewable energy sources. Cost-effective solar cells based on 1D nanostructures have attract a great deal of attentions due to the novel device structures and assembly processing for achieving acceptable efficiencies[161]. The ternary II-VI semiconductors with tuneable band gaps covering the entire solar spectrum are ideal material platforms for full spectrum photovoltaic design and solar cell application. However, despite the rapid expansion of the binary II-VI nanostructure solar cells, the real fabrication of solar cell devices based on ternary II-VI 1D nanostructures have not experimentally been realized. Recently, Ning and co-workers theoretically designed a lateral multiple junction solar cell with $Cd_xPb_{1-x}S$ as platform.[162] In their design, each of the lateral junctions could absorb

desired wavelength solar radiation due to the controllable band gap optimization. The simulation results indicated a conversion efficiency of ~40%. The proposed design demonstrated that spatially composition graded ternary $Cd_xPb_{1-x}S$ nanowires presented the potential to deliver efficiencies competitive with other high efficiency solar cells on market today. The potential of fabrication lateral multiple junction solar cells with high performance and low cost based on ternary II-VI nanowries makes them an attractive prospect for decreasing the cost per watt of photovoltaic energy. However, many challenges remain unresolved in research and industry before this proposal becomes practical.

1.4 Objective and Scope of the Present Work

An overall review on the reported literatures shows that the detailed studies on ternary II-VI 1D nanostructures are limited. This is due to the difficulties caused by the complex of the ternary structures in the synthesis, characterization, properties investigation as well as corresponding applications. The existed research gaps on the current studies of ternary II-VI 1D nanostructures can be summarized as following:

- Despite that some growth techniques have been developed and employed to synthesize ternary II-VI 1D nanostructures with single crystalline quality, the growth methods to simultaneously realize good uniformity and stoichiometry selectivity are still absent.
- The absence of samples with highly uniform composition will hamper their structural and physical property characterizations. Therefore, the

deep understanding on the physical properties varying with the composition is still unclear.

- Only few simple electronic and optoelectronic applications have been demonstrated from the ternary II-VI 1D nanostructures. The potential on practical applications of these nanostructures need to be further explored and demonstrated.
- Post synthesis techniques to further adjust and tailor the property of the nanostructures are absent. Therefore, the simple and efficient post-treatment techniques are desired to facilitate local modification of the electrical and optical properties of the nanostructures.

The main aim of this thesis is to develop a facile and effective one-step growth method to synthesize ternary II-VI 1D nanostructure with uniform composition and controllable stoichiometry on a reasonably large substrate. On top of this, the dependence of the physical properties on the chemical composition will be systematically investigated. Furthermore, the corresponding potential applications in electronics and optoelectronics will be studied and demonstrated. The specific aims of this thesis are shown as below:

1) Development and optimization of techniques for the synthesis of ternary II-VI 1D functional nanomaterials. The material systems to be developed include CdS_xSe_{1-x}, ZnS_xSe_{1-x}, and their hybrid complex nanostructures.

2) For item (1) above, the aim is to achieve growth with uniform chemical stoichiometry of the resultant ternary compound covering the entire substrate.
3) For item (1) above, the second aim is to be able to synthesize ternary compound with controllable and tuneable chemical composition.
4) Investigation of the physical properties of the ternary nanomaterials such as CdS_xSe_{1-x} with the aim to investigate how the measurable physical properties vary with the stoichiometry of the compound (i.e. how do the physical properties depend on the variation in value of *x*).
5) Investigation of the focused laser modification of the CdS_xSe_{1-x} and their hybrid system with the aim to tailor and tune the photoelectrical properties of the ternary nanostructures. Detail mechanism of the laser induced modifications of the nanostructures and the nature of the final product will be studied.
6) Explore the potential applications of these nanomaterial systems in multifunctional devices.

The results of our studies should have significant impact on synthesis of ternary 1D nanostructures with uniform and controllable stoichiometry. It will also theoretically promote the understanding of the growth mechanism of these ternary nano-systems. The systematical investigations will facilitate a deeper insight on the fundamentals of optical properties and electrical transport processes in ternary nanomaterials. The detailed investigation and clear understanding on the fundamental properties should promote the process of developing and

optimization of the corresponding nano-scaled device applications based on the ternary II-VI 1D nanostructures.

It is known that the ternary II-VI 1D nanostructure is an emerging research area and thus, the scope of our research is focused on the ternary zinc and cadmium chalcogenide nanostructures. Other typical II-VI 1D nanostructures will not be included in this thesis due to the problematic issues involved in the synthesis and characterization.

1.5 Organization of the Thesis

Following this chapter, the experimental tools and techniques as well as the theoretical approaches will be detailed in Chapter 2. Chapter 3 will describe the growth and structural characterization of the ternary nanostructures of CdS_xSe_{1-x} nanobelts, ZnS_xSe_{1-x} nanowires, and their hybrid complex nanostructures. Chapter 4 will discuss the fundamental optical properties in these ternary 1D nanostructures. The properties are systematically studies by various optical characterization tools in steady and non-equilibrium states. According to the deeper understanding on the fundamental properties obtained from the Chapter 4, the corresponding potential applications will be demonstrated in Chapter 5. In Chapter 6, a home-built focused laser beam system will be employed to locally modify the ternary CdS_xSe_{1-x} nanobelts. Under this modification, the nanobelts can be facilitated with controlled properties and multifunctional applications. Chapter 7 will provide a brief summary on the results described in this thesis and will suggest some further research directions.

Chapter 2

Experimental Facilities and Techniques

In this chapter, techniques adopted for the controlled growth of ternary II-VI 1D nanostructures and various characterization facilities are detailed. After which different characterization facilities employed for the identification of morphology and crystal structure, chemical stoichiometry and composition of the as-grown products are described. Following this, the techniques employed for the characterization of electrical, optical as well as photoelectrical properties of these nanostructures are discussed. A theoretical description on the ultrafast optical spectrum analysis is also provided.

2.1 Growth Technique

The chemical vapor deposition (CVD) is the most popular approach in nanostructure growth due to the virtue of its effectiveness and simplicity in synthesizing diverse structure morphologies from various materials.[163] This technique is typically carried out within a horizontal tube furnace using powder or condensed source as precursors that are vaporized at a high temperature zone, where the resulting chemical vapor is transported and deposited onto the substrate at lower temperature. The following growth parameters can be carefully chosen to form the desired products: (1) the type of source, which would determine the stoichiometry and phase of the product; (2) the elevated temperature of the heating zone, by considering the source material volatility; (3) the substrate temperature, which may affect the type of products; (4) the pressure of the tube

chamber, controlling the vapor pressure and evaporation rate of the source; (5) the carrier gas and flow rate, to allow desired chemical reaction to occur and to tune the growth rate during vapor transportation; (6) the evaporation time, which will strongly determine the size of the products. All of our ternary 1D nanostructures are synthesized using this technique. A typical schematic of the set-up and the optical photo of the furnace in our lab are given in Figure 2.1.

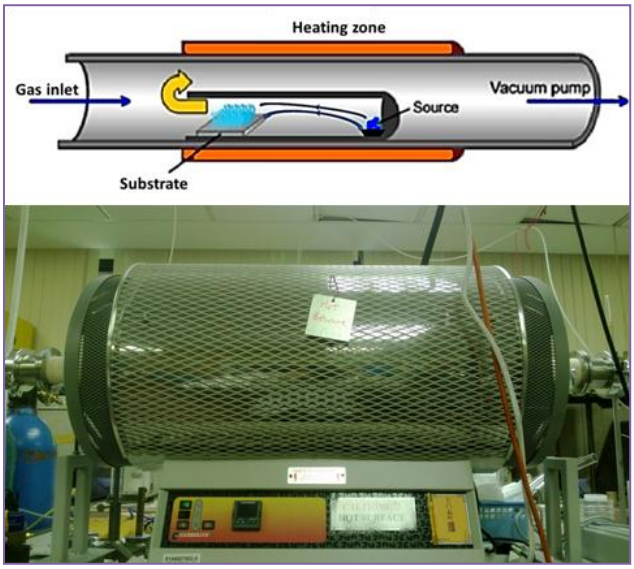

Figure 2.1 Schematic diagram and photo image of horizontal tube furnace in our lab.

2.2 Characterization Tools and Techniques

As-grown products were characterized by various state-of-the-art surface analysis techniques. In the following section, various tools utilized for the characterization of structure morphology, crystal quality, and chemical composition of the nanostructures are briefly outlined.

2.2.1 Scanning Electron Microscopy (SEM)

Nanometer scaled surface features can be imaged by SEM. A finely focused electron beam scans on the sample surface and secondary electrons emitted from the samples were collected for imaging. The morphological characterization of our nanostructures was carried out by field emission scanning electron microscopy (FESEM, JEOL JSM-6700F). The spatial resolution of about 10 nm can be achieved using FESEM. The typical acceleration voltage applied on the electron beam for the imaging was controlled in the range of 2-10 KV and the generated emission current was about 5-20 μA.

2.2.2 Transmission Electron Microscopy (TEM)

Despite of the intrinsic properties of the II-VI semiconductors, the unique properties of the 1D nanostructures are highly dependent on their size, aspect ratio, and defect density. Thus the characterization on crystal quality of individual nanostructure is essential. TEM microscopy is an accepted feasible technique with the unique capability of high magnification range. Employing TEM microscopy, both low magnification images of nanostructures and lattice resolved high resolution images can be captured. The low resolution TEM image can provide information related to the size, morphology and shape of the nanostructure. In addition, the high resolution TEM (HRTEM) images can provide more information about the crystalline quality, growth direction, lattice parameters, details of the defect distribution etc, in conjunction with the selected area electron diffraction (SAED) patterns.

The TEM inspection of our synthesized nanostructures was carried out utilizing JEOL, JEM 2010F microscopy with 200 KV electron beam or Philips CM300 microscopy with 300 KV electron beam. For TEM analysis, a suspension solution was firstly prepared by separating as-grown nanostructures from substrate by sonication in high purity (>99.9%) ethanol. Subsequently, some of the nanostructures were transferred onto commercially available copper TEM grids covered with holey carbon film by dip-coating of the suspension solution. These grids were then dried in air and loaded into microscopy for studies.

2.2.3 X-Ray Diffraction (XRD)

XRD is a well-known technique to investigate crystal structure, grain size, and internal strains of crystalline materials. The XRD patterns provide information which can be extracted to identify the crystal structure of the as-grown nanostructures. Our nanostructures were investigated using Philips X'PERT MPD (Cu-Kα (1.5406 Å) radiation) machine. The crystal structure analysis was based on the Bragg diffraction formula:

$$2d\sin\theta = n\lambda \tag{2.1}$$

where λ is the wavelength of X-ray, n is an integer which is also called diffraction series number. The Bragg's law is schematically described in Figure 2.2. When an X-ray beam incidents by a sweep angle θ into a crystalline material with the lattice plane space of d, the enhanced diffraction patterns will be obtained due to the overlying of the reflection wave under the condition of compliance with Eq. (2.1). One of the demerits of utilizing XRD to characterize the as-synthesized

nanostructures is the signal from the underlying substrate. Since the X-ray shows large penetration length, the XRD patterns comprises peaks arising from the nanostructures as well as the supporting substrate.

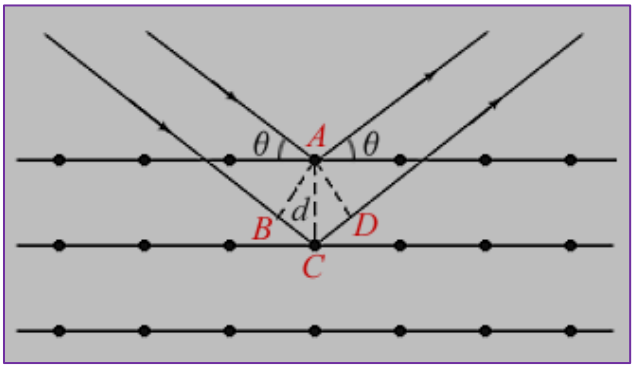

Figure 2.2 Schematic diagram of Bragg diffraction.

2.2.4 X-Ray Photoelectron Spectroscopy (XPS)

XPS spectroscopy is a widely used surface analyzing tool with high precision. In XPS analysis, the binding energy of core level electrons can be estimated by measuring the kinetic energy of the electrons emitted by the absorption of X-ray photons. XPS is useful for elemental identification due to the more atomic like behavior of the core level electrons. In addition, the XPS technique is sensitive to the chemical environment of an atom inside a material, which enables the identification of the valence state of a particular element. Since some elements such as the transition metals have the capability of forming stable compounds with different valence states, it is important to identify the exact chemical composition. The XPS technique is particularly beneficial for the chemical composition analysis of the as-grown nanostructures among the surface

analyzing tools. Our XPS spectrum was recorded under ultrahigh vacuum (UHV) condition using ESCA MK II; Mg Kα source (1253.6 eV) system.

2.3 Optical Spectrum Techniques

2.3.1 Raman Spectroscopy

Raman spectroscopy is a non-destructive tool for the characterization of optical and electronic properties of semiconductors. Raman spectroscopy is principally based on the inelastic scattering of electromagnetic waves caused by the photon-phonon interaction within the materials. In a typical set-up, a laser beam is incident onto the sample and the scattered photons will be collected to measure the wavelength shift caused by the inelastic light scattering. Particularly, Raman spectroscopy is a powerful technique for the characterization of semiconductor nanostructures. By utilizing micro-Raman spectroscopy, the probe size of the samples can be reduced to individual nanowire level. Our Raman spectrum probed from the nanostructures were carried out using the Renishaw inVia system 2000 mico-Raman machine in backscattering geometry. Polarized laser light (532 nm or 785 nm in wavelength) was focused onto the nanostructures using a 100× objective lens on an optical microscope equipped with the Raman machine. The laser spot size on the sample can be focused to ~1μm. Figure 2.3 schematically illustrates the set-up architecture of the Raman spectroscopy.

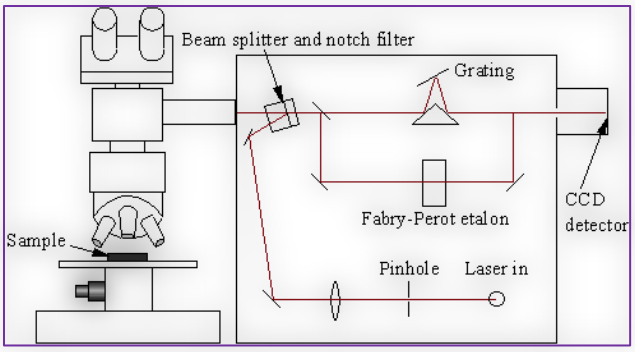

Figure 2.3 Schematic diagram of micro-Raman spectroscopy.

2.3.2 Photoluminescence (PL) Spectroscopy

PL spectroscopy is a noncontact, nondestructive technique to probe the electronic structure of semiconductors. Laser light is incident onto the sample, where the light is absorbed and imparts the excess energy to the samples with the process of photo-excitation. The photo-excitation facilitates electrons within the semiconductor to move onto permissible excited states. After these electrons return to equilibrium states, the excess energy will be released, which may result in the emission of light (radiative process) or a nonradiative process. The energy of the emitted light is related to the difference in energy levels between the excited state and the equilibrium state. In particular, PL spectroscopy is a powerful tool for the characterization of nanomaterials due to the energy band broadening in nano-scale. The simple schematic of a PL spectroscopy set-up is shown in Figure 2.4. The sample can be held in a cryostat which can facilitate the measurements taken at low temperature (~5 K).

On top of the standard PL spectroscopy, time resolved PL (TRPL) spectroscopy is a powerful technique that can monitor the variation in PL intensity with response to a laser pulse to be measured over time. A monochromator is employed to replace the spectrometer in standard PL spectroscopy set-up to select light of a single wavelength. The selected light will be directed into a photomultiplier detector with the capability of single photon counting. The TRPL facilitates the output to plot light intensity decay curve for photon with a particular wavelength, which can provide information of processes taking place within the nanostructures.

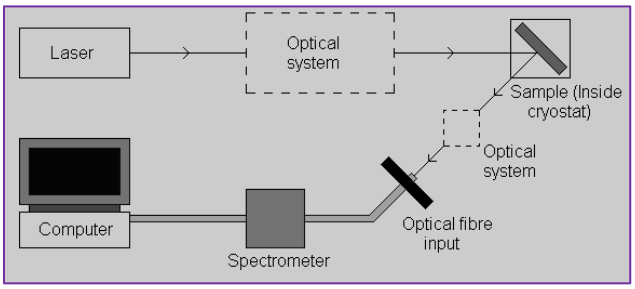

Figure 2.4 Schematic diagram of PL spectroscopy.

2.3.3 Terahertz Time-Domain Spectroscopy (THz-TDS)

THz-TDS is a nondestructive and contactless spectroscopic tool in which the physical properties of a material are probed by short pulses of broadband THz wave. This technique was developed at AT&T Bell Labs[164] and IBM T. J. Watson Research Center[165] in the 1980s. This technique can provide more information than traditional infrared spectroscopy since it is a coherent technique that can carried out both high sensitive amplitude and time resolved phase measurements, which reveal a wealth of information of materials that interact with THz radiation. In addition, the typical charge carrier scattering time is in picosecond (10^{-12} s)

range, which matches with THz frequency range in the electromagnetic spectrum. This facilitates the radiation in the THz frequency range interacts in a specific manner with charge carriers, making THz radiation the ideal probe for charge carrier in materials. The schematic illustration of a typical THz-TDS system is displayed in Figure 2.5. Our nanostructures were investigated in a THz-TDS system with a frequency bandwidth between 0.3 and 6 THz, and acquisition time under one minute, a spectral resolution of 50 GHz, and a dynamic range of 1×10^5 in electric field.

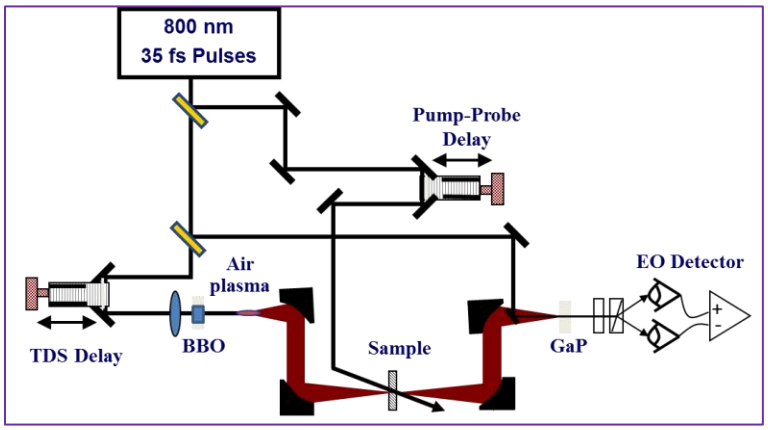

Figure 2.5 Schematic diagram of THz-TDS.

In the theoretical analysis, the experimental results will be described by the dielectric models. Generally, in the THz regime, the dielectric function $\varepsilon_m(\omega)$ consists of the contributions from high-frequency dielectric constant, conduction free electrons, and lattice vibrations, which is described by[166]

$$\varepsilon_m(\omega) = \varepsilon_\infty - \frac{\omega_p^2}{\omega^2 + i\gamma\omega} + \sum_j \frac{\varepsilon_{st_j}\omega_{TO_j}{}^2}{\omega_{TO_j}{}^2 - \omega^2 - i\Gamma_j\omega} \qquad (2.2)$$

where ε_∞ is the high-frequency dielectric constant, the second term describes the contribution from free electrons or plasmons and the last term presents the behavior of optical phonons, in which the summation involves all lattice oscillations with the *j*th transverse optical phonon frequency ω_{TO_j}, phonon damping constant Γ_j, and oscillator strength ε_{st_j}. The key parameters describing the dynamics of free electrons or plasmons are plasma frequency $\omega_p = \sqrt{Ne^2/(\varepsilon_0 m^*)}$ and carrier damping constant γ, where m^* is the electron effective mass, N is the carrier density, and ε_o is the free space permittivity constant. The free carrier mobility can be calculated through the relation

$$\mu = \frac{e}{m^* \gamma} \tag{2.3}$$

The two most frequently used models can be derived from Eq. 2.2. When the response arises mainly from the contributions of free electrons or plasmons, the classical Drude model is usually adopted

$$\varepsilon_m(\omega) = \varepsilon_{mr} + i\varepsilon_{mi} = \varepsilon_\infty - \frac{\omega_p^2}{\omega^2 + i\gamma\omega} \tag{2.4}$$

On the other hand, if the interaction between the radiation field and the fundamental lattice vibration plays the dominant role and enables absorption of electromagnetic wave due to the annihilation or creation of phonons, the dielectric function mainly consist of the contribution from lattice vibration, which will be described by the typical pseudo-harmonic phonon model

$$\varepsilon_m(\omega) = \varepsilon_{mr} + i\varepsilon_{mi} = \varepsilon_\infty + \sum_j \frac{\varepsilon_{st_j}\omega_{TO_j}{}^2}{\omega_{TO_j}{}^2 - \omega^2 - i\Gamma_j\omega} \qquad (2.5)$$

where the oscillator strength ε_{st_j} is related to the static dielectric constant or high frequency dielectric constant, ε_∞ and the background dielectric constant or low frequency dielectric constant, $\varepsilon(0)$ by the relation, $\varepsilon_{st_j} = \varepsilon(0) - \varepsilon_\infty$.

2.3.4 Optical Pump-Terahertz Probe (OPTP) Spectroscopy

OPTP spectroscopy which is also called time-resolved THz-TDS (TRTS), is an emerging technique with the integration of optical pump pulse which is synchronized with the THz probe beam upon typical THz-TDS set-up. Thus this technique can be employed directly to investigate the photocarrier dynamics and transient photoconductivity induced by ultrafast laser excitation. Figure 2.6a schematically illustrates the optical set-up of OPTP spectroscopy. On top of the typical pump-probe technique, OPTP spectroscopy extends the probe range to far-infrared (FIR) region. In OPTP, the pump pulse is normally an intense visible pulse and the probe pulse is a mild THz pulse. By collecting the change in the THz transmission as a function of time after photoexcitation of the sample, we can monitor the variation in optical constants (refractive index and absorption coefficient) of the sample. The effect of the photoexcitation on the THz wave transmission is schematically shown in Figure 2.6b. The changes of the optical constants are directly related to the sample's conductivity. In particular, OPTP spectroscopy is a powerful technique in characterization of optoelectronic properties in nanostructures. It is a contactless and nondestructive electrical probe

with capability of measuring the photoconductivity on sub-picosecond to nanosecond timescale. Using this technique, not only the time dependent conductivity can be measured, but also the complete frequency dependent conductivity will be recorded without attaching any probe electrode wires to the nanostructures. The OPTP spectroscopy does not require the employment of Kramer-Kronig analysis which is a mathematical approach involving the calculation of the real and imaginary parts of a function.[167]

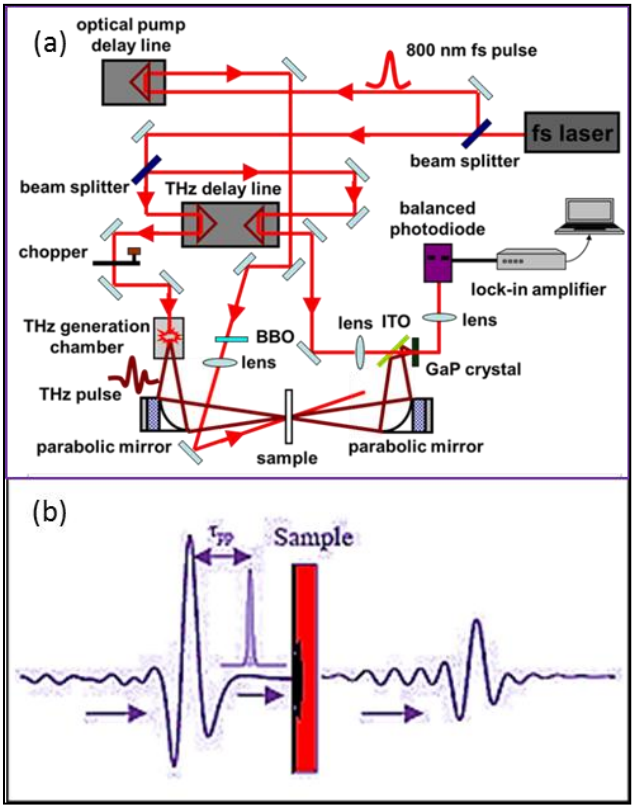

Figure 2.6 (a) Schematic diagram of OPTP set-up. (b) Schematic illustration of the photoexcitation effect on the transmission of THz pulse.

2.4 Device fabrication processes and characterization tools

In parallel to the development of nanoscaled device application, we have devoted efforts on enlarging the device system scale and creating a new paradigm referred to as large-area devices where integrated nanostructures are fabricated over substrates. We developed and employed a direct contact transfer approach to fabricate the integrated nanostructure device covering reasonable large area. The contact transferring process is schematically illustrated in Figure 2.7. Briefly, the Si substrate (donor substrate) covered with randomly grown 1D nanostructures was positioned face-down against a plain Si_3N_4 (200 nm)/Si substrate (acceptor substrate). The donor substrate was gradually slid several mm to a desired direction with downward pressure. During this process, 1D nanostructures would be transferred to the acceptor substrate parallel aligned along the sliding force direction forming laterally aligned nanowire/belt networks. The contact transfer technique utilizes shear force to realize the alignment of the 1D nanostructures, where the attraction of van der Waal's force and other chemical binding interaction between the nanostructures and the substrate enable the nanowire/belts to anchor onto the acceptor substrate. The density of the nanowire/belt network is determined by the as-synthesized nanowire/belt density and would be increased by repeated transfer. In addition, the covering area of the nanonet can be accurately controlled by the donor substrate size. On top of the direct contact transfer, patterned photoresist can be employed to define the active area on the substrate as shown in Figure 2.7b.

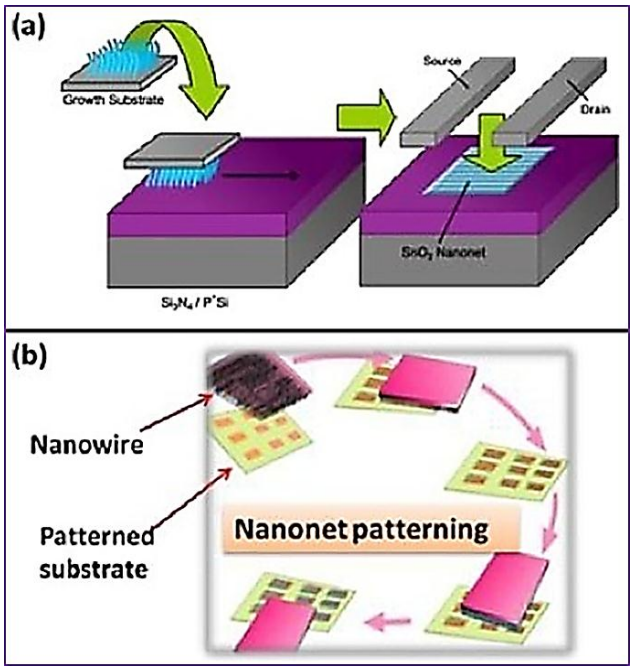

Figure 2.7 (a) Schematic of the direct contact transfer process to fabricate aligned nanowire/belt networks. (b) Illustration of the process of fabrication of networks on patterned substrate.

To realize flexible management and better operation of the contact transfer process, a simple but efficient set-up was designed as shown in Figure 2.8. A three-axis movable stage was employed which enables the pressure control in x-axis while speed and alignment control facilitated in z-direction.

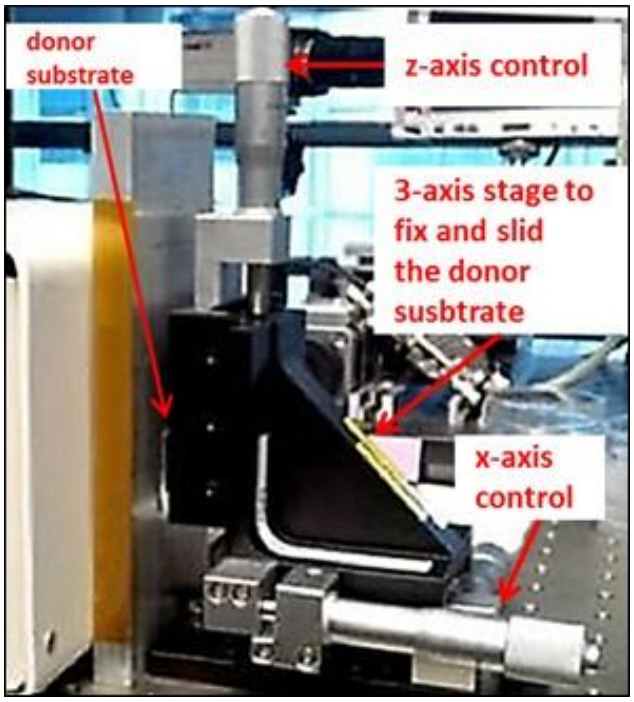

Figure 2.8 Optical photo picture of the home-built contact transfer set-up.

The device fabrication was done by thermal deposition of 200 nm thick metal electrodes on top of the networks assisted by the micro shadow mask with channel length varying from 70 to 200 μm. After the device fabrication, the performance characterization was carried out by the TTP-6 probe station technique combined with a Keithley 4200 source meter under bot ambient and vacuum (10^{-6} Torr) condition.

2.5 Laser pruning technique

Laser pruning is a facial and efficient approach for direct decoration or creation of micropatterns on nanomaterials. Our group developed this technology through an optical microscope-focused laser beam set-up since 2003.[168] And this technology has been employed on decorating 1D nanomaterials, such as CNT,

semiconductor nanowries and nanoribbons, and 2D nanomaterials of graphene oxide.[169-173] The set-up diagram of the laser pruning technique is schematically illustrated in Figure 2.9. A diode laser with continuously tunable power and at a wavelength of 660 nm is adopted. The parallel laser beam is directed into in to a modified upright optical microscope *via* two reflecting mirrors (M). Inside the microscope, the laser beam is directed to an objective lens by a beam splitter (S). The beam will be focused to the sample by a 50× objective lens (L) with a long working distance of 8.7 mm and a numerical aperture of 0.55. The laser beam can be focused to a small size about 1 to 3 μm. By moving the sample stage with respect to the laser beam, micro-patterns can be constructed on the nanostructures. A digital CCD camera is employed to capture optical images and monitor the operation process.

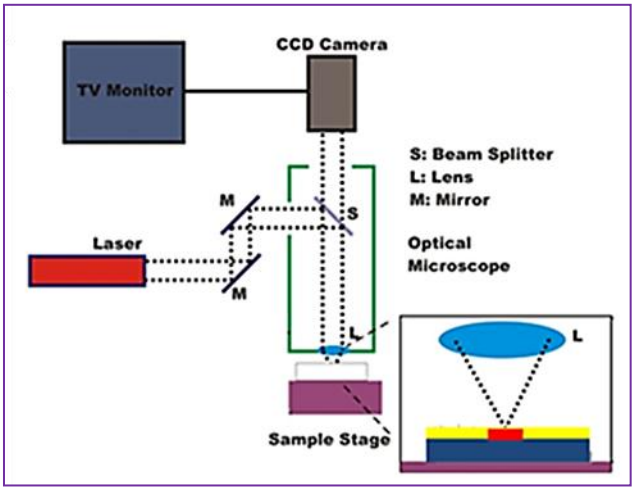

Figure 2.9 Schematic illustration of the focused laser beam set-up.

Chapter 3

Growth of Ternary II-VI 1D Nanostructures and Their Hybrids

3.1 Introduction

The synthesis of ternary 1D nanostructures from II-VI compound semiconductors is a strategic development for both the investigation of intrinsic properties and practical applications of the materials. Therefore, it is an important prerequisite to develop reliable approaches to prepare ternary nanostructures with precisely and flexibly controlled morphology, stoichiometry, and phase. In this regard, various synthesis techniques have been thoroughly explored. Using these techniques, one can prepare 1D ternary nanostructures with high throughput at good reproducibility and reasonable cost. So far, ternary 1D metal chalcogenide semiconductors (AB_xC_{1-x}) of CdS_xSe_{1-x}, ZnS_xSe_{1-x}, $Cu_{2-x}S_ySe_{1-y}$, $Ag_2Se_{1-x}Te_x$, $Bi_2Te_{3-y}Se_y$ nanowires/nanoribbons, and semiconductors ($A_xB_{1-x}C$) of $Zn_xCd_{1-x}S/Se$, $Mn_xCd_{1-x}S/Se$, and $Zn_{1-x}Mn_xS/Se$ nanowires/nanoribbons have been generated *via* chemical vapor deposition, template-assisted electrodeposition, or solution based hydrothermal methods.[46, 47, 49, 68, 87, 105, 174-176] Synthesis of 1D nanostructures is facilitated by promoting nucleation, crystallization, and growth in one direction while suppressing the other two dimensional growth. The methods that have been demonstrated for the synthesis of 1D nanostructures can be briefly categorized into either a vapor or solution base technique according to the precursors and reaction media that are used in the synthesis process.[9] The great benefits of solution based techniques lies in the relatively lower reaction

temperature and high throughput, which is favorable from the economic stance. In comparison, the vapor based techniques are able to generate materials with superior quality due to the high temperature involved during the growth process, which facilitates the materials growth with a long range crystalline order.[177, 178] In the following, we will describe the synthesis of 1D ternary nanostructure systems and discuss briefly their growth mechanism. We mainly focused the synthesis on 1D CdS_xSe_{1-x} nanobelts, ZnS_xSe_{1-x} nanowires and their hybrids structures. The growth techniques employed were typical one-step, two-step or specially designed CVD approaches. The growth mechanism was investigated as vapor-liquid-solid (VLS) process.

VLS growth is probably the most well-accepted and extensively employed technique to synthesize 1D nanowires/nanoribbons. This growth mechanism has been demonstrated by an *in situ* TEM study where the nanowire growth stages were observed.[32] The kinetic processes of this growth method were also extensively examined.[179-182] Figure 3.1 illustrates the VLS growth which is precipitated by the formation of metallic particle droplet which takes the role resembling the function of a catalyst to direct the 1D growth. Noble metal thin films, especially Au, are usually used as the catalyst materials. Due to the effect of thermal annealing, the metallic thin film breaks into particle droplets. Following which the droplet forms a liquid alloy with the vapor species of the desired materials when the substrate temperature is ramped beyond their eutectic temperature. Then the alloy can continuously adsorb the vapor species due to the high sticking coefficient of the liquid surface. When the adsorption is

supersaturated, nucleation occurs and the 1D axial growth is facilitated at the liquid alloy and solid interface. Meanwhile, the secondary nucleation is suppressed due to the higher energy required than that of the crystal step growth and the growth only occurs at a single liquid/solid interface.[32] Several processing parameters such as pressure, evaporation and deposition temperature, flow rate of carrier gas, and duration time should be optimized for different materials. Recently, ternary CdS_xSe_{1-x} nanowires have been produced through a pulsed laser deposition (PLD) process[183] and alloy CdS_xSe_{1-x} nanoribbons have been synthesized in a tube furnace.[46, 62] During the growth in tube furnace, the mixed CdS and CdSe source powders are placed in the middle of the heat zone and the substrate (1-3 cm in size) is positioned at a distance away from the source. Products covering the entire composition range (x varied from 1 to 0) are typically obtained on a single substrate. However, uniformity and selectivity of stoichiometry have not been obtained through this approach. Products with varied stoichiometry would obscure the characterization of the samples which ideally should be samples with pure stoichiometry. Otherwise one cannot draw strong conclusion about the physical properties of the alloy. The challenges in achieving uniform composition on the substrate are due to the fact that the composition of the nanostructured CdS_xSe_{1-x} is highly dependent on the local substrate temperature.[46, 62] The composition value x would change accordingly with the distance of the substrate from the source, changing from 1 to 0 within a 1.2 cm long substrate.[184] This limits the application of these 1D ternary semiconductor nanostructures in areas where uniform composition and tailored physical

properties are required. Therefore, it is necessary to develop an easy and feasible way to synthesize 1D ternary nanostructure with uniform composition on a reasonably large substrate. Recently Li *et al.* employed a complex two-step sulfurization method through thermal annealing of CdSe nanoribbons in a H_2S-Ar atmosphere[136] to fabricate uniform products. However, it is worthwhile to continue to develop simple and facile method to synthesize these alloy nanostructures.

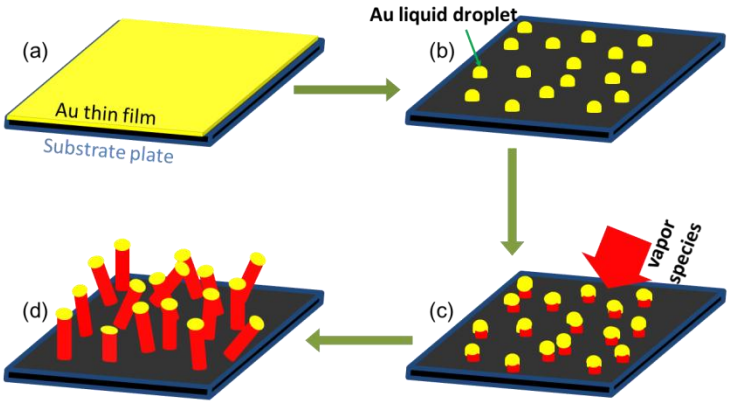

Figure 3.1 Schematic diagram of VLS growth process.

In this chapter, we present a simple and effective one-step approach for the growth of desirable CdS_xSe_{1-x} single crystalline nanobelts with good uniformity and stoichiometry selectivity on single substrates. Uniform composition over the entire substrate was confirmed by energy dispersive x-ray spectrum (EDS) spectra and elemental mapping at different random points from the substrate. With good stoichiometry control and couple with detail knowledge of composition value in CdS_xSe_{1-x} we can arrive at conclusive and decisive description of the physical properties of these ternary compounds. Notably one could provide further insight

into the correlation between the physical properties of the alloy compound and its stoichiometry. The similar approach is also employed for synthesis of high quality ZnS_xSe_{1-x} nanowires with highly uniform stoichiometry. In addition of the synthesis of typical 1D ternary nanostructures, the hybrid complex nanostructure with ZnO/CdS_xSe_{1-x} core/shell architecture is achieved by a two-step CVD method. Furthermore, more complex architecture with composition gradient CdS_xSe_{1-x} on single nanowires is obtained *via* the growth in a specially designed movable source in a horizontal tube furnace. The following sub-sections will describe the experimental method, growth of CdS_xSe_{1-x} nanobelts, ZnS_xSe_{1-x} nanowires, and their complex hybrid nanostructures in detail. The growth mechanism and corresponding structural quality of these nanostructures are discussed as well.

3.2 Experimental Method

CdS_xSe_{1-x} nanobelts with highly uniform composition were synthesized through a VLS approach with CdS (99.995%, Sigma Aldrich) and CdSe (99.99%, Sigma Aldrich) mixed powder as the precursor. The growth was carried out in a single-heating-zone horizontal tube furnace as shown in Figure 3.2a with He (99.9%) as the carrier gas. A ceramic boat loaded with 0.1g mixed powder was inserted into the end of a half-sealed quartz tube with diameter about 1.5 cm. A sapphire wafer sputter-coated with a thin (~1nm) Au layer was loaded inside the quartz tube 15—20 cm away from the source powder. In order to obtain large area samples with highly uniform composition, a specially designed substrate holder (Figure 3.2c) was used. With this holder, substrate could be slotted vertically with

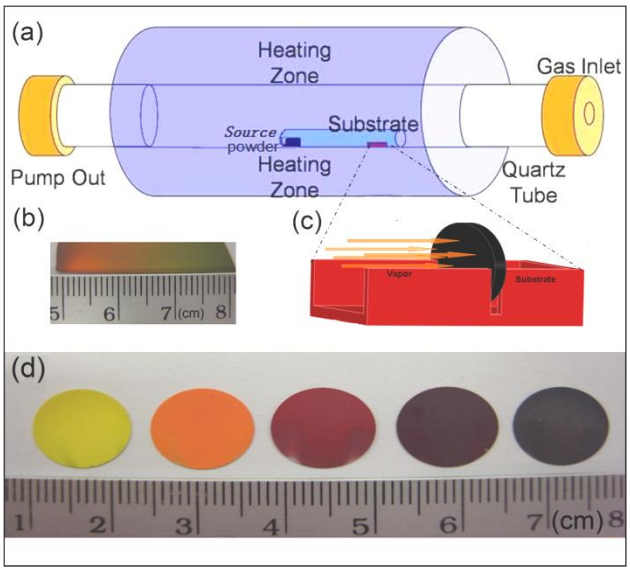

Figure 3.2 (a) Schematic diagram of alloyed nanobelts growth reactor set-up. (b) Nanobelts grown on horizontally placed substrate showing different colors from left to right, indicating wide composition range in the alloyed compounds. (c) Design model of substrate holder. (d) Optical images of five samples with different composition grown on the substrates. Sulphur concentration decreasing from left to right.

the plane of the substrate facing the incoming flux of CdS_xSe_{1-x} vapor during the growth. The vertically positioned substrate was maintained at a fixed temperature during the growth. In this case, all of the nanobelts were grown at the same growth temperature and samples with highly uniform composition covering a large area were obtained. The quartz tube was then placed inside the ceramic tube with the precursor end located at the high-temperature zone of the furnace. The system was first pumped down to a base pressure of 8.0×10^{-3} Torr before the He gas was introduced into the ceramic tube at a constant flow rate of 20 sccm with the pressure regulated and maintained at 1 Torr. After an hour of He flow to purge

away the oxygen, the furnace temperature was ramped to 850 ºC at a rate of 60 ºC/min, and the system was maintained at this temperature for 30 minutes before cooling down to room temperature naturally. Samples with different composition were obtained by changing the molar ratio of CdS and CdSe powder. The pure binary CdS and CdSe nanobelts were synthesized under the same growth conditions except only the CdS or CdSe powder was used as the precursor.

ZnS_xSe_{1-x} nanowires with uniform stoichiometry composition were synthesized by the similar conversion-evaporation and condensation approach as described in the CdS_xSe_{1-x} nanobelts synthesis. Briefly, the ZnS and ZnSe mixed powders were used as the precursor. The tube chamber was first pumped down to a base pressure of 3×10^{-3} Torr and then the He gas was flowed into the tube at a slow rate of 20 sccm. After 40 minutes flow to purge away oxygen, the temperature of the system was ramped to 1050 ºC at a rate of 35 ºC/min, and during the growth period, the pressure was regulated and maintained at 400 mbar for 90 minutes. After that, the furnace was cooled down to room temperature naturally. Similarly, the chemical stoichiometry was obtained by changing the molar ratio of the starting ZnS and ZnSe powder.

Vertically aligned ZnO/CdS_xSe_{1-x} nanowire arrays were synthesized *via* a two-step CVD method in the tube furnace. Firstly, vertically aligned single-crystalline ZnO nanowire arrays were synthesized by a vapor-solid (VS) process. A 0.3 g powder mixture of ZnO and graphite in a molar ratio of 1:1 was placed in the bottom of a one-end-closed quartz tube. A piece of silicon wafer predeposited with a 200 nm ZnO seed layer by PLD served as substrate and was inserted nearer

to the open end. The quartz tube was placed into a large alumina work tube. The system was initially evacuated to a base pressure of 2.0×10^{-2} mbar before Ar gas mixed with 0.1% O_2 by volume of a total flow rate of 80 sccm was introduced. The pressure in the alumina work tube was raised to 2 mbar. The furnace was heated to 900 °C and held at that temperature for 50 min. The growth temperature at the Si substrate was approximately 800 °C. In the second step, the process as described in CdS_xSe_{1-x} nanobelts synthesis was employed to deposit the CdS_xSe_{1-x} outer-shells. A piece of pre-prepared ZnO nanowire arrays was vertically inserted as the substrate. After the operations as described in CdS_xSe_{1-x} nanobelts synthesis, the hybrid structures with highly uniform and accurately controlled CdS_xSe_{1-x} outer-shells were obtained.

Single nanowires with gradient CdS_xSe_{1-x} composition were obtained by employing a specially designed movable precursor source in a tube furnace which is an improved VLS growth technique. The detailed description about the synthesis operation will be separately discussed in the following sub-sections. By employing this technique, the composition of CdS_xSe_{1-x} could be gradually altered along the length of the nanowires.

3.3 Results and Discussions

3.3.1 Growth of CdS_xSe_{1-x} Nanobelts

In this work, we adopted a modified approach to make use of a tube furnace with mixed CdS and CdSe source powders to synthesize CdS_xSe_{1-x} alloy. A schematic of the setup is shown in Figure 3.2a. Details of the growth conditions

are given in Section 3.2. Figure 3.2b shows an optical picture of the as-grown sample when the substrate was placed horizontally. Evidently, the substrate exhibited a range of colors. This indicated that the sample was covered with nanobelts with different stoichiometries. Thus to avoid nanobelts with wide ranging composition, the substrate was vertically inserted into the slits of a newly designed sample holder (Figure 3.2c). In doing so, we were able to grow CdS_xSe_{1-x} alloy with uniform chemical stoichiometry. Optical pictures of five representative samples with different S and Se concentration were shown in Figure 3.2d. Visibly, these samples showed single and unique colors with good uniformity across the substrate. The yellow sample on the left corresponds to the pure CdS nanobelts with wide band gap (2.44 eV). The black sample on the right corresponds to the pure CdSe sample with a narrower band gap (1.73 eV). The 3 samples in the middle correspond to samples with different proportion of S and Se in the nanobelts.

Panels a-e of Figure 3.3 show the SEM images of these as-grown samples. Evidently from the SEM images, all of them are quasi-one dimensional nanobelts with similar morphologies. The nanobelts have an average length of about several tens of micrometers, 10-30 nm in thickness and ~100-200 nm in width. The corresponding *in situ* energy dispersive x-ray spectra (EDS) are shown in curves f-j of Figure 3.3, respectively. The results indicate the samples comprised of Cd, S and Se elements, and the atomic ratio of S/Cd, namely, the x value gradually reducing from 1 to 0 corresponding to samples a-e. The values are in good agreement with those calculated using Vegard's law from the XRD patterns

(details will be discussed later). It should be noted that more EDS spectra were taken from randomly selected nanobelts to confirm that the whole large area sample has uniform chemical composition.

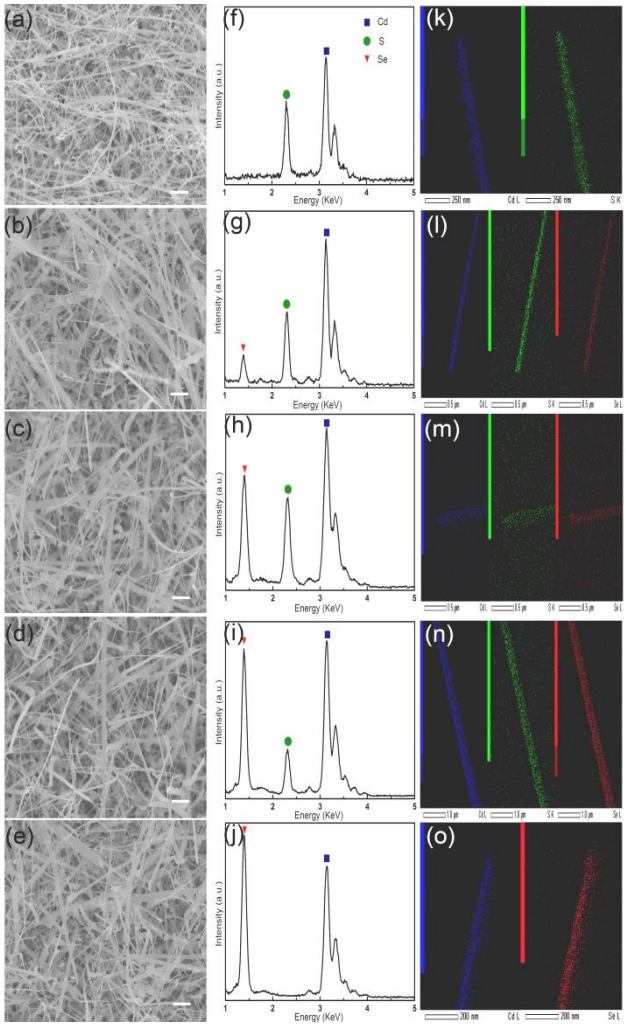

Figure 3.3 (a)-(e) SEM images of five CdS_xSe_{1-x} samples with different compositions. The scale bar is 2 μm. (f)-(j) Respective EDS of these as-synthesized CdS_xSe_{1-x} nanobelts. x value decreasing from 1 to 0 (1, 0.87, 0.65, 0.29, and 0) from (f) to (j). (k)-(o) Elemental mappings of these samples. Cd, S and Se elements distributions are homogeneous.

Moreover, the elements of S and Se were distributed homogeneously in the individual nanobelts, which was supported by the EDS elemental mapping (Panels k-o of Figure 3.3).

The detailed microstructures of these 1D samples were further studied by TEM. The typical TEM images, high resolution TEM (HRTEM) and corresponding selected area electron diffraction (SAED) pattern of two representative samples with the *x* values of 0.8 and 0.2 are shown in Figure 3.4. Figures 3.4a and b display the low magnification TEM images of $CdS_{0.8}Se_{0.2}$ and $CdS_{0.2}Se_{0.8}$ nanobelts, respectively. The corresponding HRTEM images are shown in Figures 3.4c and d. Evidently, the as-synthesized nanobelts are high quality single crystalline with hexagonal structure. For $CdS_{0.8}Se_{0.2}$, the fringe spacings between adjacent lattice planes were measured to be 0.355 nm and 0.674 nm corresponding to the (010) and (001) interplanar distance, respectively. The corresponding values are 0.361 nm and 0.688 nm for $CdS_{0.2}Se_{0.8}$. Their SAED patterns are shown in the inserts of Figures 3.4a and b, which further confirm the nanobelts are typical wurtzite hexagonal structure with lattice parameters of a=0.41 nm, c=0.67 nm for $CdS_{0.8}Se_{0.2}$ and a=0.42 nm, c=0.68 nm for $CdS_{0.2}Se_{0.8}$, respectively.

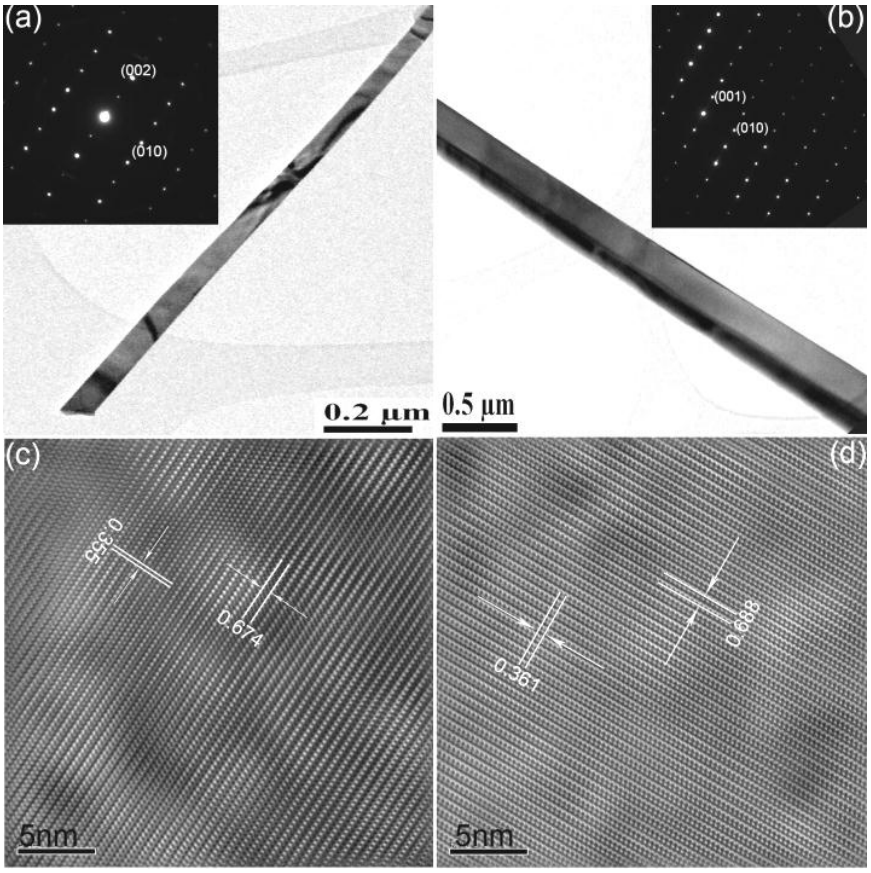

Figure 3.4 TEM images of CdS_xSe_{1-x} with x values about (a) 0.8 and (b) 0.2. Inserts are their corresponding SAED patterns. HRTEM images of CdS_xSe_{1-x} nanobelts with x values of (c) 0.8 and (d) 0.2.

The XRD patterns of five CdS_xSe_{1-x} ($0 \le x \le 1$) samples are shown in Figure 3.5. All diffraction peaks can be indexed to hexagonal wurtzite structure. Referring to Joint Committee on Powder Diffraction Standards (JCPDS) card No. 77-2306 and 77-2307, spectra in Figure 3.5a and 3.5e are pure CdS and CdSe phase, respectively. Their respective lattice constants can be calculated to be $a = 0.41\,\text{nm},\ c = 0.67\,\text{nm}$ for CdS and $a = 0.43\,\text{nm},\ c = 0.70\,\text{nm}$ for CdSe. The peak positions of CdS_xSe_{1-x} alloy are located in the region between CdS and CdSe. From spectra b to d, the diffraction peaks shift gradually towards smaller 2θ

angles, indicating the lattice constants increase with decreasing S concentration (i.e. decreasing *x* value). Since the lattice constants depend on the composition, the composition *x* of these CdS_xSe_{1-x} nanobelts can be determined by using the c-axis lattice constants calculated from the XRD data and employ Vegard's law: $C_x = C_{CdS}x + C_{CdSe}(1-x)$, where C_x, C_{CdS} and C_{CdSe} are lattice constants along the c-axis of CdS_xSe_{1-x}, CdS and CdSe crystals, respectively. For spectra b, c and d, the calculated *x* values are 0.87, 0.65 and 0.29. The results indicate that we can successfully synthesize alloyed samples with modulated and uniform composition covering the full range from CdS to CdSe.

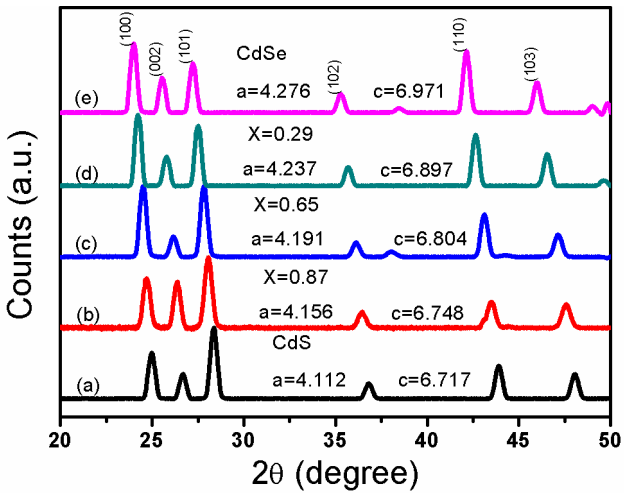

Figure 3.5 Normalized XRD patterns of CdS_xSe_{1-x} nanobelts ($0 \leq x \leq 1$). Spectra (a) and (e) for CdS and CdSe respectively. Spectra (b)-(d) for CdS_xSe_{1-x} samples with different *x* values.

3.3.2 Growth of ZnS_xSe_{1-x} Nanowires

The typical FE-SEM images of two representative ZnS_xSe_{1-x} nanowires with different composition stoichiometry are shown in Figure 3.6a ($x = 0.38$) and

b ($x = 0.18$). Evidently, all of these nanowires have similar morphologies with ultra-long length even up to about hundreds of micrometers and ~100-200 nm in diameter. The elemental compositions were investigated by *in situ* EDS, which are shown in Figure 3.6c and d, respectively. The results indicate that the as-synthesized products consist of only Zn, S and Se elements. The estimated x values from these spectra are $x = 0.38$ and $x = 0.18$, respectively. Further investigation on detailed microstructures of these nanowires was carried out by TEM. The corresponding HRTEM and SAED pattern are shown in Figure 3.6e, f and their inserts. Evidently, the nanowires are high quality single crystalline with typical hexagonal structure. Apparently, the growth direction of $ZnS_{0.38}Se_{0.62}$ nanowires in Figure 3.6e is [001]. The interplanar spacings between adjacent lattice planes were measured to be 0.648 nm and 0.342 nm corresponding to the (001) and (100) planes, respectively. The corresponding values are 0.638 nm and 0.336 nm for $ZnS_{0.18}Se_{0.82}$ nanowire. The SAED patterns shown in the inserts further confirm the typical wurtzite hexagonal structure of these nanowires with lattice parameters of $a = 0.394$ nm, $c = 0.648$ nm for $ZnS_{0.38}Se_{0.62}$ and $a = 0.388$ nm, $c = 0.638$ nm for $ZnS_{0.18}Se_{0.82}$, respectively. The similar approach as synthesis of CdS_xSe_{1-x} nanobelts were employed to grow the ZnS_xSe_{1-x} nanowires. Therefore spatially uniform samples can be achieved. Figure 3.6 g and h show the optical images of samples with uniform composition and non-uniform composition, respectively.

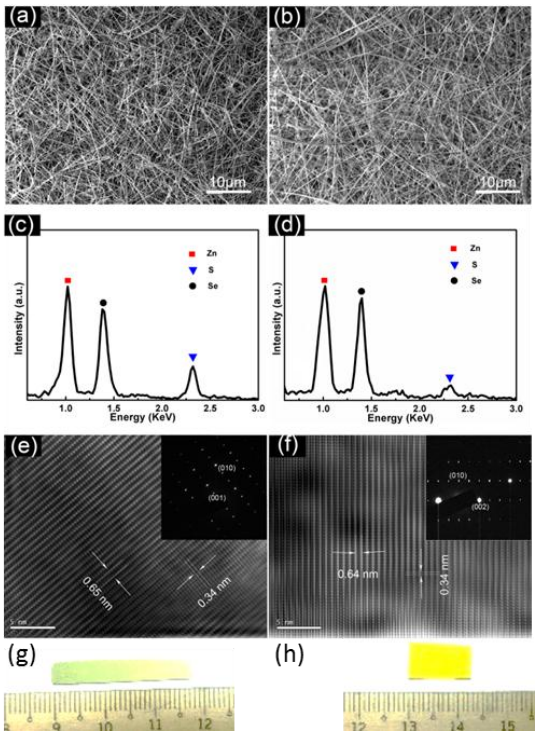

Figure 3.6 SEM images of two ZnS_xSe_{1-x} samples with different compositions (a) x = 0.38. (b) x = 0.18. EDS spectra of (c) $ZnS_{0.38}Se_{0.62}$ and (d) $ZnS_{0.18}Se_{0.82}$. (e) and (f) the corresponding HRTEM of two samples. Inserts are their SAED patterns. Optical images of (g) uniform sample and (h) non-uniform sample.

Figure 3.7 shows the XRD spectra of six ZnS_xSe_{1-x} ($0 \leq x \leq 1$) nanowire samples with different elemental composition. All diffraction peaks can be indexed to the hexagonal wurtzite structure. Figure 3.7a and f correspond to pure ZnS and ZnSe phase respectively (JCPDS: 89-2942 and 89-2940). Their respective lattice constants can be estimated to be $a = 3.82$ Å, $c = 6.26$ Å for ZnS and $a = 4.00$ Å, $c = 6.63$ Å for ZnSe. The peak positions of ZnS_xSe_{1-x} alloys are located in the region between ZnS and ZnSe. From spectra b to e, with the S concentration decreasing (i.e. decreasing x value), the diffraction peaks shift

gradually towards smaller 2θ angles, which indicates an increase of the lattice constants. From Figure 3.7, there is no evidence of any other impurities. These results indicate the formation of high purity, single phase ZnS_sSe_{1-x} ternary alloys with uniform composition stoichiometry. According to Vegard's law,[185] the lattice constants of the ternary alloys show a linear dependence on the composition and is given by, $C_x = C_{ZnS}x + C_{ZnSe}(1-x)$, where C_x, C_{ZnS} and C_{ZnSe} are lattice constants along the c-axis of ZnS_xSe_{1-x}, ZnS and ZnSe, respectively. By using the c-axis lattice constants calculated from the XRD data, the composition x of these ZnS_xSe_{1-x} nanowires can be determined and the estimated values are labeled in Figure 3.7. The gradually shifted XRD spectra indicate alloyed samples with modulated and uniform composition covering the full range from ZnS to ZnSe were successfully obtained.

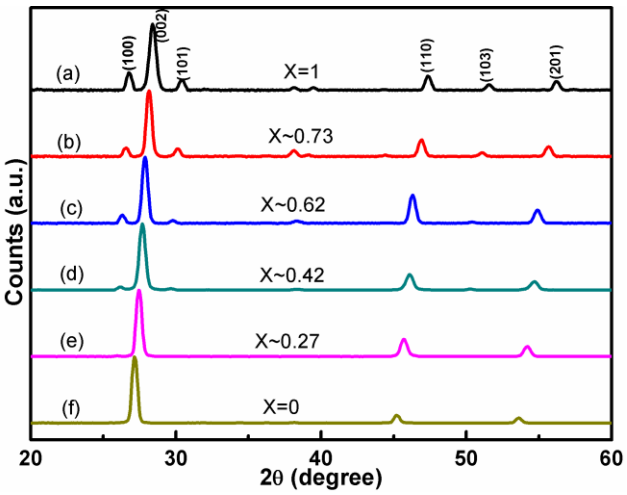

Figure 3.7 Normalized XRD patterns of ZnS_xSe_{1-x} nanowires ($0 \leq x \leq 1$). Spectra (a) and (f) for ZnS and ZnSe respectively. Spectra (b)-(e) for ZnS_xSe_{1-x} samples with different x values.

3.3.3 Growth of Ternary Hybrid Nanostructures

The morphology and structure of the vertically aligned ZnO and ZnO/CdS_xSe_{1-x} core-shell NW arrays were examined with SEM, TEM, and XRD. Part a of Figure 3.8 shows the side view SEM image of the ZnO NW arrays on Si substrate. The average diameter of the NWs is about 90 nm. The SEM image of a representative ZnO/CdS_xSe_{1-x} NWs arrays is shown in Figure 3.8b. From the high-magnification SEM image shown in the insert, the diameter of the core-shell NWs is determined about 200 nm. This indicates the deposited CdS_xSe_{1-x} outerlayers with a thickness of about 50 ± 10 nm. The thickness of the CdS_xSe_{1-x} shells would be easily altered by changing the deposition temperature or growth time. However, as revealed by the low-magnification TEM images of the core-shell NWs shown in Figure 3.8c and d, the thicker outerlayer facilitate a rougher surface. Figure 3.8c shows the NW with a 50 ± 10 nm shell and Figure 3.8d shows a 15 ± 5 nm shell which sheathed uniformly along the ZnO core.

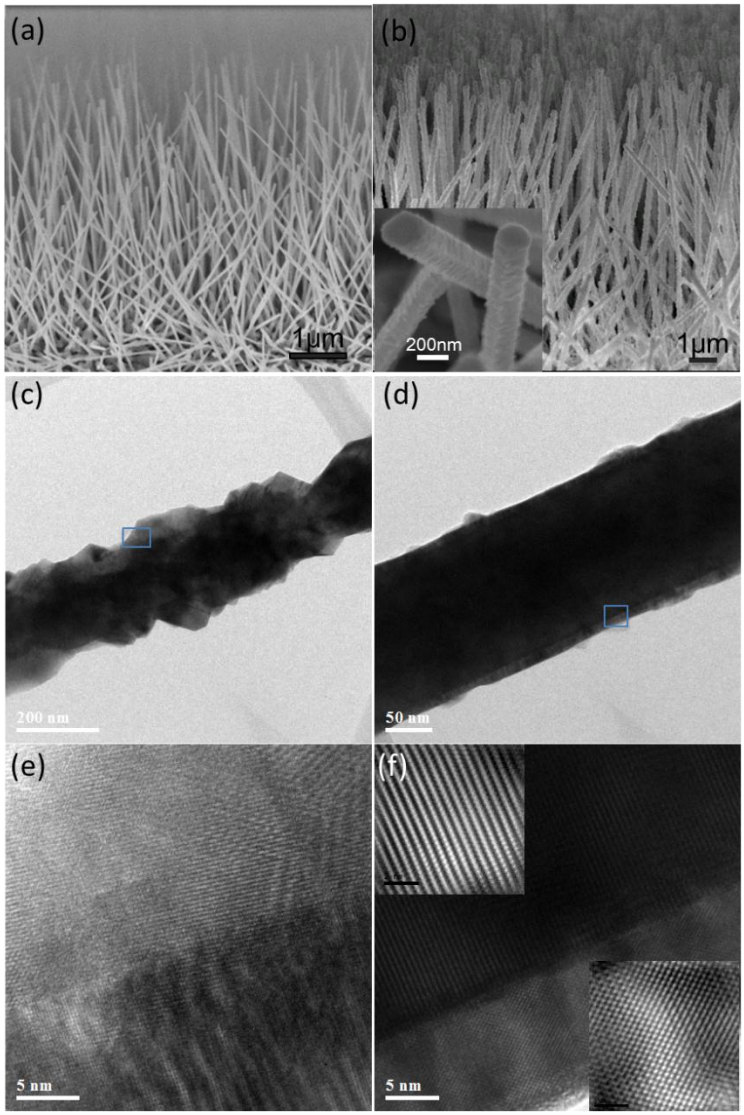

Figure 3.8 SEM images of (a) ZnO and (b) ZnO/CdS_xSe_{1-x} nanowire arrays, insert of (b) shows the high magnification SEM image. Low resolution TEM images of ZnO/CdS_xSe_{1-x} nanowires arrays with (c) thicker shell and (d) thinner shell. HRTEM images of (e) selected area in (c), and (f) selected area in (d). Inserts of (f) show the atomic resolution of the ZnO core and CdS_xSe_{1-x} shell.

The corresponding high-resolution TEM images of interface regions of the two NWs are shown in Figure 3.8e and f, respectively. The two inserts in Figure

3.8f zoom in the TEM images of core and shell regions. Evidently, both the core and shell are single crystalline wurtzite structures and grow along [001] direction with the (001) planes parallel to each other. The distance between the (001) fringes of the core is measured to be 0.52 nm which agrees well with the lattice parameter of wurtzite ZnO. The separation of the (001) fringes of the shell region is about 0.68 nm. Through applying Vegard's law, this CdS_xSe_{1-x} shell is calculated with a x value about 0.65. This result agrees well with the EDX spectrum. The EDS elemental mapping and line scanning profile are shown in Figure 3.9. These results demonstrate the ZnO core and CdS_xSe_{1-x} shell structure.

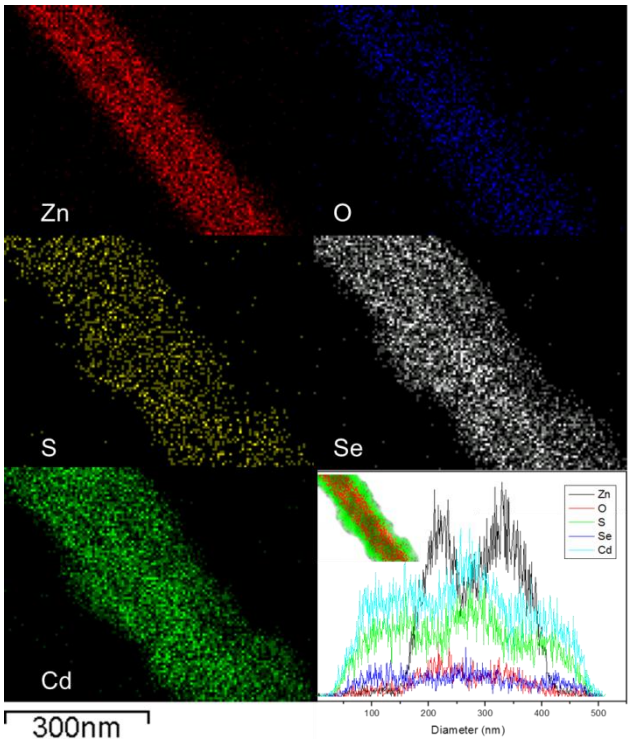

Figure 3.9 EDX mapping elemental line scanning profile of the ZnO/CdS_xSe_{1-x} core/shell nanowire.

In the vapor phase based growth process, chemical stoichiometry of the products can be easily controlled by altering the element concentration in the precursor species or mounting the substrate at different deposition temperature zone.[31, 32] Based on this principle, multifarious alloy nanomaterials were synthesized with tunable band gaps.[46-48, 186-198] Using same idea of composition controlling associated with an *in situ* altering of evaporation ratio of the precursor reagents, single nanowires with gradient composition of several alloy systems can be obtained by employing improved VLS techniques. The improved technique is based on a source-movable horizontal tube furnace. The designed source-moveable set-up is schematically shown in Figure 3.10a. By employing this technique, we synthesized CdS_xSe_{1-x} nanowires with spatial band gaps on single wire, which means the composition of CdS_xSe_{1-x} could be gradually altered along the length of the nanowire.

During the growth process, CdS and CdSe powders were separately loaded in the two ends of a ceramic tube. Subsequently, the end with CdS powder was inserted to the center of the tube furnace. A quartz rod was employed to connect the ceramic boat and a couple of magnet (one inside the tube furnace and one outside). During the growth process, the ceramic boat was continuously shifted towards the downstream by pushing the magnets. Meanwhile, CdSe powder was gradually driven to the furnace center associated with the CdS powder away from the center zone. Simultaneously with the precursor shifting, the temperature was reduced from 800 ºC to 720 ºC. Pure He gas was introduced as the carrier gas with a flow rate of 50 sccm and the pressure was maintained at 50 Torr. The

substrate with 20 nm Au particles as the catalyst was loaded at the downstream. After more than 1 h growth, the furnace was cooled down to room temperature naturally. The products with composition graded CdS_xSe_{1-x} on individual nanowire were collected on the substrate, as displayed by the FM image shown in Figure 3.10b. The precursor shifting is the sticking point of achieving in situ concentration altering of source reagents, thus facilitate the gradient composition along a single nanowire. At the beginning, only CdS powder located at high temperature zone where the precursor could be evaporated. Followed by the evaporation, the CdS nucleated and grew on the substrate. With the CdSe transferred to the furnace center and CdS shifted to lower temperature zone, the CdS vapor concentration decreased and CdSe component began to increase. Thus, the deposition composition along the growing nanowires correspondingly changed with decreased S element and increased Se element. At last, CdS was transferred far away from the high temperature zone and only CdSe could be evaporated and deposited along the grown nanowires. Therefore, the composition and band gap gradient on single nanowire was easily enabled by the precursor-moving growth route.

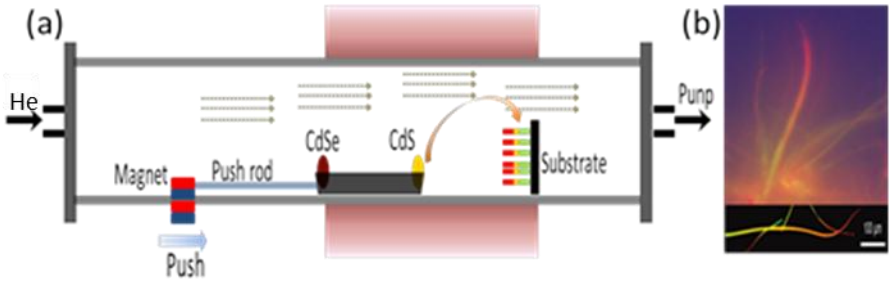

Figure 3.10 (a) Schematic diagram of special designed source-movable tube furnace. (b) Fluorescence microscopy image of composition gradient CdS_xSe_{1-x} nanowires.

3.4 Conclusions

A facile one-step vapor deposition method was employed to synthesize CdS_xSe_{1-x} nanobelts. A simple modification was developed to remove the influence of the temperature gradient on the uniformity of the composition of the 1D ternary alloyed nanostructure. This approach enables the synthesis of single crystal CdS_xSe_{1-x} nanobelts with accurately controlled composition. The micro-morphologies and detailed structures of these nanobelts were studied by scanning electron microscopy, high resolution transmission electron microscopy, X-ray diffraction, and energy-dispersive X-ray spectroscopy. The elements distribution was explored using elemental mapping. All the characteristic results indicate that the nanobelts exhibit high quality single crystalline wurtzite structure. ZnS_xSe_{1-x} nanowires with high uniformity and accurately controlled composition were also successfully synthesized through the similar deposition method. This simple and yet effective approach is expected to be useful in the synthesis of other type of 1D ternary alloys.

High-density ZnO/CdS_xSe_{1-x} core/shell nanowire arrays were synthesized by a second deposition of CdS_xSe_{1-x} outerlayers on pre-synthesized vertically aligned ZnO nanowire arrays *via* the CVD method. Both the composition and the thickness of the CdS_xSe_{1-x} shell-layer can be absolutely controlled and tuned by adjusting the growth conditions in the tube furnace. By changing the molar ratio of the CdS and CdSe source powders, the composition would be tuned from CdS to CdSe *via* CdS_xSe_{1-x}. The thickness would be controlled from 10-50 nm by increasing the growth time or temperature. Moreover, another novel hybrid nanostructure based on ternary CdS_xSe_{1-x} alloy was synthesized by a specially designed thermal evaporation approach. Along the length of a single CdS_xSe_{1-x} nanowire, the chemical stoichiometry can be continuously adjusting from CdS at the bottom end to CdSe at the top end via CdS_xSe_{1-x} at the middle part. These novel ternary II-VI 1D nanostructures are expected to present promising applications on multicolor display and light-emitting devices, ultra-broad spectral photodetectors, and high-efficiency solar cells.

Chapter 4

Fundamentals of Optical Properties in Ternary II-VI 1D Nanostructures

4.1 Introduction

The carrier contribution to the optical properties of semiconductors is facilitated by the transitions of the carriers between the conduction and valence bands. Thus the investigation of optical processes and the corresponding potential device applications require complete understanding and broad knowledge of the band structure of semiconductors. The band structures of II-VI semiconductors of wurtzite, zincblende, and rocksalt polytypes have been theoretically studied with varying degree of complexity. In wurtzite type, one of the most common structures in II-VI binary and ternary semiconductrues, the valence bands arise from the atomic *p*-like states where the symmetry is lower than that in the diamond and zincblende structures. Inversely, the minimum of the conduction band exhibits Γ_7 symmetry with *s*-like state.[199] The valence band is split into three sub-bands due to the spin-orbit coupling and crystal field. This facilitates a series of exciton states. These states are denoted as A (Γ_9, or heavy hole), B (Γ_7, or light hole), and C (Γ_7, or split-off [SO] band), respectively, in the decreasing order of energy.[200, 201] In order to investigate the different excitonic transitions, the selection rules of polarization should be considered.[202] The typical optical techniques, such as low-temperature absorption,[203] reflection,[204] photoreflectance (PR),[205] and photoluminescence (PL) spectroscopy techniques,[146, 206] are usually employed to measure the transition energies of intrinsic excitons.

In this chapter, we will investigate the fundamentals of optical properties in ternary II-VI 1D nanostructures as-synthesized in Chapter 3. The attractive fundamental activities including steady state photoluminescence, time-resolved photoluminescence, ultrafast carrier dynamics, complex photoconductivity, and photon-phonon interactions are reported and studied using various optical characterization techniques. The promising experimental results are expected to promote a deep understanding on fundamental physical process of how the formation of alloys affects the optical properties in the ternary II-VI 1D nanostructures, as well as application interests alike.

4.2 Experimental Method

All the ternary II-VI 1D nanostructures prepared for optical property characterization were grown on C-plane sapphire substrates which are transparent for the probe wavelength in our techniques. The synthesis processes were carried out in a horizontal tube furnace through a VLS growth process as described in Chapter 3. A series of CdS_xSe_{1-x} nanobelts with different composition were prepared by tuning the molar ratio of the source powders of CdS and CdSe. The source was maintained at the maximum temperature of 850 ºC for 30 minutes and the growth pressure was kept at 1 Torr by the pure He carrier gas during the growth process. Various ZnS_xSe_{1-x} nanowires with different compositions were synthesized by changing the ratio of ZnS and ZnSe source powders. The powder evaporation temperature was ramped to 1050 ºC at a rate of 35 ºC/min and maintained at the maximum temperature for 90 minutes. During the whole process, He gas was flowing at a slow rate of 20 sccm to keep the pressure in the

tube chamber at 400 mbar. After the growth time, the furnace was cooled down to room temperature naturally.

The detailed optical property characterization of the nanostructures was carried out using the optical techniques including micro-PL spectroscopy (Renishaw inVia system2000, excitation 325 nm and 532 nm), time-resolved PL spectroscopy, THz-TDS, and OPTP spectroscopy. The time-resolved PL spectra were measured by a 405 nm laser excitation. The PL signal was dispersed by a monochromator (Acton, SpectroPro 2300i) and detected by a liquid nitrogen cooled charge coupled detector. A time-correlated single photon counting system (PicoHarp 300, PicoQuant) was employed to control the time-resolution. The low temperature probing was achieved by a helium compressor cooling system in an optical cryostat. The transmission THz spectra were measured using a THz-TDS system (TeraView Spectra 3000). The terahertz wave was generated by a 800 nm laser with 100 fs optical pulses at a repetition rate of 76 MHz from a mode-lock Ti:sapphire laser focusing onto a low temperature grown GaAs photoconductive antenna. The generated THz pluses were collimated and focused onto the samples by a pair of off-axis paraboloidal mirrors. The transmitted signal was directed to a photoconductive detector. All the operations were carried out in an enclosed chamber purged with dry nitrogen gas to reduce the influence of water adsorption. In the OPTP measurements, the ultrafast optical pump pulse was generated by a Ti:sapphire regenerative amplifier laser system, which can provide ~ 35 fs pulse laser at 800 nm with a repetition rate of 1 kHz. The 400 nm optical excitation pulses were converted from the fundamental output laser by frequency doubled

using a 1 mm thick β-barium borate (BBO) crystal. The THz probe wave was generated by the air-plasma technique and detected using a THz air-biased-coherent-detection (THz-ABCD) route. The pump pulse excited the sample at 30º incidence with different excitation fluences. The THz probe pulses transmitted through the samples at normal incidence. The spot size of the pump beam was about 0.4 cm^2 which was two times larger than that of the THz probe beam. All the measurements were operated in a dry nitrogen purge at room temperature.

4.3 Results and Discussions

4.3.1 Exciton Complex

An exciton is a quasi-particle consisting of the bound state of an electron-hole pair with interaction through the electrostatic Coulombic force. An exciton behaves similarly to a bosonic particle which can freely moves in the crystal lattice of a semiconductor. As compared with free charge carriers, excitons exhibit superior features, such as narrow energy distribution of optical gain, large oscillator strength, and more varieties of possible interactions with electrons and phonons. In addition, excitons have a dynamic electric dipole which can couple with a certain wavelength electromagnetic wave/light. In principle, the coupling between a field (electromagnetic cavity mode) and a particle (exciton) can be employed to achieve zero threshold laser diode.[207] In comparison the bulk counterparts, the electron-polariton coupling strength in nanoscale materials is also significantly enhanced , as was recently demonstrated in CdS nanowire optical cavities.[208]

There are two optical transition processes involving the emission of radiation from semiconductors, *i.e.* luminescence and inelastic scattering of photon (namely, Raman scattering). In a typical luminescence process, electrons in the ground state are excited to a higher energy level, where after the relaxation, the excited electrons return back to the ground state accompanied by the emission of photons. Figure 4.1 schematically illustrates the possible categories of transitions that may occur during a PL process. The realization of these categories depends on the material and experimental conditions such as crystalline quality, temperature and excitation energy.

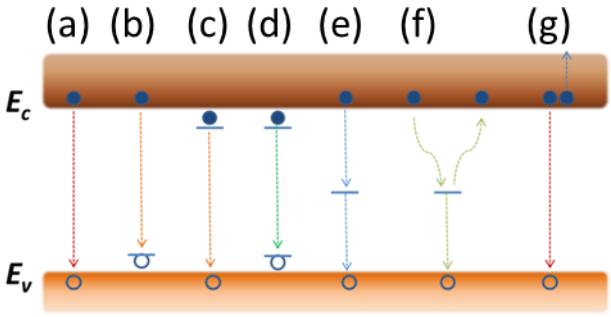

Figure 4.1 Recombination processes in semiconductors. (a) Band-to-band recombination. (b) Band-to-acceptor transition. (c) Donor-to-valence transition. (d) Donor-to-acceptor-pair transition. (e) Recombination *via* a deep center. (f) Non-radiative recombination *via* an intermediate state. (g) Band-to-band Auger recombination.

4.3.1.1 Steady state photoluminescence

PL spectroscopy is one of the most used techniques to probe the optical properties of semiconductors. This is due to the fact that very rich information of both the intrinsic recombination processes and various radiative recombination processes caused by the imperfections of a sample can be revealed by the PL spectroscopy.

As the II-VI ternary compounds exhibit band gap tenability with composition, the PL emission peak can gradually shift with controlled stoichiometry. Figure 4.2a schematically illustrates that the band gap of ternary AB_xC_{1-x} can be continuously tuned from the band gap of binary AB to band gap of AC as the composition *x* decreases. Figure 4.2b shows the normalized PL spectra of CdS_xSe_{1-x} nanobelts of different compositions. Evidently, the nanobelts synthesized in this work exhibit near-band-edge emission peak with narrow line-width and no defect-emission appeared in the spectra. This indicates that the synthesized CdS_xSe_{1-x} alloyed nanobelts are high-quality single crystal with few defects such as dislocations and stacking faults. Obviously, with *x* decreasing, the near-band-edge emission peak positions continuously red-shifts from 507 nm (pure CdS) to 713 nm (pure CdSe) due to the decreasing band gap. Figure 4.2c shows a plot of band gaps of CdS_xSe_{1-x} alloys, calculated from the PL peak positions, *vs* the composition value *x*. As reported,[209] the variation of the band gaps with *x* can be fitted by a quadratic function

$$E_g(x) = E_{CdSe} + (E_{CdS} - E_{CdSe} - b)x + bx^2 \qquad (4.1)$$

where E_{CdS}, E_{CdSe}, and $E_{g(x)}$ indicate the band gap of CdS, CdSe, and CdS_xSe_{1-x} alloys, respectively. *b* is an additional bowing parameter. The best fitting curve

yields b = 0.58 eV. This value is very close to that reported by Hill *et al.*[210] but different from that reported by Adachi.[211] The bowing parameter is a measure of crystal field fluctuation or the nonlinear effect caused by anisotropic binding.[210, 212] The relatively small value of b indicates that the synthesized CdS_xSe_{1-x} alloy nanobelts have good miscibility.

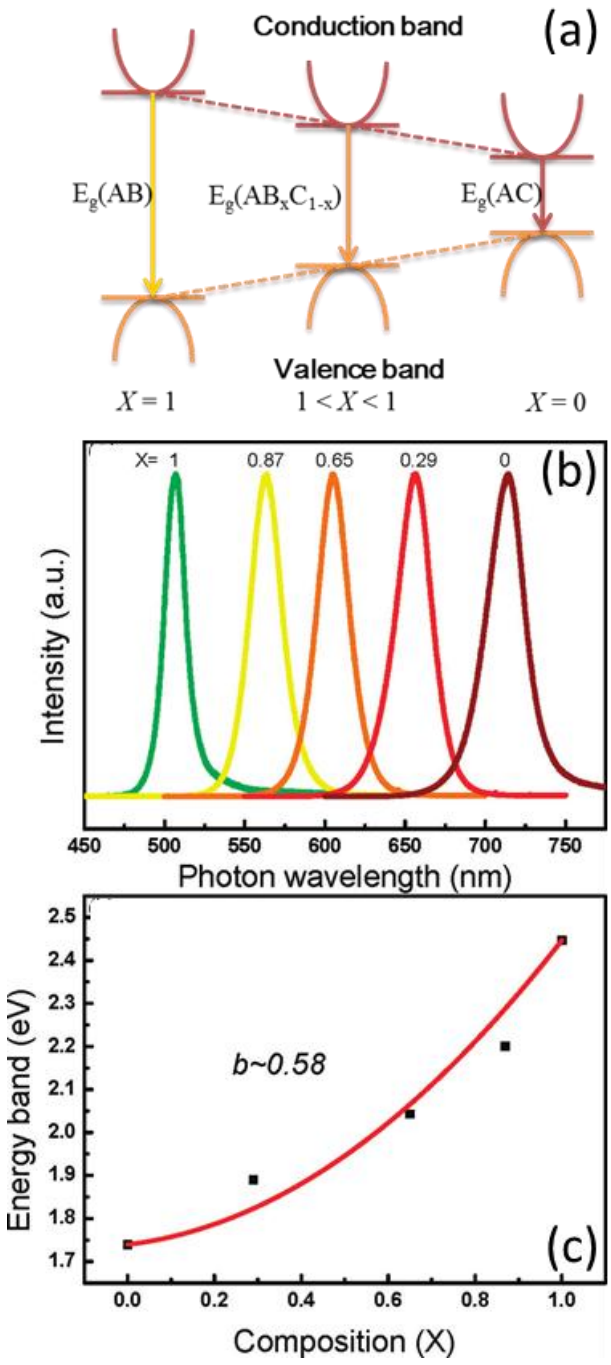

Figure 4.2 (a) Band gap engineering of ternary semiconductors. (b) PL spectra of CdS_xSe_{1-x} nanobelts of different compositions. (c) Band gap energy as a function of composition.

By employing low temperature PL spectroscopy, detailed information of the semiconductor properties (such as exciton, phonon, and donor binding energy) would be obtained. These parameters are very helpful in giving a clear picture of the optical quality of a semiconductor material.[213] Figure 4.3a shows the PL spectra of CdS_xSe_{1-x} nanobelts at 300 K and 30 K, respectively. At room temperature, PL spectra of all nanobelts are alike and show a single peak with full width at half maximum of 81.4–91.4 meV. However, the low temperature PL spectra of these nanobelts differ significantly from those observed at room temperature. For pure CdS (CdSe), two emission bands are observed at 30 K: the high-energy band at 2.546 eV for CdS (1.818 eV for CdSe) and the low-energy broad band at 2.48 eV (1.78 eV), which is ~60meV (40 meV) lower in energy. Due to the crystal-field and spin-orbit coupling, the valence band of CdS splits into three sub-bands, leading to three exciton levels with characteristic energies of E_A = 2.550 eV, E_B = 2.568 eV, and E_C = 2.629 eV.[214-216] The high-energy band in the spectrum is centered at around 2.546 eV, which is close to the A exciton value, with a red- shift of ~4 meV. The emission band at 2.546 eV in CdS nanobelts are assigned to neutral donor bound excitons. Similar conclusion was also reported by Thomas and Hopfield in CdS platelets. In their studies, besides intrinsic exciton peaks, many peaks are actually caused by transitions involving bound excitons,[217, 218] which are created when excitons are bound to neutral/charged donors or acceptors. Recent reports of CdS nanobelts by Ip *et al.*[219] and Xu *et al.*[220] show a similar emission peak near 2.545 eV and 2.543 eV, respectively, and those were also attributed to the exciton bound to a neutral donor. Similarly, the high-

frequency emission band observed for CdSe nanobelts at 1.819 eV also originate from exciton bound to a neutral donor. And the results are consistent with those reported by Gourdon *et al.*[221] The broad low-energy peak can be ascribed to the emission related to surface defect states, which are usually 20–80 meV lower in energy than the near band-edge emission.[222] Interestingly, such surface defects related emission almost disappears for all ternary CdS_xSe_{1-x} samples. It can only be observed by elaborate curve fitting of these slightly asymmetrical emission bands, suggesting that much weaker surface emission occurred in ternary CdS_xSe_{1-x} nanobelts. The largely reduced surface emission was mainly attributed to the carrier localization caused by composition disorder in ternary CdS_xSe_{1-x} as described by the Mott-Anderson localization theory[223] as well as the formation of type-I core-shell-like heterostructure during the ternary alloy synthesis process as analyzed in ref 16.

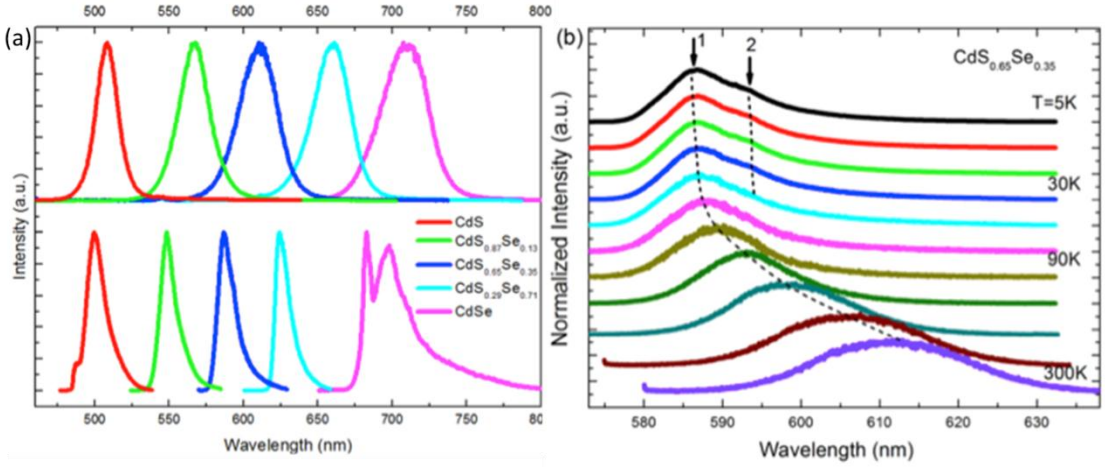

Figure 4.3 (a) Normalized PL spectra of CdS_xSe_{1-x} nanobelts at 300 K (up) and 30 K (down), respectively. (b) Temperature-dependent PL spectra of $CdS_{0.65}Se_{0.258}$ nanobelts from 5 K to 300 K.

Due to the difference of their densities of state (DOS), the relative PL intensity of the defect and exciton transition presents a very different trend with the variation of temperature. As shown in Figure 4.3b the PL spectra of $CdS_{0,65}Se_{0.35}$ nanobelts at a series of temperatures from 5 K to 300 K are presented. With the change of the sample temperature, a redshift of the emission peaks of semiconductors can be observed. The shrinkage of the band gap is related to exciton-phonon interactions as well as the thermal expansion.[140, 224]

4.3.1.2 Ultrafast Spectroscopy

For ternary II-VI compound nanomaterials with high exciton binding energies, excitons are typically generated from optical absorption. The generated non-equilibrium carriers will choose decay paths (either radiative or non-radiative) to return to equilibrium.[225] Ultrafast spectroscopy, such as time resolved photoluminescence (TRPL) spectroscopy, optical pump-probe absorption, reflection, transmission, or second harmonic generation (SHG) spectroscopy, is a highly sensitive techniques that can be employed to monitor the decay processes experienced by those carriers, in which case, the time required by the carriers traversed in each path (*i.e.*, exciton lifetime) can be measured, and the fundamental mechanism of the energy loss from the interactions (such as, by exciton-exciton, electron-exciton, exciton-phonon, or electron-phonon interactions) can be clearly understood.

Exciton lifetime is highly sensitive to crystal quality, where the lifetime will be longer for samples with improved crystal quality and reduced defect density.

We have reported a tri-exponential decay for ternary CdS_xSe_{1-x} nanobelts with different composition from $x = 1$ to $x = 0$ at different temperature conditions,[213] as shown in Figure 4.4. These decay components indicated the excitons recombine through different recombination paths. We suggested that the first (fast) decay component arises from a very fast exciton's transfer from interior of nanobelts to surface; the second (intermediate) decay is from the recombination of localized excitons; and the third (slow) PL decay one originates from the near band edge recombination. However, the PL decay profiles of ternary CdS_xSe_{1-x} nanobelts at 5K show bi-exponential behaviors rather than tri-exponential behaviors, and display much longer decay time of excitons recombination, which are quite different from that of binary CdS and CdSe nanobelts. The absence of the very fast process of exciton transferring from interior to surface in CdS_xSe_{1-x} alloy nanobelts indicates the reduced significance of surface defect. Since binary (CdS and CdSe) nanobelts have more surface defect states than ternary alloy nanobelts, a larger number of excitons in CdS and CdSe nanobelts can migrate to the surface without localization in the interior of nanobelts at low temperature, resulting in tri-exponential behavior. These results of PL dynamics of CdS_xSe_{1-x} nanobelts demonstrated that the formation of ternary alloys can efficiently reduce the surface defect density and improve the luminous efficiency of nano-scaled light-emitting devices. Moreover, the lifetime of band edge emission does not exhibit any clear trend with variable Se or S contents in CdS_xSe_{1-x} alloy nanobelts. This is in agreement with both Gadd's observation[226] in bulk CdS_xSe_{1-x} and

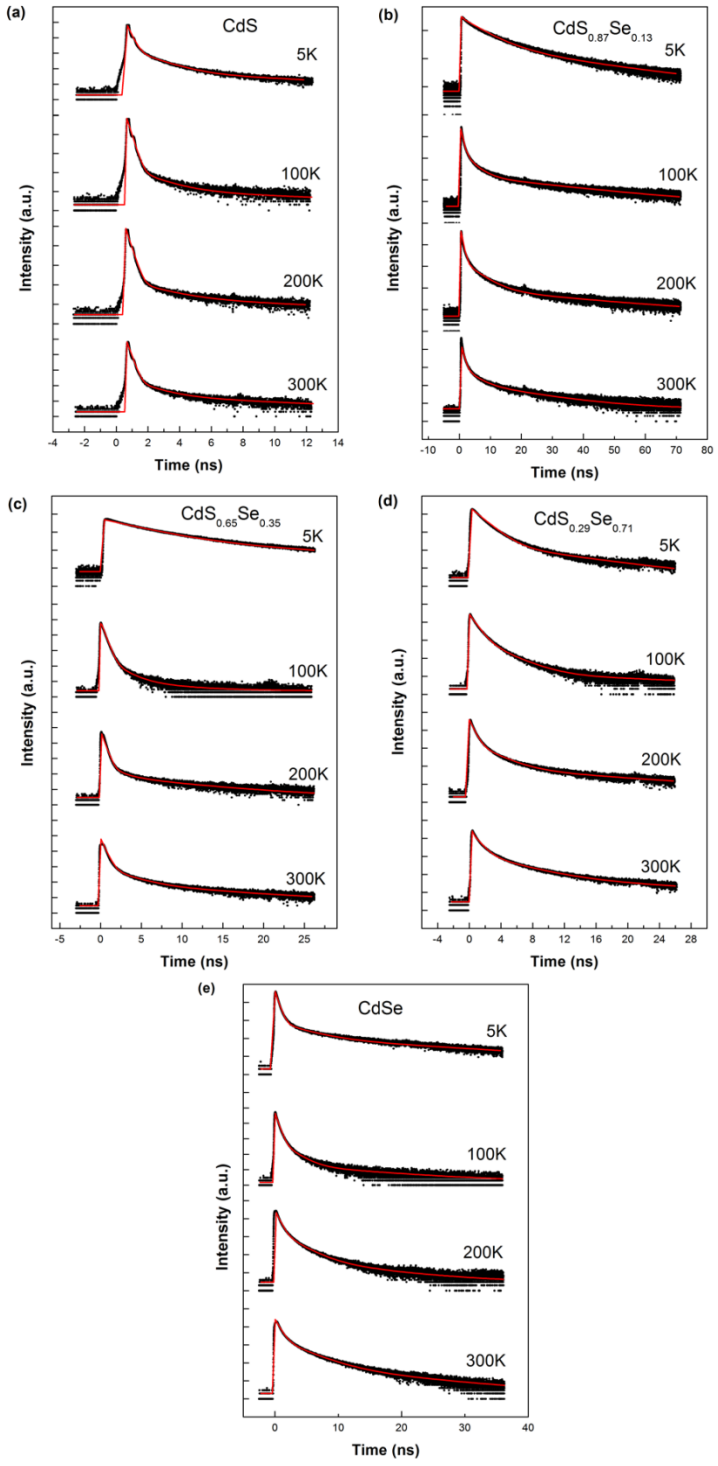

Figure 4.4 Time-resolved PL spectra with fits of five CdS_xSe_{1-x} nanobelt samples at different temperature.

Hane's results[227, 228] of bulk CdSe/S graded alloys, but differs from that observed in nanocrystals.[229]

Optical pump-terahertz (THz) probe (OPTP) spectroscopy is an important tool to investigate the quasiparticle dynamics in nanostructures on time scales that range from sub-picosecond to nanoseconds.[230] Recent studies of nanomaterials [231-233] have demonstrated that OPTP spectroscopy possess a number of advantages compared with other ultrafast techniques. In comparison to TRPL technique, OPTP spectroscopy would avoid some drawbacks, for instance that the measurements of TRPL are often hindered by a large defects density which would reduce the photoluminescence efficiency.[234] As compared to other common ultrafast spectroscopy techniques, the powerful nature of OPTP spectroscopy stems from the facts that it is a coherent technique that can make both amplitude and phase measurements, which reveal a wealth of information about materials that interact with THz wave, while the typical charge carrier scattering time is in picosecond range which corresponds to THz frequency range in the electromagnetic spectrum, as shown in Figure 4.5. This enables the radiation in the THz frequency range interacts in a specific manner with charge carriers, facilitating THz radiation the ideal probe for charge carriers in materials. In addition, OPTP spectroscopy is effective in elucidating the defect-related trapping process due to the high sensitivity of THz probe to the carrier density and mobility.[235, 236]

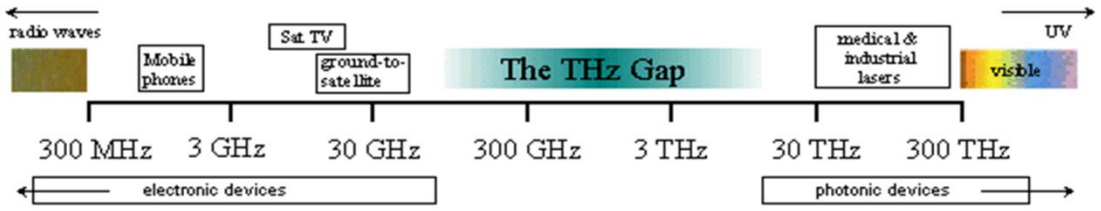

Figure 4.5 THz frequency regime in electromagnetic spectrum.

We reported a study on the carrier dynamics in CdS and CdS_xSe_{1-x} nanobelts using OPTP spectroscopy,[237] as shown in Figure 4.6. The transient differential transmission, $\Delta T/T_o$, as shown in Figure 4.6, can be well fitted by a biexponential function

$$\Delta T/T_o = A_1 e^{-t/\tau_1} + A_2 e^{-t/\tau_2} \tag{4.2}$$

where τ_i is relaxation time constant, and A_i is the weighting factor. The OPTP results reveal a clear picture for the complicated relaxation dynamics of photocarriers. According to the excitation fluence dependence, the biexponetial relaxation processes affecting such dynamics are attributed to surface defect related trapping and structural-defect-related recombination. For the fast decay process, both CdS and CdS_xSe_{1-x} nanobelts present distinct excitation fluence dependence. Especially, the fast process disappeared in CdS_xSe_{1-x} sample at low excitation fluence and the experimental data can be fitted with monoexponential curves. From the excitation fluence dependence law, two possible origins, surface defect trapping and Auger recombination are assumed here. Figure 4.7a displays the fast decay time of CdS and CdS_xSe_{1-x} as a function of photocarrier density, N_e,

where $N_e \propto [(1+\Delta T/T_o)^{-1}-1]$, while Figure 4.7b shows the $\Delta T/T_o$ of slow decay process *versus* excitation fluence.

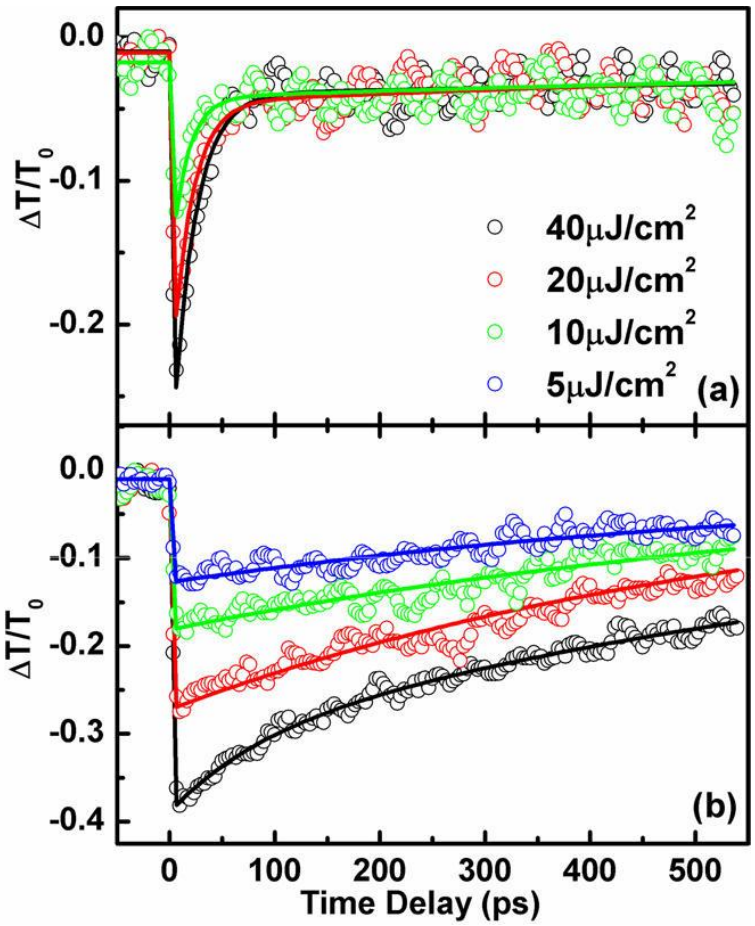

Figure 4.6 Excitation fluence dependence of time-dependent differential THz transmission for (a) CdS and (b) CdS_xSe_{1-x} nanobelts. The solid lines are best exponential fitting results.

Auger recombination varies with a lifetime following a quadratic law $\tau_{Auger}^{-1} \sim N_e^2$; therefore, the lifetime of Auger recombination should decrease with excitation fluences. Nevertheless, both the τ_{1CdS} and τ_{1CdSSe} shown in Figure 4.7a increase with increasing excitation fluence; thus, the fast decay process can be attributed to

surface defect trapping rather than Auger recombination. The increase of decay time with excitation fluence is due to surface trap saturation. At lower excitation fluence, photocarrriers are trapped by surface defects, while the available trapping sites will become fully occupied at higher fluence, resulting in a longer decay time.

On the other hand, the slow process shown in Figure 4.6a and b does not present distinct excitation fluence dependence, indicating that the carrier decay is mainly attributed to the structural-defect-related nonradiative recombination or band-to-band recombination. The slow process of CdS and CdS_xSe_{1-x} can be measured to be 1000 ps and 894 ps, respectively. The faster decay of CdS_xSe_{1-x} sample indicates that the carrier decay is dominated by defect-related recombination, since CdS_xSe_{1-x} is expected to have higher defect densities. It is noticed that the decay curves of CdS nanobelts coincide in the decay time from 90 to 500 ps as shown in Figure 4.6a, indicating $\Delta T/T_o$ saturated readily even at low excitation fluence during the slow decay process. Figure 4.7b presents that the $\Delta T/T_o$ at 300 ps of CdS nanobelts (red dots) does not dependent on the excitation, while $\Delta T/T_o$ of CdS_xSe_{1-x} exhibits an exponential dependence ($\Delta T/T_o \propto (1-e^{-I/I_o})$) on the excitation fluence at the low decay process. The excitation independence of CdS is caused by its low structural defects concentration, where the high photocarrier density exceeds the density of available structural trap states.

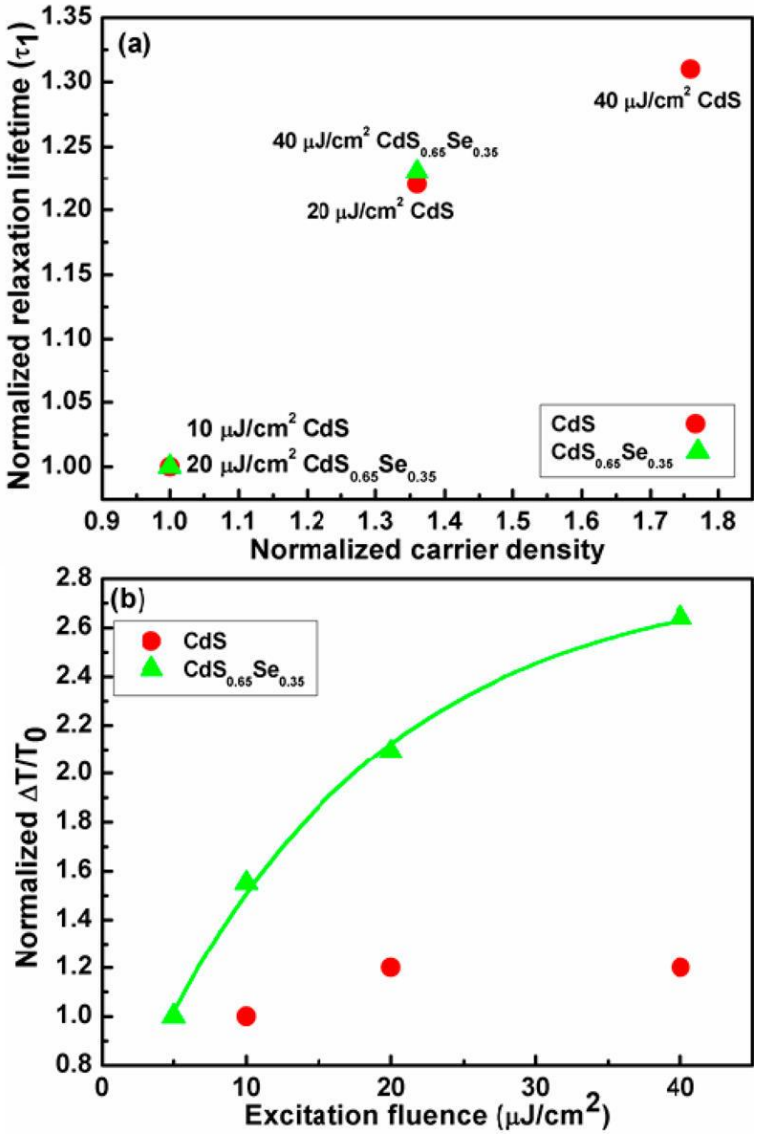

Figure 4.7 (a) Fast decay time τ_1 as a function of photocarrier density. (b) $\Delta T/T_o$ at t = 300 ps as a function of excitation fluence.

Specifically, surface defects dominate the carrier relaxation path in CdS while the dominant decay path is structural defect related recombination after the formation of ternary alloys. Therefore element replacement is an effective approach for defect-distribution restructuring, which would improve the luminous efficiency of nano-scaled light-emitting devices and facilitate high optical

conductivity of optoelectronic devices through reducing or avoiding surface defect trapping.

4.3.2 Complex photoconductivity

In order to realize photoelectronic devices with technologically useful performance, great efforts have been dedicated into this research field of photoconductivity to find new photoconducting materials with improved properties. Using a material in its nanoscale counterparts has been exhibited to improve greatly the photoconductivity in both carrier density and transport, which are the two basic processes involved in the study of photoconductivity. The high crystalline quality of nanomaterials can reduce the scattering in the electron transport process while the large surface to volume ratio will strengthen the significance of surface states, which would enhance the recombination rate and thus increase the response speed. Additionally, the large surface to volume ratio will also improve the trapping of charge carrier to enhance the sensitivity further, due to the more pronounced depletion region near the surface. In this section, ternary CdS_xSe_{1-x} alloy nanobelts are demonstrated as a new photoconducting material with more significant photoconductivity than binary CdS and CdSe.

Photoconductivity measurement in nanostructures, however, is a challenging problem due to the inherent difficulty in attaching electrode to nanometer-scaled objects. Currently, many reports on the probing of photoconductivity of nanowires/belts employed expensive and complex precision lithography methods to fabricate contact electrodes on the nanowires.[157, 238-241]

Naturally, the observed photoresponse of their samples depends on the interplay of the intrinsic response of nanobelts, nanobelts−nanobelts and nanobelts−electrode contact barriers.[239] Given the wide diversity of contributing factors to the experimentally obtained results in a typical contact-based photoconductivity experiment, interpretation of the observed phenomena would prove to be challenging. To answer this challenge, Time-resolved THz time-domain spectroscopy (TRTS) has been demonstrated to be an excellent noncontact electrical probe technique capable of measuring the photoconductivity of nanoscaled semiconductors without the cumbersome process of making contacted sample.[242] The TRTS was carried out using the same optical setup as shown in Chapter 2. Here, we employ TRTS as an excellent technique to study the photoconductivity of ternary CdS_xSe_{1-x} nanobelts with various compositions ($0 \leq x \leq 1$). The results demonstrate ternary compounds exhibit much enhanced photoelectronic properties in comparison to their binary counterparts (CdS and CdSe). To probe carrier dynamics in nanobelts, the excited states were photogenerated via a pulse from a femtosecond laser, while the complex photoconductivity can be extracted from a delayed single-cycle pulse of THz radiation. The broad bandwidth of THz waves enables the characterization of complex photoconductivity of samples covering a frequency range comparable to momentum scattering rate and typical plasma frequencies in semiconductors.[230] Figure 4.8 shows the collected time-domain spectra of two representative CdS_xSe_{1-x} samples before and after exciation at a given pump-probe delay time point.

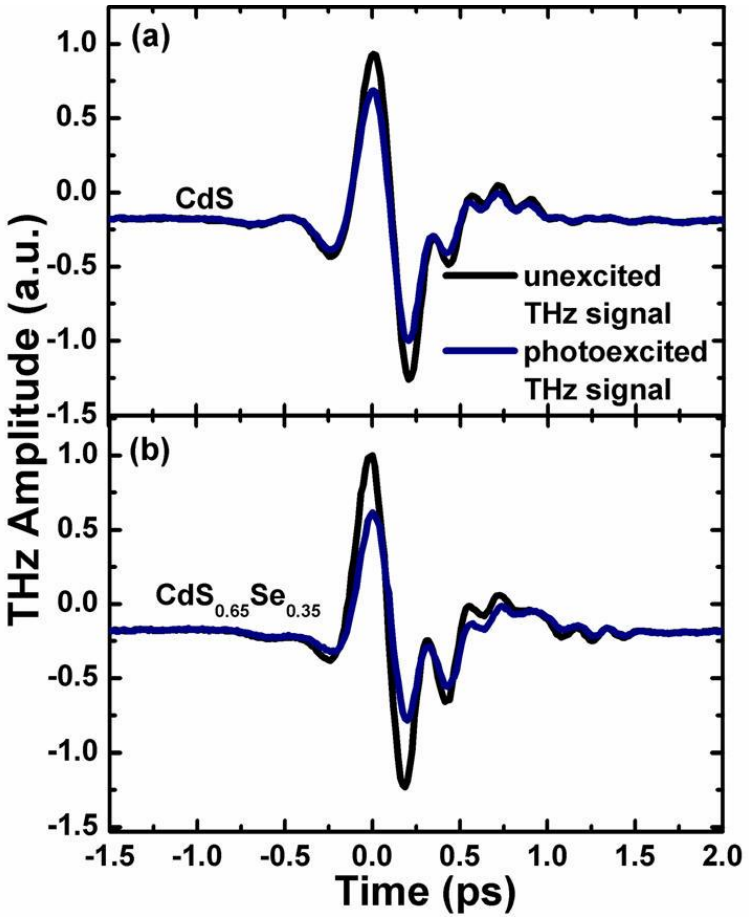

Figure 4.8 Time-dependent THz pulses transmitted through (a) CdS and (b) CdS_xSe_{1-x} nanobelts. The black and blue curves represent the transmitted THz pulses before and after photoexcitation, respectively.

The information of photoinduced conductivity $\Delta\sigma(\omega,t)$ can be extracted from the recorded transient change in terahertz transmission. The expression of photoconductivity is derived as,

$$\Delta\sigma(\omega,t) = -\frac{\varepsilon_0 c(n_1+n_2)}{d}\frac{\Delta\tilde{E}_{sam}(\omega,t)}{\tilde{E}_{sam}(\omega)} \tag{4.3}$$

where *t* is the pump-probe delay time, ε_0 is free space permittivity, *n* is refractive index, *c* is speed of light, *d* is thickness of sample and ω is the radial frequency. The extracted complex photoconductivity spectra of six CdS_xSe_{1-x} samples (x = 1, 0.87, 0.75, 0.65, 0.29 and 0, respectively) are shown in Figure 4.9. The experimental data are best fitted by the Drude-Smith model, which is a correctional Drude model employed to present the carrier conductivity in nanostructures and is described by[243]

$$\sigma(\omega) = \frac{\varepsilon_0 \tau_0 \omega_p^2}{1 - i\omega\tau_0}\left(1 + \frac{c}{1 - i\omega\tau_0}\right) \tag{4.4}$$

where $\omega_p^2 = Ne^2/(m^*\varepsilon_0)$ is the plasma frequency, in which N_o is free carrier density, *e* is the charge of single electron and m^* is the electron effective mass. τ is the scattering time between collisions.

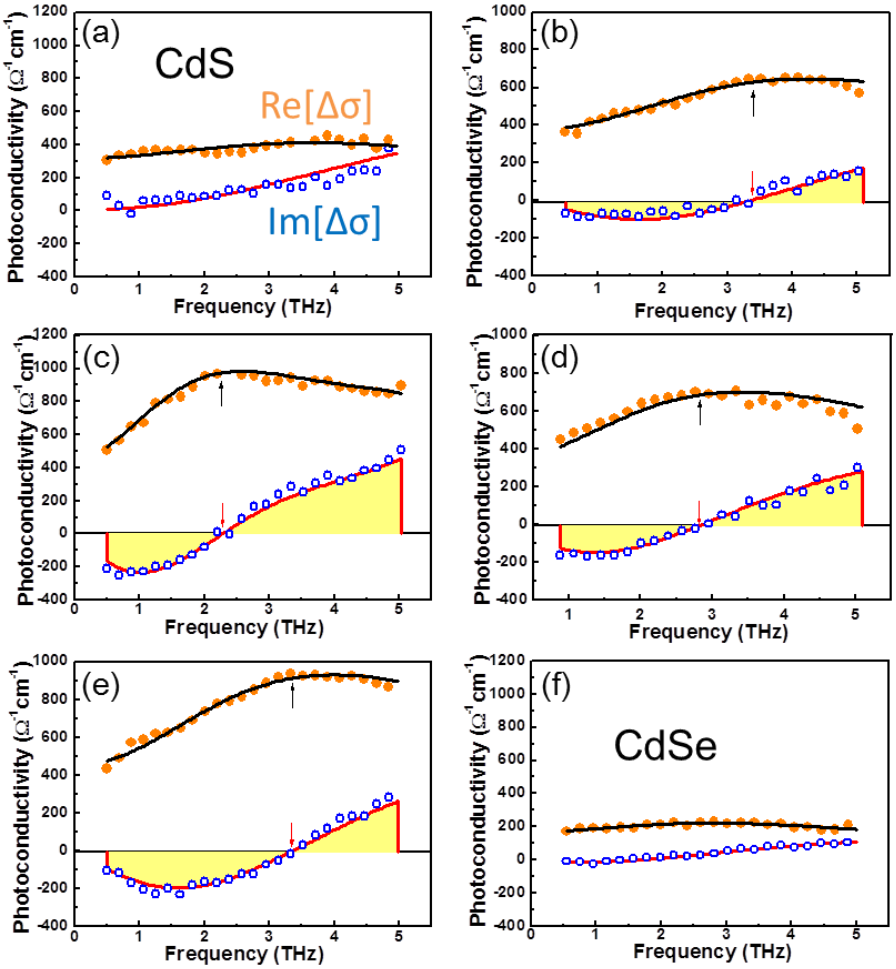

Figure 4.9 Complex photoconductivity of six samples (x= (a) 1, (b) 0.87, (c) 0.75, (d) 0.65, (e) 0.29, and (f) 0, respectively) recorded at t = 3.5 ps. The solid lines are Drude-Smith fitting curves.

The broad bandwidth of THz waves enables the characterization of complex photoconductivity of samples covering a frequency range comparable to momentum scattering rate and typical plasma frequencies in semiconductors.[230] Here, the real part of the photoconductivity (solid circles) may be considered as the resistive response of the nanobelts, with the imaginary part as an additional

inductive or capacitive response.[233] The real part photoconductivity (Re[Δσ]) of all nanobelts are positive but ternary CdS_xSe_{1-x} nanobelts show larger Re[Δσ] values than those of binary CdS and CdSe nanobelts, indicating the higher responsivity to light of ternary nanobelts and revealing their great potentials in photoelectronic applications. The corresponding values of Re[Δσ] at 2 THz as a function of composition are plotted in Figure 4.10a. As shown, CdSe nanobelts present the minimum Re[Δσ] value while $CdS_{0.75}Se_{0.25}$ show the maximum value, which is consistent with our previous photoresponse experiment with applied bias under light illumination.[244] Furthermore, the real part photoconductivity has no distinct frequency dependence, which indicates the presence of photoinduced free carriers possessing a large scattering rate in CdS and CdSe nanobelts. However, in ternary CdS_xSe_{1-x} nanobelts, a broad peak appears in the real part accompanied with a corresponding zero crossing in the imaginary part of photoconductivity (as illustrated by black and red arrows in Figure 4.9(b)-(e)). The frequency of this feature is located at low frequency region when "S" and "Se" are comparable and shifts to high frequency region when "S" or "Se" is rich. The appearance of this feature is attributed to excitonic transition.[245] In short, the transformation of photoexcited unbound *e-h* pairs into excitons requires a transient phonon bath into which the momentum and binding energy can be permanently released. Due to the higher photogenerated free carrier densities (Figure 4.10b) in ternary CdS_xSe_{1-x} nanobelts, the features are revealed more obviously in ternary nanobelts spectra. The photocarrier densities are obtained from the best fitting (solid lines in Figure 4.9) parameters. Both the photocarrier density and the corresponding free electron

mobility are plotted as a function of composition *x*, as shown in Figure 4.10b. The higher photocarrier density of ternary CdS_xSe_{1-x} nanobelts also provides a certification for their large real part photoconductivity values. Conversely, the mobility of photocarriers in binary CdS and CdSe is higher than that in ternary CdS_xSe_{1-x} nanobelts. This is possibly attributed to the Anderson localization[223] or the higher chance of excition formation in CdS_xSe_{1-x} nanobelts.

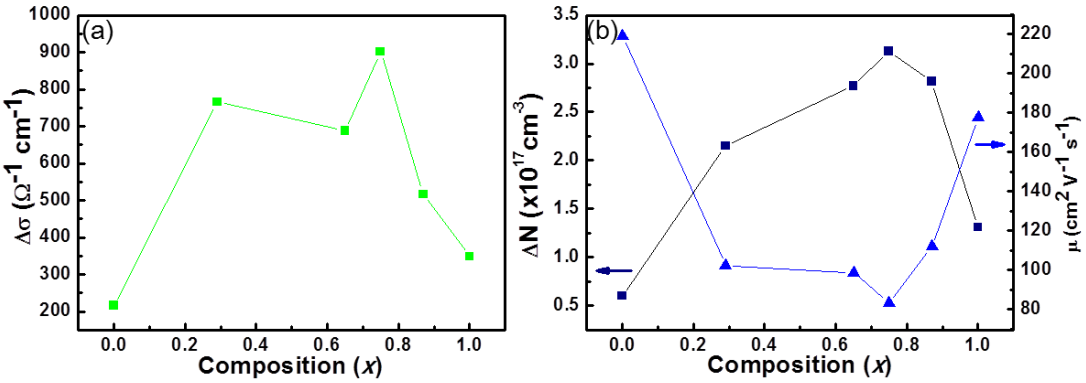

Figure 4.10 (a) Real part of photoconductivity at 2 THz plotted as a function of composition. (b) Photocarrier density (ΔN) and photocarrier mobility plotted as a function of composition.

4.3.3 Phonons

Phonons are often referred to as quasiparticles, which represent the quanta of lattice vibrations. They play a major role in many of physical properties of solid bulk- and nano-materials, including a material's thermal, electrical, and optical properties[246], as phonons carry energy and interact with electrons and among themselves *via* phonon-electron and phonon-phonon interactions, respectively. The importance of phonons in nanostructures are also demonstrated

in various interesting phenomena, such as anisotropy of electron-phonon interaction and phonon confinement in single nanowires,[247-249] surface resonant Raman scattering,[250] phonon bottleneck effects in nanoscaled electronic devices,[251] and determination of carrier mobility.[246] In theory, the frequency and dispersion relation of phonons can be calculated from solving the lattice dynamics equation. Because the vibrational modes of phonons are either Raman-active or IR-active, the Raman spectroscopy and infrared absorption or transmission spectroscopy are complementary techniques in the experimental measurement for assignment of vibrational modes.

4.3.3.1 Raman spectroscopy

Since its discovery,[252] Raman spectroscopy is one of the most effective spectroscopic techniques to investigate phonons and other element excitations in solid state physics. Raman spectroscopy is highly sensitive and non-destructive. It can probe the samples on the order of a few nanometers covering a broad excitation energy range from UV to NIR. The first order inelastic Raman scattering process involves two photon events that comprise the simultaneous annihilation of an incident photon and the generation of a scattered photon, modulated by the electron-phonon and electron-photon interactions.[253] During this process, the conservation of momentum and energy would be obeyed simultaneously. In the visible or NIR regime, the photon momentum (wave vector) is less than 10^6 cm^{-1} and this is much smaller than the magnitude of phonons corresponding to the Brillouin zone boundary of typical crystals. Therefore, the first-order process only involves phonons and other elementary excitations at or

near the Brillouin zone center, which is the well-known $\vec{q} = 0$ Raman selection rule.

In 1D nanomaterials, the shape of phonon dispersion relation will be obtained from folding the bulk material Brillouin zone. However, some new modes (*e.g.* surface phonons) will emerge due to the interface and surface vibrations in nanostructures, which would become more significant with the increasing surface to volume ratio due to the decrease of size. The formation of surface optical phonons in 1D nanomaterials usually indicates the breading of some translational symmetry, since surface optical phonons are generally non-activated due to the momentum conservation.

Here, we report the systematic study of the Raman spectra from 1D ternary CdS_xSe_{1-x} nanobelts.[187] The results are shown in Figure 4.11a. The phonon peaks were fitted and separated by Lorentz function. From CdS Raman spectra, the peaks at 236, 256 and 307 cm^{-1} are assigned to A_1 (TO), E_2^H and LO modes respectively. Whereas the peaks at 215, 326, 350, 367, and 600 cm^{-1} (2LO) arise from multiphonon scattering[254] and additions of optical phonons give a broad band around 590 cm^{-1}. The broad and weak peak at 299.5 cm^{-1} comes from surface optical mode.[255] From CdSe Raman spectra, the peaks at 212 and 419 cm^{-1} are assigned to LO and 2LO modes. The weak peaks at 175, 203.5 and 235 cm^{-1} are attributed to TO, surface mode and vibrational mode of –Se–Se–Se– chains.[256] CdS_xSe_{1-x} is classified as an alloy with two-mode behavior. That means the first-order Raman spectra of the alloyed ternary crystals exhibit both CdS- and CdSe-

like phonons.[255] As seen from the spectra (Figure 4.11b and c), the alloyed nanobelts exhibit CdS-like LO_1 and CdSe-like LO_2 modes at ~200 and ~300 cm^{-1}. In addition, $2LO_2$ peak at ~600 cm^{-1} is observed. Furthermore, the asymmetric and broad peak near 480 cm^{-1} is assigned to LO_1+LO_2 band. With the S-fraction in the alloy increasing from x=0.29 to x=0.65, the LO_2 phonon intensity decreases and the peak shifts downward from 204 cm^{-1} to 197 cm^{-1}, while the LO_1 phonon intensity increases and peak position shifts upward from 289 cm^{-1} to 298 cm^{-1}. Simultaneously, the LO_1+LO_2 band peak shifts a bit from 487 cm^{-1} to 485 cm^{-1}. This behavior of Raman lines shifts is due to the variation of the chemical composition.[257] Moreover, the peaks labeled ahead of the LO peaks are assigned to surface optical modes for CdS and CdSe. Finally, the surface optical peaks at 180.8 cm^{-1} in Figure 4.11b and 194.5 cm^{-1} in Figure 4.11c become prominent, which has been explained by the increasing role of surface phonons.[258, 259] Surface phonon modes are localized on the surface or propagating only along the interface of a structure, which are actually the solution of Maxwell's equations with appropriate boundary conditions.[260] Surface phonon modes are usually Raman-non-active because of the constraint of momentum conservation. They would be Raman-active only if the surface translational symmetry is broken. Nevertheless, surface phonon modes can now be optically observed in nanostructures because the size modulation will facilitate surface translational asymmetry along a specific dimension. This provides the momentum enable activate surface modes in Raman scattering. Generally, Raman spectrum only detects optical modes since the light

momentum is close to the wave vector of optical mode at or near the center of the Brillouin zone, thus they are defined as surface optical (SO) phonons.[261]

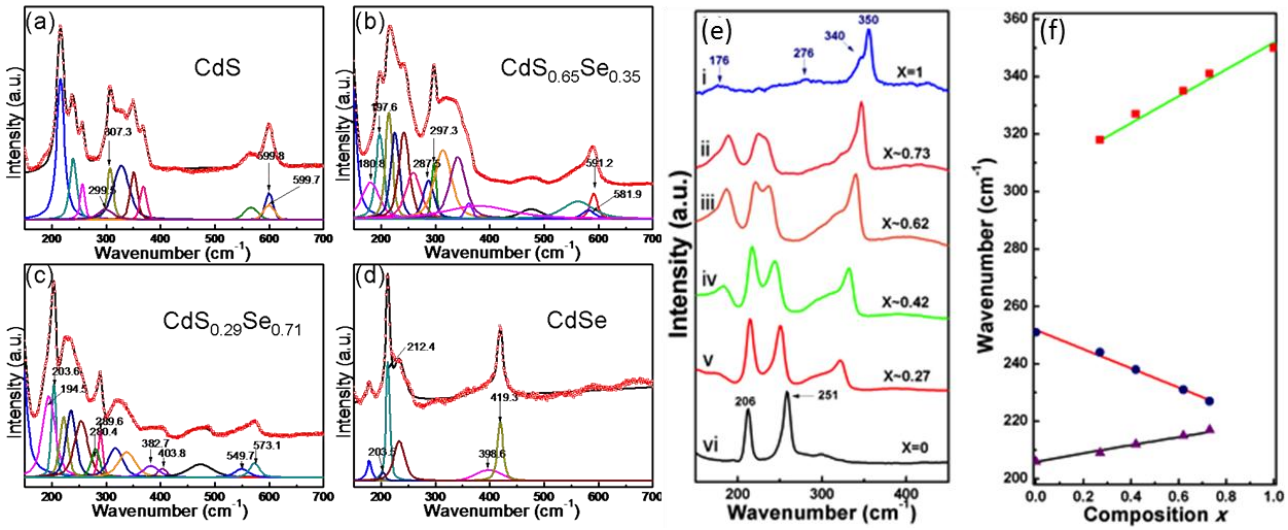

Figure 4.11 Raman spectra of (a)-(d) CdS_xSe_{1-x} nanobelts, and (e)-(f) ZnS_xSe_{1-x} nanowires.

Besides the Raman spectra of CdS_xSe_{1-x} nanobelts, the Raman-active phonons of ZnS_xSe_{1-x} nanowires are also reported here. The Raman spectra of six ZnS_xSe_{1-x} nanowire samples are displayed in Figure 4.10e. Similar to the CdS_xSe_{1-x} results, the alloyed nanowires also present a typical two-mode behavior[262]. In addition, the optical phonon frequencies vary with the variation in composition. Figure 4.11f shows the experimental concentration dependences of the frequencies of vibration in ZnS_xSe_{1-x} nanowires. Evidently, both ZnS- and ZnSe-like modes are in well agreement with the calculations from modified random-element-isodisplacement model[263, 264]. Despite of the gradual shifts, LO_1 peaks asymmetrically broaden with a low frequency shoulder with decreasing *x* value. This phenomenon is attributed to alloy potential fluctuations and can be

explained by a "spatial correlation" model[265], related to *q*-vector relaxation caused by the alloy disorder. The alloy potential fluctuations destroy translational invariance and induce a breakdown of the usual $\vec{q} = 0$ Raman selection rule, thus leading to the asymmetry and broaden the shape of ZnS-like LO.

4.3.3.2 Terahertz time-domain spectroscopy

The IR-active phonon modes with low-frequency have been demonstrated to show sensitive response to THz-TDS. Based on this reason, THz-TDS has been successfully employed to probe the IR-active vibrational modes in polymers,[266] biomolecules,[267] saccharides[268] and low-energy phonons in II-VI semiconductors, such as crystalline ZnTe and CdTe,[269] and nanostructures of ZnS and ZnO[270] by measuring the real and imaginary parts of the dielectric functions. The set-up of TDS is similar to that of TR-TDS with the key difference being the absent of the pump source beam line, as shown in Figure 2.4. The low-frequency phonons play a significant role in carrier scattering and electrical conductivity, thus it is important to understand the phonon modes of ternary alloyed nanostructures for their potential applications in optoelectronics.

Generally, in the THz regime, the dielectric function $\varepsilon_m(\omega)$ consists of the contributions from high-frequency dielectric constant, conduction free electrons, and lattice vibrations, which is described by[166]

$$\varepsilon_m(\omega) = \varepsilon_\infty - \frac{\omega_p^2}{\omega^2 + i\gamma\omega} + \sum_j \frac{\varepsilon_{st_j} {\omega_{TO_j}}^2}{{\omega_{TO_j}}^2 - \omega^2 - i\Gamma_j\omega} \tag{4.5}$$

where ε_∞ is the high-frequency dielectric constant, the second term describes the

contribution from free electrons or plasmons and the last term presents the behavior of optical phonons, in which the summation involve all lattice oscillations with the *j*th transverse optical phonon frequency ω_{TO_j}, phonon damping constant Γ_j, and oscillator strength ε_{st_j}.

The low-frequency phonon resonance in ternary CdS_xS_{1-x} nanobelts probed by THz-TDS is reported here. We investigated the optical phonon at equilibrium and non-equilibrium conditions, respectively. The experimental spectra can be described well by the theoretical models of Eq. (4.5), as shown in Figure 4.12. The composition dependence of the CdSe-like TO mode frequencies in CdS_xSe_{1-x} nanobelts is displayed in Figure 4.12c. The solid line is the calculated values of the TO mode frequency by modified random-element-isodisplacement model.[263] Evidently, the experimental TO mode frequencies are in good agreement with the calculated values. The amplitude of oscillator strength enhanced evidently and the oscillator strength should show a linear variation with composition *x*.[263, 271] The best fitting curve, as shown as the red solid line can be described by $y = 2.10 - 2.06x$. Under nonequilibrium condition, the contributions from phonons to dielectric functions improved by the photoexcitation.

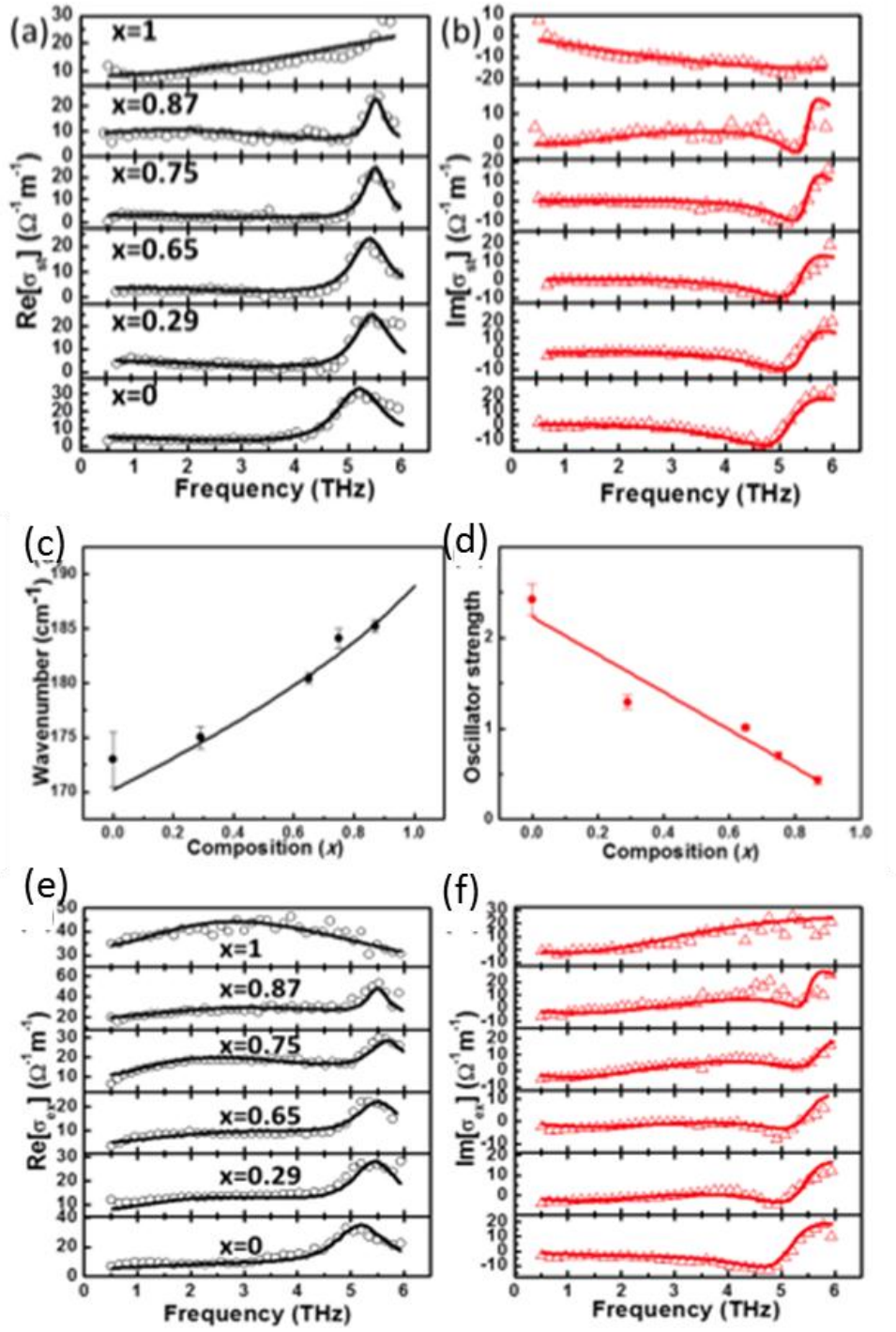

Figure 4.12 Low-frequency phonon resonance in ternary CdS_xS_{1-x} nanobelts probed by THz-TDS under equilibrium and non-equilibrium conditions.

4.4 Conclusions

In summary, we present a systematic investigation in fundamentals of Optical Properties in Ternary II-VI 1D Nanostructures, especially in CdS_xSe_{1-x} nanobelts. We investigated the temperature-dependent steady and time-resolved transient PL of CdS_xSe_{1-x} nanobelts. The observed PL spectra originated from band-edge recombination as well as surface state emission. The ultrafast carrier relaxation dynamics in CdS and CdS_xSe_{1-x} nanobelts are also studied by OPTP spectroscopy. The photocarrier decay in CdS and CdS_xSe_{1-x} nanobelts are mainly due to the fast trapping by the surface defects and structural defect-related recombination. The composition-dependent complex photoconductivity in CdS_xSe_{1-x} nanobelts are measured using TRTS technique. The ternary CdS_xSe_{1-x} nanobelts present much higher photoconductivity than that of binary nanobelts, which is attributed to the higher photocarrier densities caused by the reduction of surface trapping decay in ternary compound. These results demonstrate the high light responsivity of ternary CdS_xSe_{1-x} nanobelts to light illumination and show their promising potential as photoelectric devices such as phototransistor and solar cells.

Chapter 5

Applications of Ternary II-VI 1D Nanomaterials as FETs and Photodetectors

5.1 Introduction

1D nanostructures provide many opportunities for the nano-scaled devices and arrays assembled by the bottom-up growth paradigm.[272, 273] These nanostructures demonstrate emerging and high performance functions crucial to a lot of areas of technology. Realizing the potential applications of these nanostructures requires in depth understanding and rational control of the key parameters in the nanomaterials, including their dimensionalities, morphology, chemical composition and doping. These key parameters determine the electrical and photoelectrical properties which are critical to the nano-scaled device functions. In the last decade, with the fast development of synthesis techniques, these key parameters have been best controlled by special methods. Thus, fabrication of nanoscaled devices with the desired nano-forms of potentially important materials is the ultimate goal of nanotechnology. Ternary alloyed II-VI 1D nanostructures offer a wealth of potential applications, especially in electronic, photonics, and optoelectronics due to their excellent photoelectrical properties. This chapter will highlight a few of the interesting instances of the applications of 1D II-VI ternary alloys.

5.2 Experimental Method

After the 1D nanostructures synthesized by the method as described in Chapter 3, a single nanowire/nanobelt was transferred to a silicon substrate coated

with a 200 nm thick Si_3N_4 dielectric layer for device fabrication and subsequent electronic characterization. A UV laser lithography system (Heidelberg Instruments μPG101) was adopted to construct the device architecture. The device fabrication was completed by thermal evaporation of 20 nm cobalt and 280 nm gold as the source-drain electrodes. This is a brief technical process we employed for single nanowire/nanobelt device fabrication. Despite of the abundant research activities on single nanowire/nanobelt devices, we have devoted efforts on extending the device working scale and developing a new paradigm referred to as large-area devices where integrated 1D nanostructures are assembled over substrates. We employed the direct contact transfer technique as described in Chapter 2 to fabricate the integrated nanostructure device covering reasonably large area. Briefly, the as-grown 1D nanostructures on Si donor substrate was faced down against a plain acceptor substrate (Si_3N_4/Si). The donor substrate was gradually slid to a desired direction with downward pressure. During this process, 1D nanostructures would be transferred onto the accepter substrate parallel aligned along the sliding force direction forming laterally aligned nano-networks. The nano-network device fabrication was done by thermal deposition of 200 nm thick metal electrodes assisted by the micro shadow mask with channel length varying from 70 to 200 μm. After the device fabrication, the device performance characterization was carried out by the TTP-6 probe station technique combined with a Keithley 4200 or 6430 source meter under ambient and vacuum condition.

5.3 Results and Discussions

5.3.1 Field-Effect Transistors (FETs)

FETs are the basic build-blocks in many electrical devices such as integrated circuit, digital data storage, and flat panel displays due to their high yield and capability to scale down in dimensions. Metal oxide semiconductor FETS (MOSFETs) are the most widely used class among the different structures of FETs and play a central role in the current electrical technology. The typical architecture of normal MOSFETs is composed of five major units: conduction channel, gate dielectric layer, source electrode, drain electrode, and gate electrode.[22] MOSFETs firstly arise from the silicon electronic techniques, and now have been widely applied to various semiconductor materials. The unique geometry of 1D nanomaterials makes them a natural choice as the conduction channels in nano-scaled MOSFETs. The architecture of the nanowire-MOSFETs is schematically illustrated in Figure 5.1a.

5.3.1.1 Single Nanowire FETs

The FETs device constructed from single nanowires/nanobelts has been demonstrated with high performance due to the features of high-quality single crystal, reduced phonon scattering in low-dimensionality, device material decoupled from substrate material, quantum confinement, and large surface-to-volume ratio. The insert of Figure 5.1b shows the structure of a nanoscaled MOSFET fabricated from single $CdS_{0.25}Se_{0.75}$ nanobelts[136]. The device was constructed on a SiO_2/p^+-Si substrate with a global back-gate configuration. In a

typical fabrication process, the CdS_xSe_{1-x} nanobelts were dispersed on the substrate at a desired density, and then electrodes were deposited onto the nanobelts by e-beam evaporation accompanied by the photolithography and lift-off processes. The device was demonstrated with a pronounced gating effect revealed by the gate-dependent I_{ds}-V_{ds} curves as shown in Figure 5.1b. The relationship of the conductance increasing correspondingly with increased V_g revealed the n-type conductivity of CdS_xSe_{1-x} nanobelts. From the I_{ds}-V_g curve shown in the Figure 5.1c, a threshold voltage of 4.9 V and an on/off ratio of 10^5 were obtained from this device. The electron mobility and carrier concentration were calculated to be 14.8 $cm^2/(Vs)$ and 3.9×10^{16} cm^{-3} from the equations of $\mu = g_m C_o^{-1} V_{ds}^{-1} Z / L$ and $n_c = C_o V_T / eT$, respectively, where $C_o = \varepsilon\varepsilon_o / h$ is the gate capacitance, *T* is the thickness of the nanobelt, *Z/L* is the ratio of channel width to length, and g_m is the transconductance of the FET.[274] All the parameters show better values than those of reported binary CdS and CdSe nanobelts.[275, 276]

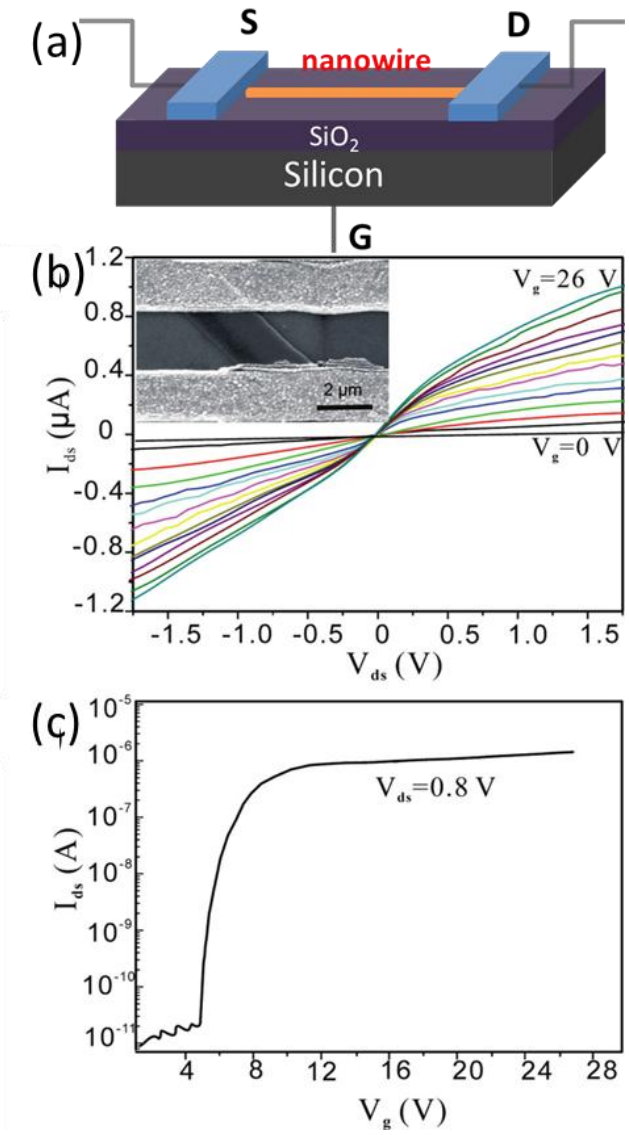

Figure 5.1 (a) Schematic illustration of a single nanowire FET. (b) and (c) FET performance characteristics of CdS_xSe_{1-x} single nanobelt FET (reprinted from Ref. [136] by permission of the American Chemical Society).

5.3.1.2 Nano-Networks FETs

In parallel to the rapid development of nanoelectronics, significant progress has been made in recent years to enlarge the system scale and create a new

paradigm referred to as macroelectronics or large-area electronics where integrated microelectronics devices are fabricated over substrates ranging from several millimeters to meters in dimensions. Fabrication of large-area electronic devices from oxide nanowires is a challenging proposition. Direct printing of nanowires such as dry transfer printing,[277] microcontact printing,[278] and direct transfer printing[279] have recently been reported. These techniques that normally involve the use of ultrasonication to harvest the nanowires followed by stamp transfer typically result in networks with low density of nanowires. Direct-contact printing is a very promising methodology that relies on aligned nanowires grown on substrates followed by a lubricant-mediated mechanical rubbing transfer of nanowires to enable wafer assembly as well as 3D multilayered device structures.[280, 281] Our group employed the contact printing method to fabricate aligned 1D CdS_xSe_{1-x} nanobelt networks as wafer-scale FETs.[187] Figure 5.2a schematically illustrates the process of nano-network FET fabrication. The SEM image of the horizontal aligned nanonet-FET fabricated from $CdS_{0.8}Se_{0.2}$ nanobelts with the schematic in the insert is shown in Figure 5.2b. The interface between the metal electrode and the nanobelt network is displayed using the red dotted-line. The typical output characteristic curves are shown in Figure 5.2c, with gate voltage increasing from 5 to 30 V in steps of 5 V. Consistent with single CdS_xSe_{1-x} nanobelt FETs,[136] the nanonet-FET shows an obvious gating effect and presented typical n-channel depletion mode behavior with good saturation. Lower threshold voltage than those of pure CdS[275] and CdSe[276] nanobelt FETs were measured and listed in Table 5.1, whilst the on/off ratio was tested to be much

higher than those reported for CdS and CdSe nanobelts. Light irradiation on II-VI ternary alloys will lead to the generation of electron-hole pairs in the nanostructures, resulting in the increase of conductivity. Consequently, the device charateristics of the II-VI ternary nanonet-FETs are significantly influenced by the incident light. As shown by the I_{ds}-V_{gs} curves (V_{ds} = 20 V) under different light intensities (1, 3, 5 W/m^2, Figure 5.2d), the threshold voltage (V_{th}) obviously left-shifted with the increasing light illumination intensities (Table 5.1 and Figure 5.2d). Despite of the saturation current increasing with the light intensities, the on/off ratio reduced from 5.8×10^5 to 2.9×10^4 due to the more prominently increase in off current.

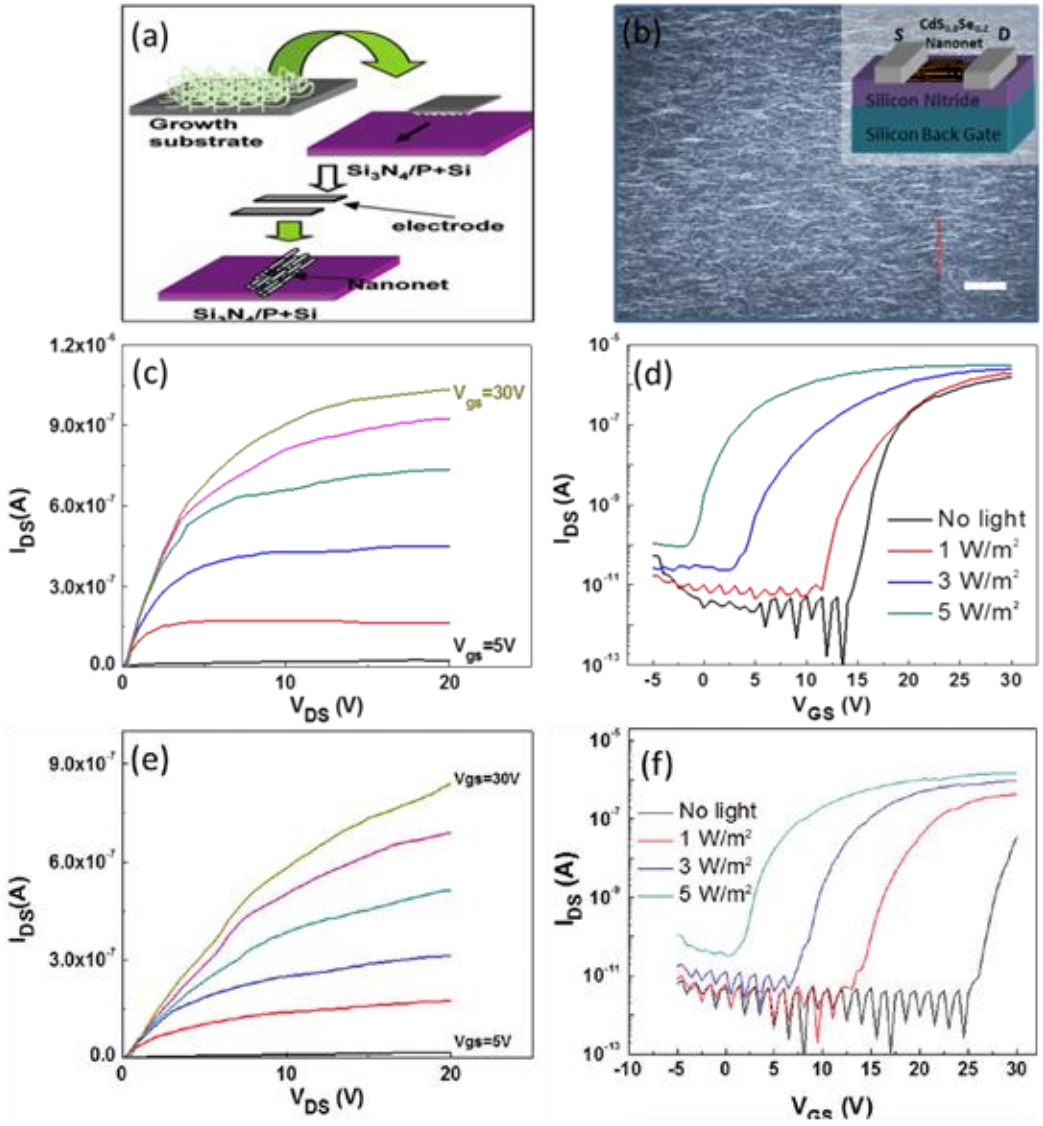

Figure 5.2 (a) Schematic illustration of the nano-network FET fabrication process. (b) SEM image and schematic (insert) of the parallel aligned CdS_xSe_{1-x} nanonet-FET. I_{ds}-V_{ds} output curves of (c) $CdS_{0.8}Se_{0.2}$ and (e) $CdS_{0.65}Se_{0.35}$ at V_{gs} from 5 V to 30 V. Transfer characteristics of (d) $CdS_{0.8}Se_{0.2}$ and (f) $CdS_{0.65}Se_{0.35}$ under different light intensity.

Different from the electron mobility calculation in a single nanowire FET, a parallel plate capacitor model must be assumed in the networks to estimate the

gate capacitance. 15% area coverage of the nanobelts can be estimated from the SEM images. Following the route reported by Dattoli *et al*,[282] the normalized effective gate capacitance of about 60% can be calculated and will be utilized for the mobility calculation following the expression,

$$\mu_{sat} = \frac{2I_{DS}L}{0.6C_iW(V_G - V_{th})^2} \tag{5.1}$$

where L and W are the length and width of the channel, respectively. C_i represents the gate capacitance per unit area. The calculated mobility values at different light illumination intensities are listed in Table 5.1, according to the measured Si_3N_4 capacitance (18.83 nF/cm^2, 1 MHz), channel length (100 μm), and channel width (3000 μm). As implied by the results, the increasing light intensity will promote the electrical performance of the nanonet FET due to the increasing density of free electrons. Nevertheless, the performance of the device did not enhance all the way with the increasing light intensity but became less promising with the saturation current only increased by a factor of 2 whilst the off current increased by two orders of magnitude. In addition, the carrier mobility was weakened as well. The high intensity of photo-generated electrons under intensified light illumination reduced the significance of the gate voltage effect which facilitated a less steep I_{ds}-V_{gs} curve, reducing the carrier mobility. The FET performance of nanobelts with different composition was investigated. All the ternary alloys exhibited similar output performance. The nanonet FET performance of another representative ternary sample with x value of ~ 0.65 is displayed in Figure 5.2e and f. There was no obvious trend on the dependence between the FET

performance and the ternary compound composition. However, compared with the pure binary CdS (parts a and b of Figure 5.3) and CdSe (parts c and d of Figure 5.3) nanonet-FETs, the ternary nanobelts exhibited more significant gating effect, full saturation, higher on/off ratio and larger carrier mobility. All these results indicate the CdS_xSe_{1-x} nanobelts have a great potential in nano-scaled electronic application.

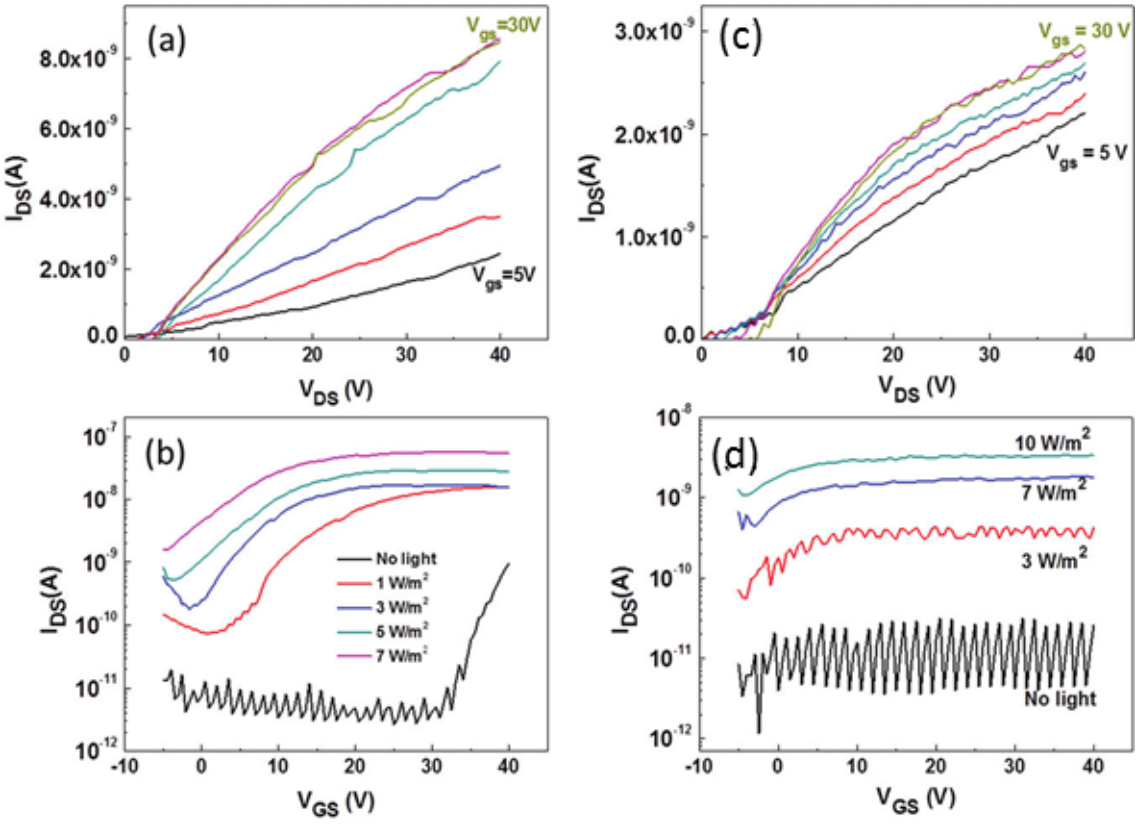

Figure 5.3 I_{ds}-V_{ds} output curves of (a) CdS and (c) CdSe nanobelt networks FET at V_{gs} from 5 V to 30 V. Transfer characteristics of (b) CdS and (d) CdSe under different light intensity illumination.

Table 5.1 Summary of Device Behavior at Different Light Intensity Illumination

Light illumination	Mobility ($cm^2/(Vs)$)	V_{th} (V)	ON (A)	OFF (A)	ON/OFF
No illumination	0.04	15.6	1.56×10^{-6}	2.7×10^{-12}	5.8×10^{5}
1 W/m^2	0.049	15	1.96×10^{-6}	10.5×10^{-12}	1.9×10^{5}
3 W/m^2	0.034	7.8	2.42×10^{-6}	27.0×10^{-12}	9.0×10^{4}
5 W/m^2	0.0315	-1.3	2.93×10^{-6}	100.0×10^{-12}	2.9×10^{4}

Similarly, the large scale devices based on ZnS_xSe_{1-x} nanowires network were obtained through the contact printing method.[186] The corresponding SEM image of the parallel aligned nanowire network FET based on $ZnS_{0.42}Se_{0.58}$ nanowires is shown in Figure 5.4a with the schematic of the nanonet-FET architecture shown in the insert. Evidently, the network displays highly ordered alignment. The I-V characteristics of $ZnS_{0.42}Se_{0.58}$, ZnS, and ZnSe networks at sweeping voltages from -40 V to 40 V are shown in Figure 5.4b. As implied, the ternary $ZnS_{0.42}Se_{0.58}$ (red line) networks presented the significantly higher current magnitude than those of the pure binary ZnS (violet line) and ZnSe (green line) networks. The current enhancement is attributed to the promotion of the electrical-conductivity resulted from the formation of alloy.[283, 284]. Briefly, the increasing localized state density present in the mobility gap facilitates the conductivity enhancement.[283] The enhanced conductivity enables the application of ZnS_xSe_{1-x} nanowire networks in the field of electronics. Based on the

simplified network-FET, typical I_{ds}-V_{ds} output curves were tested with V_{gs} increasing from 0 V to 40 V in steps of 10 V and result is shown in Figure 5.4c. As revealed, a significant back gating effect is exhibited and the positive gate voltage resulted in the source–drain current increasing strongly, which indicates the nanowires were n-type channel. Samples with different compositions were investigated while all the ternary alloys exhibit parallel performance and we did not find a certain tendency with the variation of the stoichiometry. However, compared with the poor electrical properties of pure binary ZnS and ZnSe compounds, the more obvious gating effect was displayed among these ternary alloys.

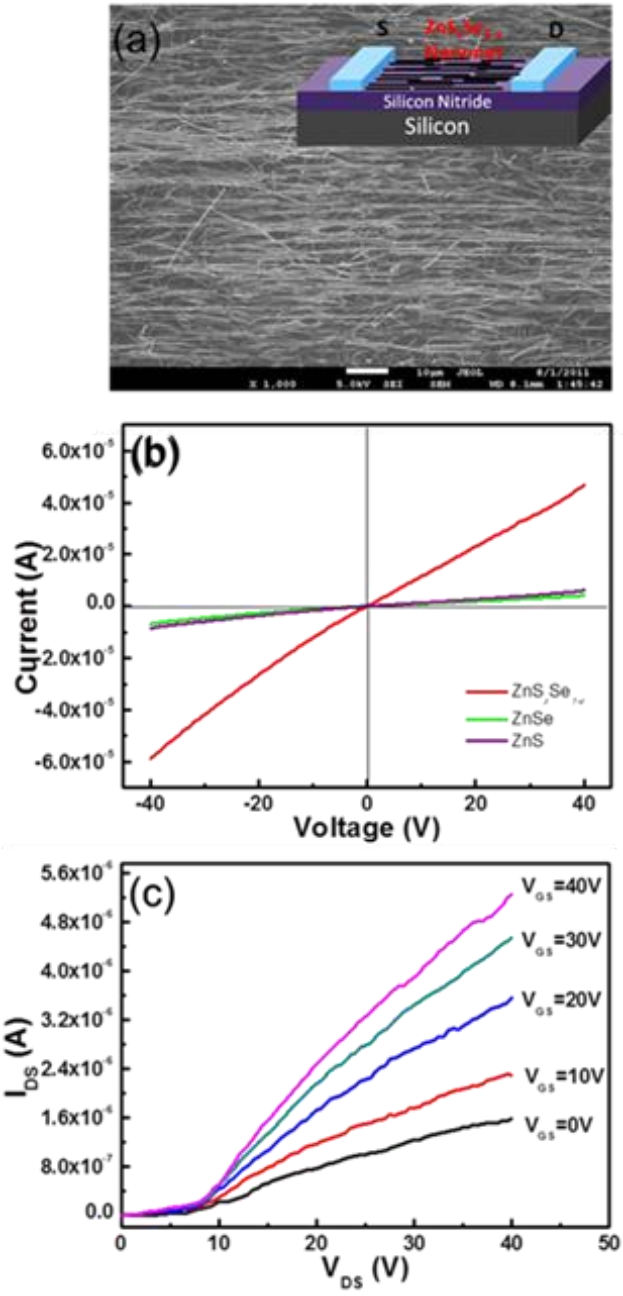

Figure 5.4 (a) SEM image and schematic illustration (insert) of the horizontal aligned ZnS_xSe_{1-x} nanowire network-FET. (b) Typical I-V measurement of the ZnS, ZnSe, and $ZnS_{0.42}Se_{0.58}$ nanowire networks. (c) I_{ds}-V_{ds} output curves of $ZnS_{0.42}Se_{0.58}$ network-FET at V_{gs} from 0 V to 40 V.

5.3.2 Photodetectors/sensors

Among all the nano-scale devices, photodetectors are critical for applications of binary switches in photo-communications and imaging techniques, as well as in future memory storages and optoelectronic circuits.[151-157] II-VI ternary semiconductors present direct band gaps from UV to NIR, and the band gaps of 1D ternary nanostructures can be absolutely controlled and designed by carefully controlling the chemical stoichiometry. Therefore, 1D II-VI ternary nanostructures are very promising candidates for applications as photodetectors or photosensors available to work from NIR to UV spectrum. Distinctively, owing to the continuously controlled band gaps of ternary nanostructures, such nano-photodetectors are expected to display much improved performance as compared with the conventional binary II-VI film and bulk devices. Several physical processes should be considered to understand the photoconductive properties of nanostructural semiconductors; (1) Exciton generation by light irradiation with energy exceeding the band gap, which determines the spectral response of photodetectors. (2) Electron and hole separation by applied electrical field. This process facilitates photocurrent, and a strong electrical field can be desired to improve exciton dissociation and consequently increase the response speed. (3) Exciton recombination at the bulk and surface of nanostructures (resulting in the decrease of photocurrent). The lifetime of the photo-excited carriers determines the gain and response speed. Nevertheless, large gain would slow down the response speed. A compromise between the gain and response speed has to be considered to realize a reasonable overall performance. (4) Carrier trapping.

Carrier trapping and releasing dominate the rise time and decay time. Namely, high crystalline quality (few defects) will benefit a high response speed. (5) Surface band bending. For wide band gap semiconductors, surface band bending usually occurs due to the surface depletion, which leads to an energy barrier for electron-hole recombination. The barrier height is highly related to the nanostructure size. (6) Ambient effect. Adsorption of ambient gas, particularly oxygen and moisture, might withdraw electrons from n-type nanomaterials and thus cause the decrease of photocurrent. On the other hand, desorption of gas molecules will facilitate the increase of photocurrent.

Here, we present a study on the photocurrent of ternary CdS_xSe_{1-x} nanobelts based on the network device and demonstrated the potential of the device as high performance photosensor. The photoresponse of the nanonet was detected by an oscilloscope (DSO-X 3024A, 200 MHz) associated with an electronic chopper (SRS SR540). The experimental setup is schematically illustrated in Figure 5.5a. In this setup, the light chopper was employed to turn the light source on and off while the oscilloscope was utilized to monitor the time dependence of the output current. A halogen lamp with the main spectrum ranging from 400 nm to 800 nm was employed as white light source to study the photoresponse behavior of the nano-network devices. The spectrum of the lamp was captured by a spectrometer and the result is shown in Figure 5.5b.

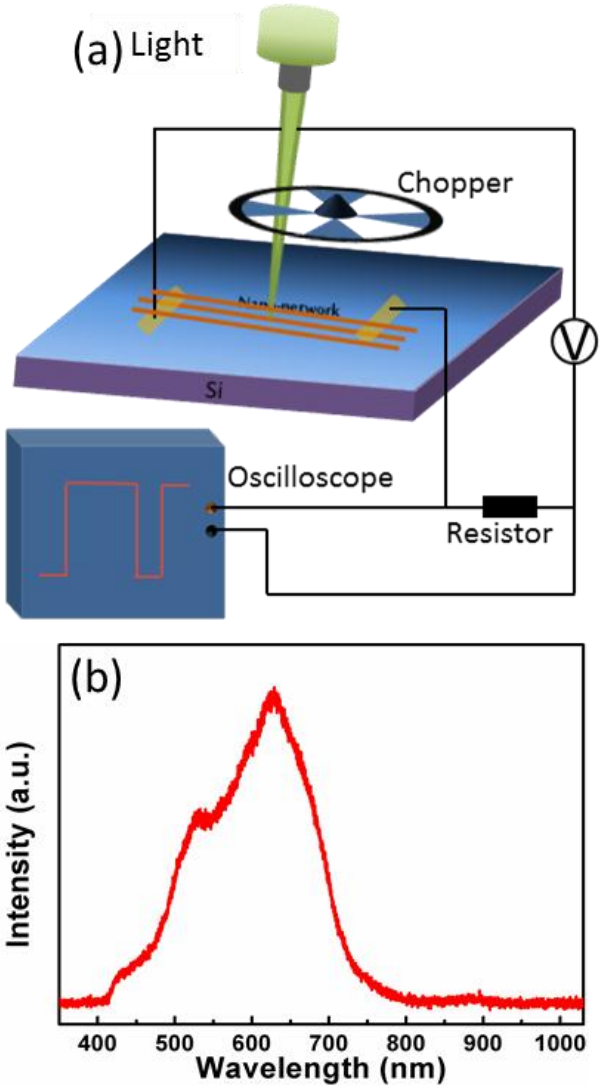

Figure 5.5 (a) Schematic diagram of time response measurement setup. (b) Spectrum of the light source.

The photo-switching response of the $CdS_{0.8}Se_{0.2}$ nanobelt network to the normal white light source as a function of time is shown in Figure 5.6a. The measurements were carried out at the bias voltage of 20 V, and the applied light intensity was fixed at 50 W/m^2. Evidently, the output current increased to 2.8 μA in a very short time (<2 s) after the sensor was exposed to the light irradiation

while the current was only at the level of nanoamperes under dark conditions. The photoresponse performance of devices based on CdS_xSe_{1-x} nanobetls with different stoichiometry was also investigated. All the ternary ternary alloys exhibited similar performance on the current enhancement and response time. An example of the photoresponse of another ternary sample with *x* values of about 0.65 is displayed in Figure 5.6b. There is no obvious trend found on the dependence between the photosensor performance and the composition of the ternary alloys. However, compared to the sensors based on pure binary CdS (Figure 5.6c) and CdSe (Figure 5.6d) nanobelt networks, the ternary alloys produced much higher photocurrent upon the same illumination of light. All the results promote the potential of ternary CdS_xSe_{1-x} nanobelts in nano/micro-scaled optoelectronic applications.

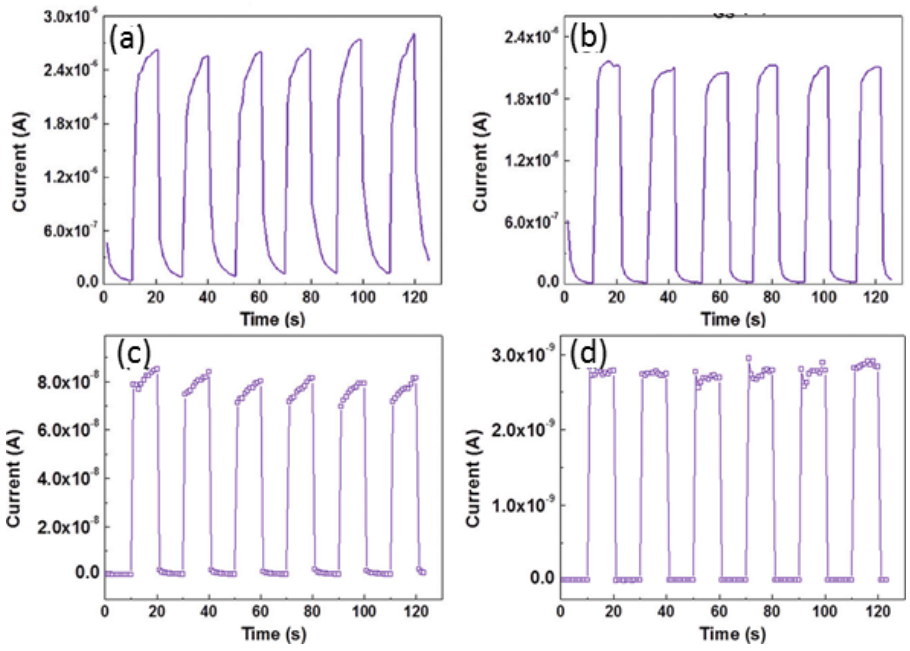

Figure 5.6 Photosensitive behaviors of (a) $CdS_{0.8}Se_{0.2}$, (b) $CdS_{0.65}Se_{0.35}$, (c) CdS, and (d) CdSe nanonets.

In addition to of the demonstration of ternary CdS_xSe_{1-x} nanobelts as photosensors, the photoresponse of ZnS_xSe_{1-x} nanowires was also investigated. Figure 5.7 shows the photoresponse of $ZnS_{0.42}Se_{0.58}$ nanowire networks as a function of time at the normal white light source illumination. The bias voltage was fixed at 30 V and the applied light illumination was 30 W/m^2. The presence of the light illumination shall be denoted as ‘‘on’’ state, in reverse, the blockage of the light illumination shall be denoted as ‘‘off’’ state, and both the ‘‘on’’ and ‘‘off’’ states were kept to the same period of 20 seconds. Evidently, the photocurrent increased to 13 mA in a reasonably short time after the nanowire network was exposed to the light source but the recombination time is relatively slow and would not revert to the original value during the ‘‘off’’ period. These phenomena were found with the nanowire network in vacuum or in ambience. The light-induced thermal effect would contribute to the measured photocurrent and tend to introduce a slower photoresponse in the nanowires.[239]

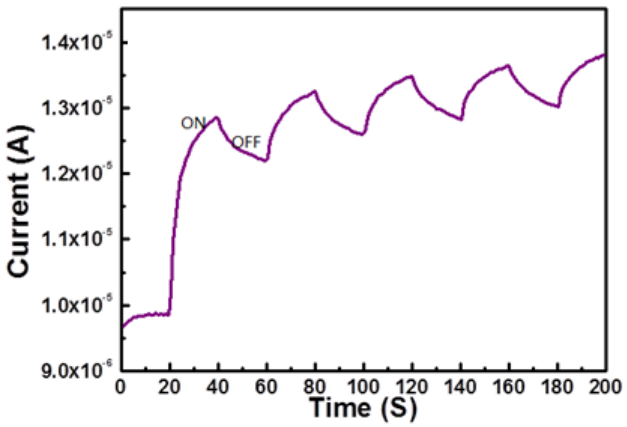

Figure 5.7 Photosensitive behavior of $ZnS_{0.42}Se_{0.58}$ nanowire network.

5.4 Conclusions

In summary, two interesting instances, FETs and photodetectors/sensors of the applications of 1D II-VI ternary alloys, especially, CdS_xSe_{1-x} nanobelts and ZnS_xSe_{1-x} nanowires, are demonstrated here. The nanostructures are manipulated to reasonable large-scale nano-network devices *via* a contact printing method. The CdS_xSe_{1-x} nanobelt network device shows obvious gating effect and pronounced photosensitivity. The measured threshold voltage is lower than those of pure binary CdS and CdSe nanoribbons, and the on/off ratio is much higher than that reported for CdS and CdSe. The CdS_xSe_{1-x} nanobelt network based photosensor presents fast response to normal and weak white light. The ternary ZnS_xSe_{1-x} nanowires were also fabricated into large-scale network devices by the similar approach. The electrical properties are significantly enhanced due to the alloyed effect as compared to the binary ZnS and ZnSe nanowires while the sensitive photo-responsibility is also reported. All the above promise their potential applications in adjustable electrical and optoelectrical devices in the UV to visible region.

Chapter 6

Direct Laser Pruning of CdS_xSe_{1-x} Nanobelts en Route to a Multicolored Pattern with Controlled Functionalities

6.1 Introduction

Once 1D ternary nanostructures with uniform composition are fabricated, in light of interest to miniaturize functional device, it is worthwhile to develop techniques which can further create micropatterns with controlled functionalities on these samples. These techniques should be able to directly pattern the nanomaterials as well as altering the optical properties of the ternary alloys during the process. Therefore, a simple, flexible, efficient and low cost multipurpose post processing technique is extremely desirable. So far, several innovative patterning methods have already been reported. These include nanoimprinting,[285, 286] microcontact printing,[287] soft lithography,[288] dip-pen lithography,[289] photolithography,[290] and inkjet printing.[291] Each of these techniques has specific advantages and drawbacks. For example, most of the methods involved employment of masks to define the patterns or post-processing treatment for the removal of photoresist. These processes often destroy or compromise the optical properties of the delicate nanomaterials. In this chapter, we present a facile and effective focused laser pruning method that can controllably modify the chemical composition of the ternary nanostructures. In doing so, we can control the photoluminescence properties of the nanobelts. This is a surprising result considering the more conventional destructive nature of the focused laser beam.

With a scanning focused laser beam, multicolored micropatterns can be fabricated on an extended area on a substrate covered with the nanobelts. Moreover, the fabrication of the micropatterns does not require the use of any pre-defined mask. Hence this method reduces the risks of physical damage and chemical contamination to the sample. The possible chemical modifications were systematically investigated by photoluminescence spectroscopy, energy-dispersive spectroscopy, X-ray photoelectron spectroscopy and X-ray diffractometry.

6.2 Experimental Method

CdS and CdSe mixed powders were used as the source precursor to synthesize CdS_xSe_{1-x} nanobelts. A silicon wafer coated with a thin Au layer was slotted vertically inside a specially designed substrate holder. Such an arrangement promoted the growth of nanobelts with uniform stoichiometry since it is free from the influence of temperature gradient during the growth. The furnace was maintained at 650 ºC for 30 minutes while the pressure was regulated at 1 Torr. Further characterizations of the pruned samples were carried out through a fluorescence microscope (FM, Olympus IX71S1F-3 Inverted Microscope), field emission scanning electron microscope (FESEM, JEOL JSM-7600F) with built-in energy-dispersive spectroscopy (EDS), photoluminescence microscope (Renishaw inVia with a Kimmon 1K Series He-Cd Laser), X-ray photoelectron spectroscopy (XPS) and X-ray diffractometer (X'PERT MPD, Cu-Kα (1.5406 Å) radiation).

6.3 Results and Discussions

After the successful synthesis of the ternary alloyed CdS_xSe_{1-x} nanobelts with high uniform composition, we subjected the alloy to a treatment of focused laser beam destruction with the aim to create micropatterns on the substrate. However, instead of destroying the nanobelts, we found that the focused laser beam could effectively modify the chemical nature of the nanobelts and more importantly change the photoluminescence nature of the nanobelts. With this feasibility, we could carry out localized bandgap engineering on a sample and create different components on the same sample.

The direct micro-patterning and micro-modification was carried out through an optical microscope-focused laser beam set-up, as illustrated in Figure 6.1a. In our experimental set-up, a diode laser (maximum power = 60 mW, λ = 660 nm) was employed. The emitted laser beam was introduced into an optical microscope *via* two mirrors. The power of the laser beam was adjusted by a neutral density filter inserted along the beam path. Inside the microscope, the laser beam was directed towards the objective lens (L, magnification = 50 ×) through a beam splitter (S). The laser beam was tightly focused onto the samples surface via the objective lens. The samples were mounted on an X-Y stage (motorized stage MICOS) which is controlled by a computer. A CCD camera was used to capture the optical images, which could monitor the process of laser pruning live and examine the quality of the pattern directly. Apart from micropatterning with the samples in ambient condition, a vacuum chamber (2 cm × 1 cm × 0.5 cm) could be used to house the samples. Laser could be focused towards the sample through

a quartz window positioned on the top of the chamber. A vacuum pump was linked to the chamber and thus the samples can be modified in vacuum condition. In addition, we could also fill the chamber with Helium gas to control the gaseous environment during the laser irradiation.

When the focused laser beam was incident upon the nanobelts film, the irradiated nanobelts absorbed the laser energy, then the energy was rapidly converted to local heat. The intense heat raised the temperature of irradiated nanobelts and caused localized partial modification of the ternary alloys. This method is akin to plant pruning and thus denoted as laser pruning method. By controlling the sample stage movement in a programmable manner with respect to the focused laser beam, micro-patterns of the desired design were constructed on the nanobelts covered surface. Figure 6.1b shows a SEM image of a pattern created using this laser pruning method and Figure 6.1c shows the same pattern as observed using the fluorescence microscopy. The bright orange background is reminiscent of the optical properties of the $CdS_{0.71}Se_{0.29}$ nanobelts. Remarkably, the laser modified region was also optical active and exhibited a different fluorescent color. The "Dragon" was created *via* a laser power of 30 mW.

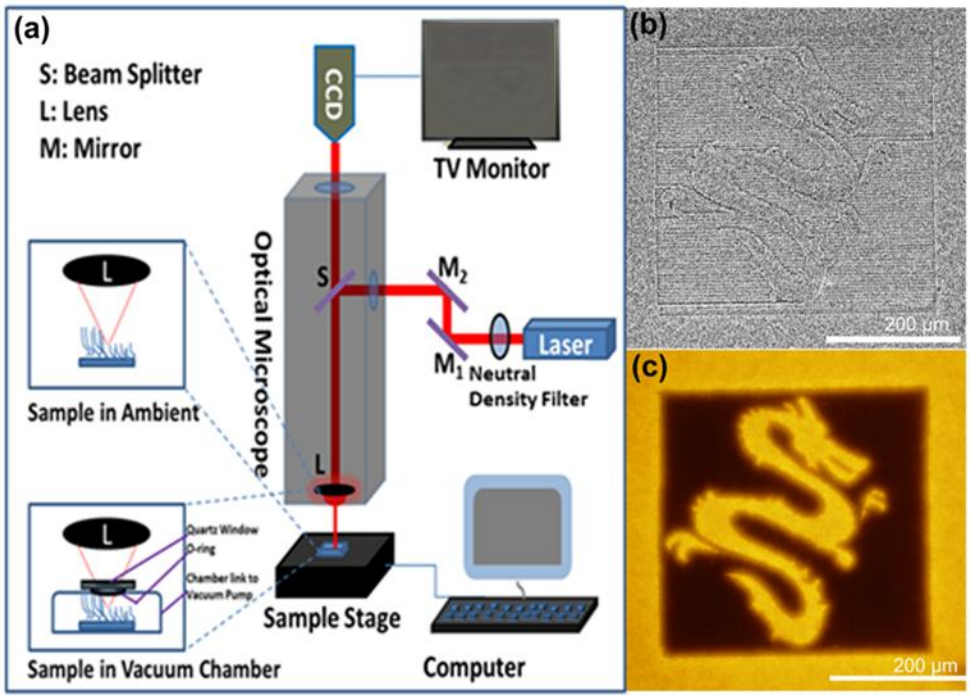

Figure 6.1 (a) Schematic of the optical microscope-focused laser beam set-up for micro-patterning. (b) SEM and (c) fluorescence microscopy images of a "Dragon" patterned *via* a 660 nm laser with a power of 30 mW.

Figure 6.2 provides further illustrations on the appearance of the patterned samples when they were imaged by SEM, optical microscope and fluorescence microscope respectively. SEM image (Figure 6.2a*i*) did not reveal a striking contrast from the complex micro-structure created. This was attributed to the relatively low laser power (20 mW) used and hence the $CdS_{0.75}Se_{0.25}$ nanobelts were not significantly affected. However, as the nanobelts surfaces became rough, then the reflectivity of the laser pruned areas appeared significantly different from the pristine areas. As a result, the optical image provides a clearer distinction for the micro-pattern (Figure 6.2a*ii*) than that revealed by SEM image. Perhaps the most dramatic change in the nanobelts was revealed by the fluorescence

microscope image (Figure 6.2a*iii*). CdS_xSe_{1-x} nanobelts have been demonstrated to possess high yield luminescent in the Chapter 4.

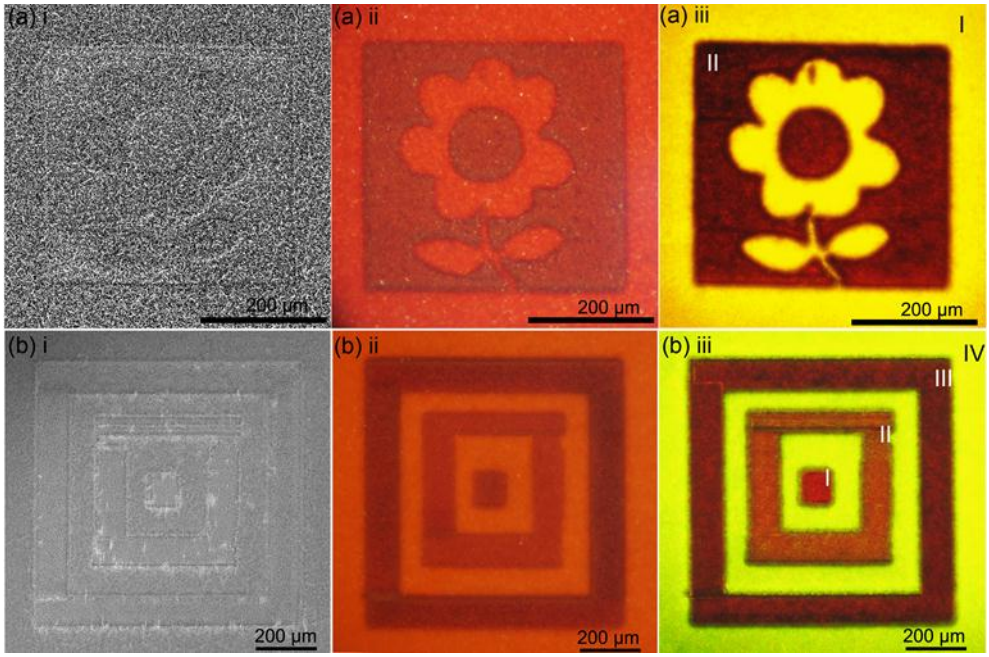

Figure 6.2 (a) (*i*) SEM, (*ii*) optical microscope and (*iii*) fluorescence microscope images of a "Flower" patterned on $CdS_{0.75}Se_{0.25}$ nanobelts film *via* a 660 nm laser with a power of 20 mW. (b) (*i*) SEM, (*ii*) optical microscope and (*iii*) fluorescence microscope images of a multiple boxes patterned on $CdS_{0.79}Se_{0.21}$ nanobelts film. Multi-colored pattern with four different colors obtained by carefully control the laser power.

Therefore, intense light emission was achievable upon UV excitation. Remarkably, laser treated nanobelts had a different fluorescent color and the difference in this color from the pristine nanobelts resulted in the best contrast among the three types of images. Evidently, the laser treated nanobelts have become different PL active materials. This is a surprising finding considering the

destructive attribute of focused laser beam. The color can be readily regulated and further altered by carefully controlling the laser power intensity. Figure 6.2b shows another example of multi-colored pattern with four different colors (as labeled in Figure 6.2b*iii*) formed on a $CdS_{0.79}Se_{0.21}$ sample created *via* laser pruning at different laser powers.

Systematic studies on the dependence of such laser modification on the power of the laser beam were carried out. Figure 6.3a shows a set of patterned micro-squares (200 μm × 200 μm, as labeled in Figure 6.3a from right to left) created on $CdS_{0.71}Se_{0.29}$ nanobelts using laser beam with different laser power. The laser power was increased from 10 mW to 30 mW in the steps of 5 mW corresponding to patterns from I to V. Evidently, from I to V, the micro-squares gradually deepened, attributable to the increasing intense heat caused by increasing laser power. However, the depths of these patterned squares created are not very distinguishable compared to the channel depth created *via* a large power of 60 mW. In particular, pattern I is barely observable from the SEM image.

In order to investigate the variation of color emission, fluorescence microscopy images of these squares were captured and shown in Figure 6.3b. Evidently, with the laser power gradually increasing, a darker red color was seen emitting from the pruned region. By altering the power from 10 mW to 30 mW, the corresponding patterns can be varied in color covering a decent range from bright red to dark red. PL spectra for each other these regions were captured as well. As shown in Figure 6.3c, the pristine region and patterns I to V exhibits distinct PL peaks at different wavelengths.

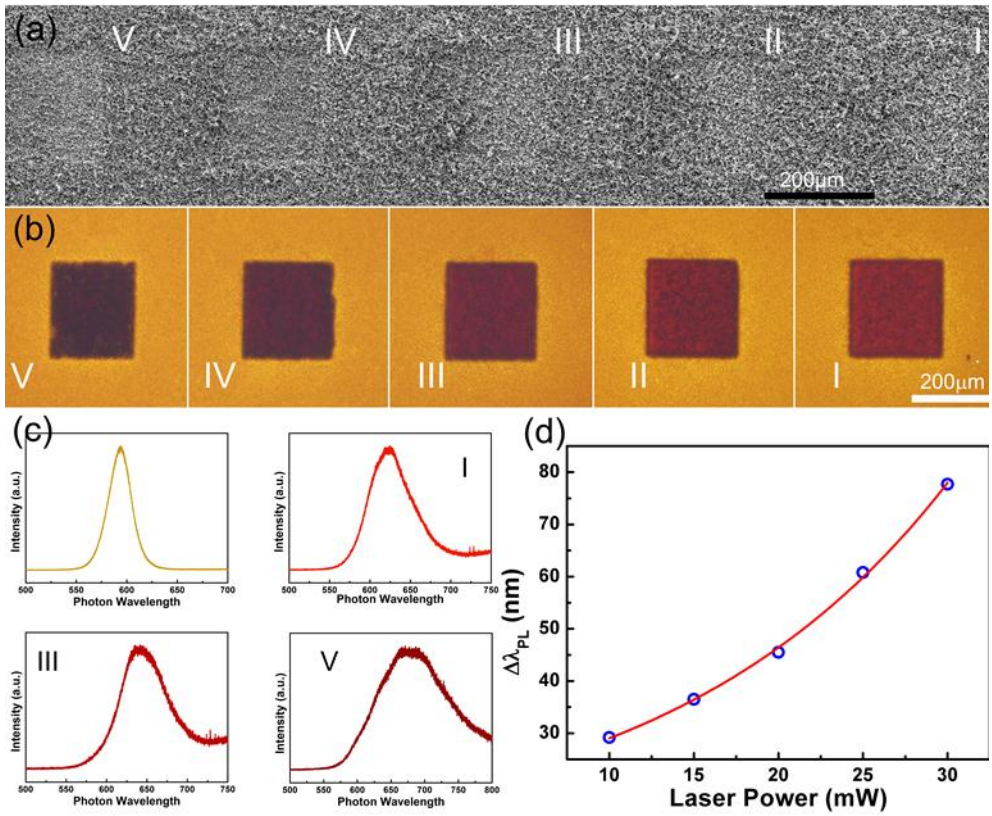

Figure 6.3 (a) SEM images of five micro-squares patterned on $CdS_{0.71}Se_{0.29}$ nanobelts *via* different laser powers. [V (30 mW), IV (25 mW), III (20 mW), II (15 mW) and I (10 mW)]. (b) Corresponding fluorescence images of five micro-squares patterned, I to V *versus* the laser power from 10 to 30 mW. (c) PL spectra of as-grown region and three representative patterned micro-squares. (d) PL peak position shifts as a function of laser power.

Analysis of the peak positions associated with variation of the emission colors shown in Figure 6.3b, a significant trend could be observed. The pristine region showed a narrow and symmetrical peak located at 593.9 ± 0.1 nm, which fell in the orange visible light wavelength range and was consistent with the FM observation. After patterning with a low power of 10 mW, the PL peaks of this

region red-shifted by a large step from 593.9 ± 0.1 nm to 623.1 ± 0.1 nm, compared with the pristine site. Visually, the emitted color changed from orange to bright red (region I). Increasing the laser power in the steps of 5 mW until 30 mW, the corresponding PL peaks of regions II, III, IV and V were identified at 630.4 ± 0.1 nm, 639.4 ± 0.1 nm, 654.7 ± 0.1 nm and 671.6 ± 0.1 nm, respectively. Gradual red-shifts in the peak position were observed as the laser power increases. The related emission light of the fabricated patterns could be fine-tuned to a darker red-color in the small steps besides a giant step from orange to red in the beginning of the pruning. In addition, the PL spectra of the pruned regions become broadened and asymmetric. The broadening of the peak is attributed to the increase in surface states or defect states resulting from laser ablation.[292, 293] With the increase in laser power, the darkened color could further enhance the contrast between pruned and pristine regions and in turn facilitate a better image contrast of the micro-patterns. The color modification is quantitatively described by Figure 6.3d, in which the PL peak position shift, $\Delta\lambda$, from the PL peak position of the pristine $CdS_{0.71}Se_{0.29}$ nanobelts is plotted as a function of laser power. Evidently, the experiment data (blue circles) can be fitted very well by a quadratic function, indicating the monotonically increasing relationship between PL red-shift and laser power, after the initial step of about 30 nm.

Despite the emission color shift, the morphology modification also presents a direct dependence on laser power. The striking morphological effects caused by laser pruning of nanobelts in ambience were readily observed through SEM images. We exposed a CdS_xSe_{1-x} sample with x value of 0.68 to the focused laser

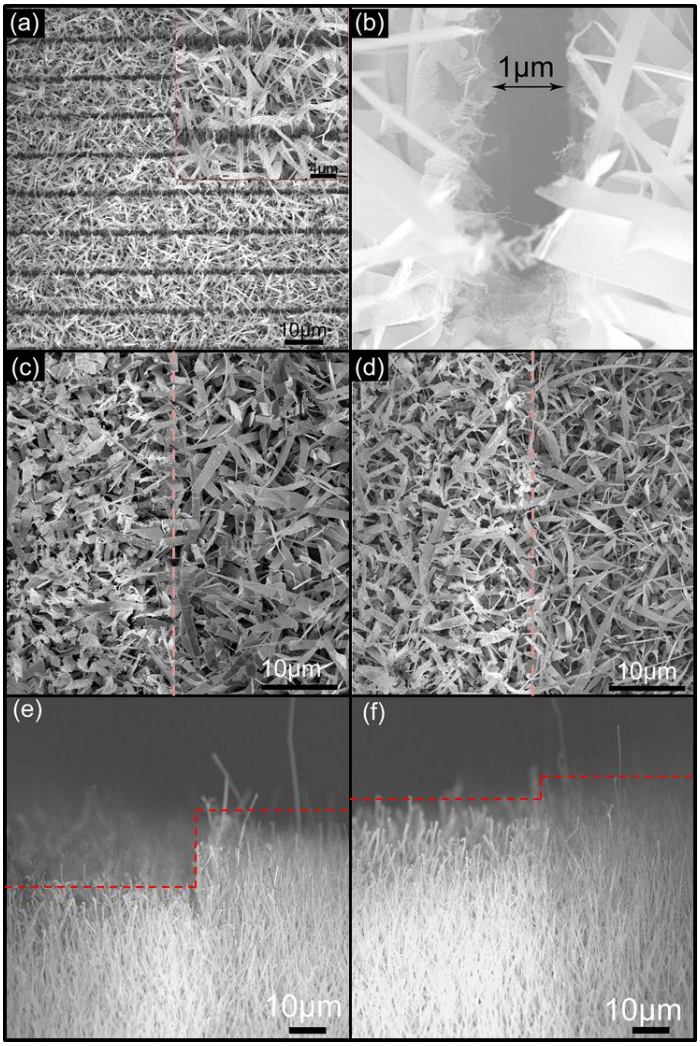

Figure 6.4 (a) SEM image of the micro-channels pattern. Magnified view in insert shows two distinct 1μm channels separated by a width of 10 μm. (b) A cross sectional SEM image of a channel reveals the high resolution of the focused laser beam technique. (c and d) Magnified images of the boundary of laser modified region (left) with pristine region (right). The powers of the laser used were 30 mW and 10 mW respectively. (e) and (f) Cross sectional SEM views of the samples shown in (c) and (d) respectively.

beam. SEM image shown in Figure 6.4a reveals that the channels cut with a strong laser power of about 60 mW. The magnified view shown in the inset clearly illustrates two distinct and well-defined channels with a width of about 1 μm separated by ~10 μm. A clear separation between the pruned and pristine nanobelts is obtained, which reveal the high spatial resolution achievable with this direct pruning technique. A cross sectional image of the patterned line channels is shown in Figure 6.4b.

The magnified views of laser treated sample clearly illustrate the physical distinctions of the morphology caused by different laser powers. After exposure to a 30 mW laser, the CdS_xSe_{1-x} nanobelt film shows a distinct boundary (red dash line) between the pruned and pristine areas, as shown in Figure 6.4c. As revealed by the side view SEM image (Figure 6.4e), the length of the film is obviously shortened (about 20 μm). And clearly the laser pruned surfaces become populated with blistered nanobelts, a clear contrast from the pristine nanobelts with smooth edges. On the other hand, for the square exposed to a 10 mW (Figure 6.4d) laser, the boundary is much more inconspicuous. The length of the nanobelts became only slightly shortened (Figure 6.4f). Similarly, the morphology of the nanobelts changed from those with smooth edges to blistered form.

The color modification and morphology changes could be initially ascribed to laser induced thermal effect from the laser power dependence. Further characterizations are shown in Figure 6.5. As is well known, the band gap energy for CdS and CdSe is 2.44 eV and 1.73 eV, respectively. These band gaps correspond to PL emission wavelength of 507 nm and 713 nm respectively.

Consequently, the significant red-shift observed from the PL spectra is attributed to the "S" element being driven away from the CdS_xSe_{1-x} nanobelts and the near-band-edge energy shift towards CdSe. Briefly, the focused laser beam ablating the nanomaterial induced a high local temperature, which might dissociate Cd=S bond and thus increase the relative concentration of CdSe species. To expound this assumption, we carried out EDS spectrum analysis on pristine region and region pruned with laser power of 20 mW. As shown in Figure 6.5a, the ratio of "S/Cd" was investigated as 0.69 for the pristine region. On the other hand, the ratio of the pruned region was significantly reduced to 0.49 as shown in Figure 6.5b. At the same time, the component of "Se" did not show any significant change caused by the laser pruning. In addition, the "O" element was detected in the pruned region, which indicates the formation of oxidation state. The broadness and asymmetry of the PL spectra after pruning (Figure 6.3c) could be attributed to defect contributions from the oxidation.

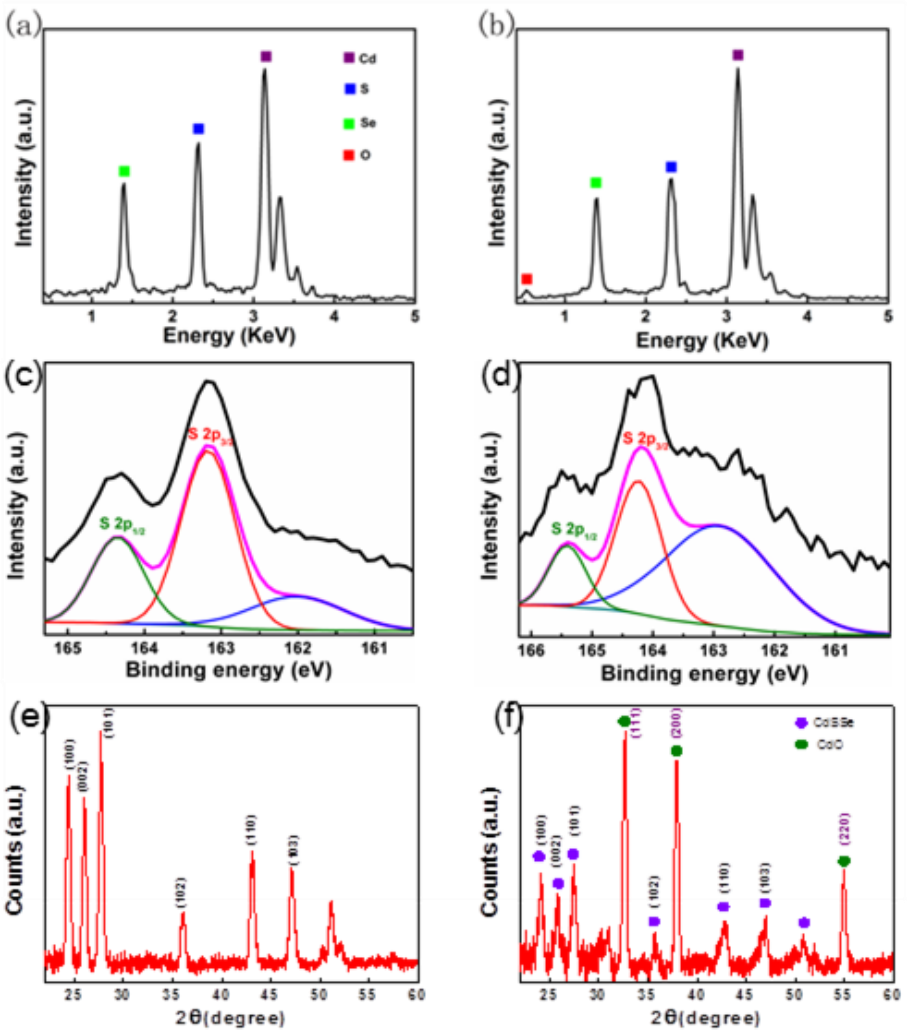

Figure 6.5 EDX spectra of $CdS_{0.69}Se_{0.31}$ nanobelts (a) before and (b) after laser modification. XPS spectra of these nanobelts (c) before and (d) after laser modification. XRD patterns of $CdS_{0.69}Se_{0.31}$ nanobelts (e) before and (f) after laser modification.

To further investigate the chemical process during the pruning process, X-ray photoelectron spectroscopy was carried out for pristine and pruned regions, respectively, as shown in Figure 6.5c and d. The S 2*p* peaks at 164.1 eV and 165.3 eV show a significant decrease after laser pruning. (the peaks were fitted

and separated by 100% Gaussian profile). To provide more convincing evidence, the XRD studies were carried out before and after laser pruning, as shown in Figure 6.5e and f respectively. Evidently, there is a small left-shift, which reveals the modification of chemical composition of the CdS_xSe_{1-x} pattern after pruning. In addition, three emerging peaks are observed at $33^\circ \pm 0.1^\circ$, $38.3^\circ \pm 0.1^\circ$ and $55^\circ \pm 0.1^\circ$, which are consistent with the (111), (200) and (220) peaks of CdO respectively, as referenced to JCPDS No. 75-0594.

The formation of the oxide indicates that oxygen plays an important role in chemical modification process induced by the focused laser beam. To further explore the role of oxygen, a specially designed vacuum chamber, as shown in Figure 6.1, was employed to prune the ternary nanobelt in vacuum or in chambered filled with Helium gas to exclude the impact of oxygen. The same laser power was employed as pruning with sample in ambience. Surprisingly, the photoluminescence spectrum reveals completely different appearance. As shown in Figure 6.6a, the red curve indicates the PL spectrum of the pruned region created in Helium environment. Evidently, the near-band-edge peak position after laser modification does not show any signification shift but a large and broad defect peak located in infrared region is displayed. The emerging broad peak is attributed to the introduction of defects caused by the destruction of the good crystalline lattice due to the laser pruning. However, in the absence of oxygen, the laser induced chemical modification of the $CdS_{0.75}Se_{0.25}$ nanobelts could not take place, hence there is no peak shift.

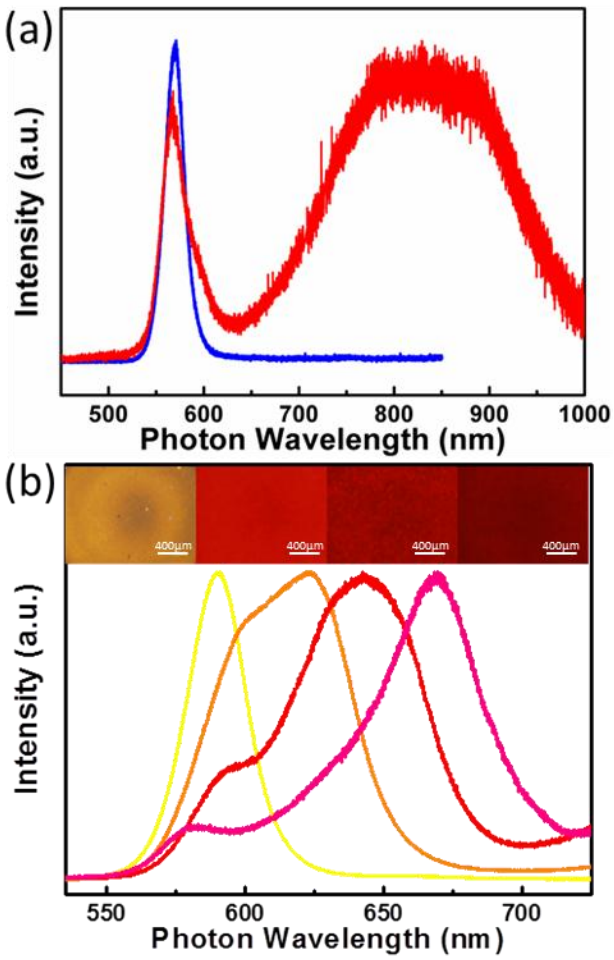

Figure 6.6 (a) PL spectra of pristine sample $CdS_{0.75}Se_{0.25}$ (blue curve) and sample after laser pruned in helium environment (red curve). (b) PL spectra of an as-grown $CdS_{0.75}Se_{0.25}$ sample (yellow curve) and three other samples after annealing with increasing temperatures of 650°C, 850°C and 1050°C for 0.5 minute. Insets show the corresponding images of the samples captured by a fluorescence microscope.

As mentioned above, the proposed mechanism is that the irradiated nanobelts absorbed the laser energy and rapidly converted to local heat, which facilitated the reaction with oxygen in ambience. Therefore, local domain

chemical modification can be achieved by focused laser beam and hence the local control of the optical property. To verify the prediction, three pieces of $CdS_{0.75}Se_{0.25}$ nanobelts film (5 mm×5 mm) were inserted into a horizontal tube furnace then annealed in ambient at 650 ºC, 850 ºC and 1050 ºC for 0.5 min. After the PL spectroscopy characterization, the peak position was found to be red-shifted, became broader and asymmetrical. The fluorescence images and corresponding PL spectrum of before and after annealed samples are shown in Figure 6b. The observed consequence is almost identical with that revealed by laser pruning. Therefore, the mechanism of laser-induced heating and the subsequent oxidation is tenable.

On top of the fabrication of a multicolored display, we found that the modified nanobelts are more stable when it comes to exposure to mild acid. Figure 6.7a illustrates a simple experiment that was carried out to explore the stability of pristine nanobelts and laser treated nanobelts towards exposure to mild acid (HCl). A pre-pruned sample ($CdS_{0.73}Se_{0.27}$ with a 'Tai Chi' micropattern, the fluorescence microscope image as shown in Figure 6.7d) was fixed on top of a glass beaker with 5 ml diluted HCl with a concentration of about 10%. After a short exposure (5 seconds) to the HCl vapor, the sample was collected and imaged by fluorescence microscope again. The corresponding fluorescence microscope image after exposure to HCl is presented in Figure 6.7e. Evidently, the contrast of the FM image improved significantly after acid exposure. Figures 6.7b and c display the PL spectra of pristine and pruned regions before and after acid exposure, respectively. Clearly, the PL emission peaks of both the laser pruned

and pristine regions did not show any peak shift. Instead, the dominant change for the spectra is that the output intensity of pristine region shows an obvious decrease after acid treatment. Evidently pristine nanobelts are much more susceptible to acid corrosion. As for the laser pruned region, the output intensity of the spectra did not show a significant decrease. With both pristine and laser pruned regions fluoresced at comparable intensity, the contrast of the image naturally becomes

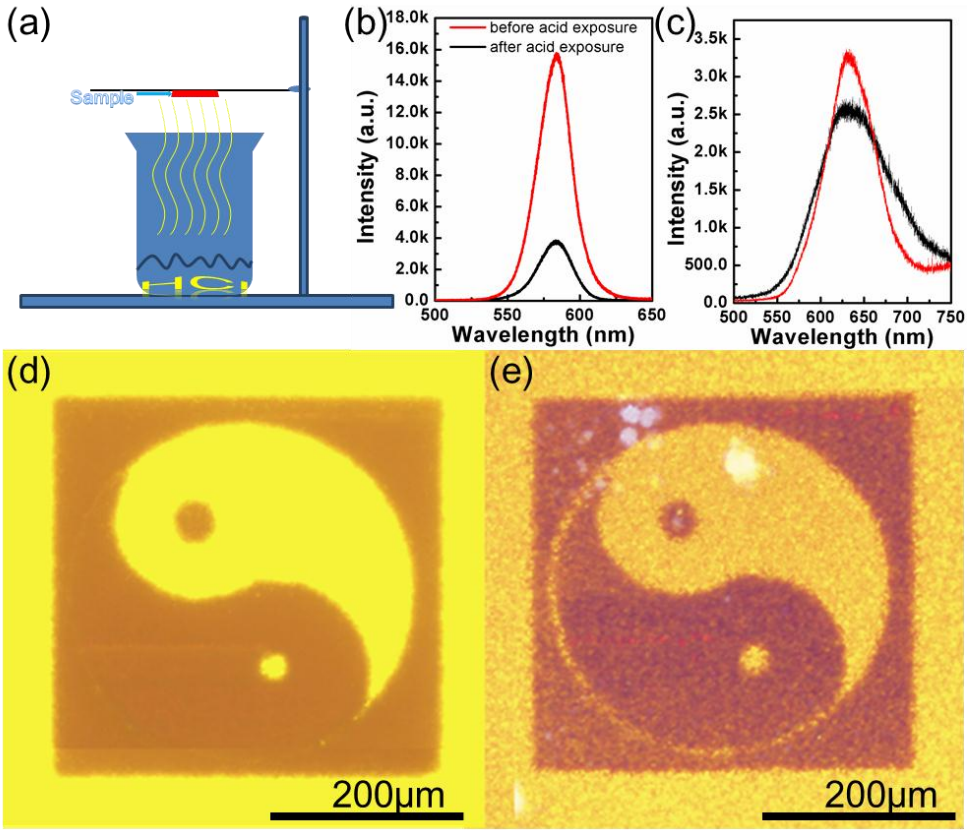

Figure 6.7 (a) Schematic of the set-up for the studies on acid-exposure . PL spectra of (b) pristine and (c) pruned region before and after acid exposure. Fluorescence microscope images of a micro-Tai Chi pattern (d) before and (e) after acid exposure.

better. Such an attribute could be further exploited to develop the patterned nanobelts as potential acid sensors.

Besides the alteration in the optical properties, changes in the functionalities of the laser pruned nanobelts are also found in their electrical and photoelectrical properties. A significant increase in film conductivity is observed as a result of the laser pruning induced nanobelts modification as well as improved nanobelt to nanobelt contact. Figure 6.8a shows the typical *I—V* curves for the pristine nanobelts and the laser pruned nanobelts. Evidently, the pristine nanobelts are poor conductors. We detected only a small current of ~ 2.7×10^{-10} A through the sample at an applied voltage of 5.0 V. However, after laser pruning, the sample showed a significant increase in conductivity. We measured a current of 1.3×10^{-8} A at an applied voltage of 5.0 V. These results shed light on the potential for a simple one-step, maskless, and in situ lithographic method for creating selective conducting domain. Beside a clear difference in conductivity, the pristine nanobelts and laser pruned nanobelts also exhibit marked difference in photocurrent. Figure 6.8b and c show the typical *I—V* curves of CdS_xSe_{1-x} nanobelts before and after laser pruning under broad beam laser illumination (1 mW, λ= 660nm). Both samples exhibit increased output current under illumination, indicating their obvious photoresponse to 660 nm laser light. However, the laser pruned sample shows a higher photo-responsivity than pristine nanobelts. Figure 6.8f presents the on/off photocurrent response corresponding to the laser illumination at 5 V bias under ambient condition. A rapid and prominent photoresponse is observed for both samples with the on/off laser illumination. The

photocurrent of pristine nanobelts increased 5 times compared to that measured at dark condition. However, under the same illumination condition, the laser pruned sample exhibits 10 times increasing in current, as show in Figure 6.8f (green curve). Beyond the response to visible spectrum light, the laser pruned nanobelts also exhibit sensitive response to infrared light. Figure 6.8d and e display typical *I—V* curves of pristine and pruned nanobelts under 1 mW 808 nm laser illumination. Evidently, pristine sample does not show any change in the output current while the output current of pruned nanobelts increases dramatically. As shown in Figure 6.8g, the pruned sample (brown curve) exhibits a rapid and prominent on/off photoresponse to 808 nm laser at 5 V bias, while the current passing through the pristine sample remains constant under the same irradiation and bias condition. The higher photo-responsivity of the pruned nanobelts could be attributed to the change of the optical property after laser pruning. The red-shift in the PL of the nanobelts is suggestive of a material that exhibits better photoresponse near to the wavelength of illumination (660nm and 808 nm). This demonstrates the enhanced photoelectrical properties of laser pruned CdS_xSe_{1-x} nanobelts and indicates their potential in optoelectronic applications such as photo-switching and wavelength selective photo-sensors.

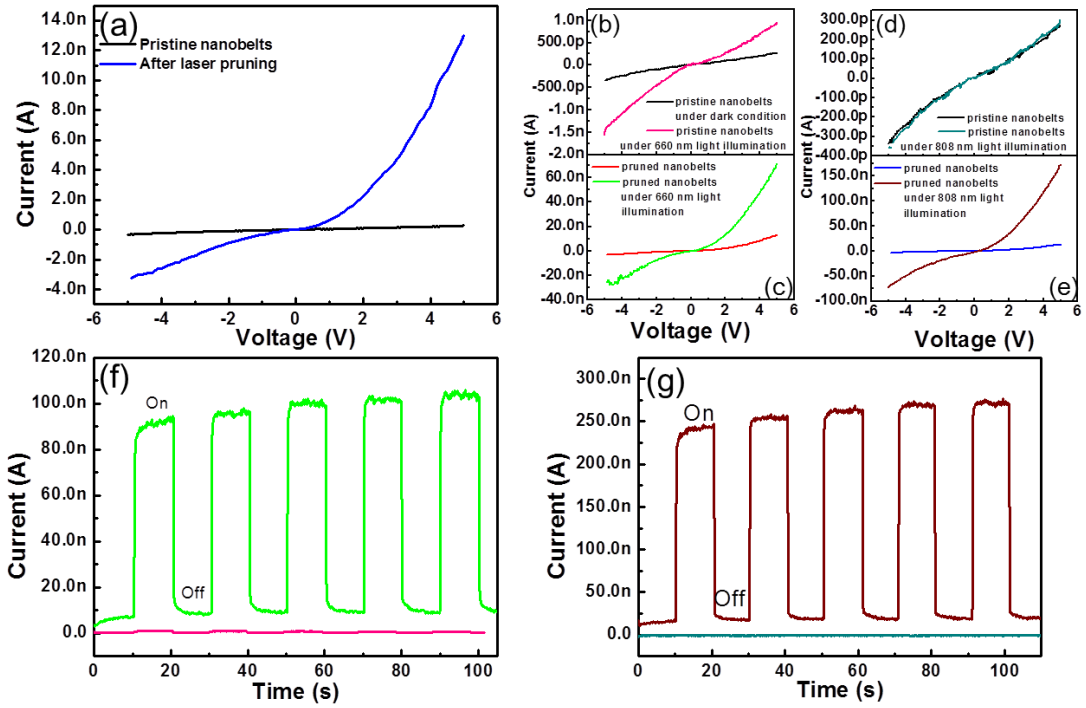

Figure 6.8 (a) Typical *I*—*V* curves acquired with two-probe measurements for the pristine nanobelts film and its laser pruned counterpart. Typical *I*—*V* curves under 660 nm laser irradiation of (b) pristine and (c) pruned nanobelts film. Typical *I*—*V* curves under 808 nm laser irradiation of (d) pristine and (e) pruned nanobelts film. (f) On/off photocurrent response of pristine nanobelts (pink curve) and laser pruned nanobelts (green curve) to 660 nm laser. (g) On/off photocurrent response of pristine nanobelts (light blue curve) and laser pruned nanobelts (brown curve) to 808 nm laser.

6.4 Conclusions

In summary, we have presented an inherently efficient and high throughput approach to directly create multicolored micro patterns on CdS_xSe_{1-x} nanobelt

samples. Well defined and high resolution micro structures are achievable *via* a simple focused laser beam. In addition, precise control over the fluorescence emissions of the nanobelts is another important attribute that can be achieved with this effective technique. The result is a chemical modification in the nanobelts compositions that alters the physical characteristics of the nanobelts and also provides a mechanism for patterning with multicolored domain. Moreover, followed by careful tuning of the laser power, fluorescence emissions of samples are readily controlled. As a result, multicolored display with a reasonably wide range of controlled color at selected location can be created on the ternary CdS_xSe_{1-x} nanobelt film. The laser modified nanobelts showed higher resistance to corrosion by acid and exhibited more superior photoconductivity. This effective approach is anticipated to be applicable to other ternary compounds as well.

Chapter 7

Conclusions and Future Works

In this work, we have developed simple and efficient growth methods to synthesize ternary II-VI 1D nanostructures of cadmium chalcogenide, zinc chalcogenide, and their hybrid complex structures. The physical properties of these as-grown ternary nanostructures were characterized and correlated with the binary compounds. The fundamentals of the optical properties have been investigated with varying chemical composition *x*. The appropriate potential applications have been optimized and demonstrated. In this chapter, brief conclusions extracted from the results presented in this work will be summarized and some possible future works will be proposed.

7.1 Summary

7.1.1 Synthesis of Nanostructured Ternary Zinc and Cadmium Chalcogenides

The ternary alloyed CdS_xSe_{1-x} nanobelts were synthesized by a facile one-step CVD method. A special modification was developed to remove the temperature gradient influence on the uniformity of the ternary composition. This approach enables the synthesis of high quality single crystalline CdS_xSe_{1-x} nanobelts with controlled composition. This method has been demonstrated to be applicable on synthesis of other ternary II-VI 1D nanostructures. The ZnS_xSe_{1-x} nanowires with uniform and controlled composition were also successfully synthesized *via* the same method. Vertically aligned ZnO/CdS_xSe_{1-x} core/shell

nanowire arrays were prepared by the second deposition of CdS_xSe_{1-x} shells on pre-grown ZnO nanowire arrays *via* a VS deposition route. The shells were synthesized with uniform and controlled composition and the composition could be tuned from CdS to CdSe by changing the molar ratio of source powders. In addition, complex CdS_xSe_{1-x} nanostructures with the composition gradient along the single nanobelt growth direction were synthesized by a specially designed source movable CVD approach. Along the length of a single CdS_xSe_{1-x} nanobelt, the chemical composition can be continuously controlled from CdS at the bottom end to CdSe at the top end *via* CdS_xSe_{1-x} at the middle part.

7.1.2 Investigation of Optical Properties

The fundamentals of optical properties of the ternary nanostructures have been investigated in steady state and non-equilibrium state, respectively. The different steady state optical mechanisms of the CdS_xSe_{1-x} nanobelts and ZnS_xSe_{1-x} nanowirs whilst the optical property dependence on the composition were studied by the characterization tools of temperature dependent PL spectroscopy, micro-Raman spectroscopy, and THz-TDS spectroscopy. The ultrafast and quasi-particle carrier dynamics at non-equilibrium states of CdS_xSe_{1-x} nanobelts were investigated by the time-resolved PL spectroscopy and OPTP spectroscopy. The composition-dependent complex photoconductivity of these nanobelts was probed by the TRTS spectroscopy. The ternary CdS_xSe_{1-x} nanobelts were demonstrated with much higher photoconductivity than that of binary CdS and CdSe nanobelts.

7.1.3 Demonstration of Potential Applications

The nanoscaled FETs and photodetector devices fabricated from ternary II-VI 1D nanostructures of CdS_xSe_{1-x} nanobelts and ZnS_xSe_{1-x} nanowires have been demonstrated. Large-scale nano-network devices were fabricated by a direct contact printing method. The CdS_xSe_{1-x} nanonet-FET exhibited better performance than that of binary CdS and CdSe. The ternary FETs were measured with lower threshold voltage and higher on/off ratio. The CdS_xSe_{1-x} nanonet based photodetectors showed faster response rate and higher responsivity to the normal and weak white light. The ZnS_xSe_{1-x} nanonet-FET was tested with higher conductivity and significantly enhanced gate effect as compared with the binary ZnS and ZnSe nanowires, whilst the ternary nanonets showed higher photoresponse capability than the binary compounds.

7.1.4 Modified Properties and Versatility

A simple focused laser beam setup was developed and employed to create well defined and high resolution micro-patterns on CdS_xSe_{1-x} nanobelt samples. The micro-patterns could be prepared with multicolors by carefully tuning the laser power. Therefore, multicolored display with controlled color at selective location can be fabricated on ternary CdS_xSe_{1-x} nanobelt film. On top of the modified properties, the laser pruned nanobelts showed higher resistance to corrosion by acid and exhibited higher photoconductivity than pristine nanobelts. This efficient approach is expected to be appropriate on other ternary nanostructures as well.

7.2 Further Works

7.2.1 Extension of Growth

The growth of ternary cadmium and zinc chalcogenides nanostructures by one-step or two-step vapor phase routes was realized in this work. The one-step chemical vapor deposition approach assisted with the special modification can be further employed to synthesize other type of ternary II-VI nanostructures such as lead chalcogenides and copper chalcogenides. Two-step method could be extended to the synthesis of the core/shell nanostructure arrays of ZnO/ZnS_xSe_{1-x} nanowires, TiO_2/CdS_xSe_{1-x} nanowires, and TiO_2/ZnS_xSe_{1-x} nanowires. We have obtained encouraging preliminary results on synthesis of ZnO/ZnS_xSe_{1-x} nanowire and TiO_2/CdS_xSe_{1-x} nanowire arrays. The aim of the growth is to promote the application potentials and improve the unique physical properties of ternary 1D nanostructures.

7.2.2 Investigation of Optical Property and Potential Applications of Complex Nanostructures

The fundamentals of optical properties in CdS_xSe_{1-x} nanobelts have been systematically investigated in this work. Similarly, the optical properties of ZnS_xSe_{1-x} nanowires can be investigated in detail due to the different band gap range as compared to the CdS_xSe_{1-x}. When more ternary II-VI 1D nanostructures such as PbS_xSe_{1-x} nanowires are synthesized, extended applications based on these ternary nanostructures can be explored and demonstrated due to the extension of the band gaps and corresponding broader wavelength respond range.

ZnS_xSe_{1-x} nanowires and CdS_xSe_{1-x} nanobelts cover the wavelength response from UV to NIR. PbS_xSe_{1-x} nanostructures can extend the response range from NIR to MIR and even FIR. This will greatly facilitate the application potential of these nanostructures in optoelectronic devices. On top of this, it is worthwhile to further investigate the optical properties shown by hybrid complex nanostructures. After the formation of hybrid nanostructures, type-I or type-II junctions will be fabricated due to their band gap and band energy alignment. The type-I junction can promote the fluorescence and light emitter yield of the nanostructures, whilst the type-II junction can facilitate the separation of the electron-hole pairs and thus improve the light-electron energy conversion efficiency. After the optical properties are understood *via* the systematical investigation, these hybrid nanostructures can be appropriately applied in various optoelectronic areas. The type-I hybrid structures can be used as the platform for light-emitting devices such as LEDs, lasers and LDs. Type-II hybrid nanostructures can be employed as the building-blocks for energy conversion devices such as photodetectors and solar cells.

7.2.3 Extension of the Modification by Laser Pruning

The focused laser beam method can also be put into effect on the hybrid complex nanostructures to realize more interesting optical properties and extended functions. We have obtained encouraging preliminary results on the laser modification of ZnO/CdS_xSe_{1-x} core/shell nanostructures. These modified nanowires showed a broader tunable color ranges due to the formation of quaternary of ZnCdSSe or even pentabasic ZnCdOSSe nanostructures. Using this

laser pruning method on the hybrid nanostructures, near white light fluorescence is expected to be realized. In this case, the white light LED can be achieved in the practical applications.

BIBLIOGRAPHY

[1]. Yuan, G. D.; Zhang, W. J.; Jie, J. S.; Fan, X.; Zapien, J. A.; Leung, Y. H.; Luo, L. B.; Wang, P. F.; Lee, C. S.; Lee, S. T. *Nano Letters* **2008,** 8, 2591-2597.

[2]. Wang, J.; Gudiksen, M. S.; Duan, X.; Cui, Y.; Lieber, C. M. *Science* **2001,** 293, 1455-1457.

[3]. Tian, B.; Zheng, X.; Kempa, T. J.; Fang, Y.; Yu, N.; Yu, G.; Huang, J.; Lieber, C. M. *Nature* **2007,** 449, 885-889.

[4]. Wang, Z. L.; Song, J. *Science* **2006,** 312, 242-246.

[5]. Wang, X.; Song, J.; Liu, J.; Wang, Z. L. *Science* **2007,** 316, 102-105.

[6]. Lieber, C. M. *Solid State Communications* **1998,** 107, 607-616.

[7]. Wei, L.; Charles, M. L. *Journal of Physics D: Applied Physics* **2006,** 39, R387.

[8]. Xia, Y.; Yang, P.; Sun, Y.; Wu, Y.; Mayers, B.; Gates, B.; Yin, Y.; Kim, F.; Yan, H. *Advanced Materials* **2003,** 15, 353-389.

[9]. Yang, P.; Wu, Y.; Fan, R. *International Journal of Nanoscience* **2002,** 01, 1-39.

[10]. Lieber, C. M.; Wang, Z. L. *MRS Bulletin* **2007,** 32, 99-108.

[11]. Law, M.; Goldberger, J.; Yang, P. *Annual Review of Materials Research* **2004,** 34, 83-122.

[12]. Holmes, J. D.; Johnston, K. P.; Doty, R. C.; Korgel, B. A. *Science* **2000,** 287, 1471-1473.

[13]. Zhao, X.; Wei, C. M.; Yang, L.; Chou, M. Y. *Physical Review Letters* **2004,** 92, 236805.

[14]. Peng, H.; Li, J. *The Journal of Physical Chemistry C* **2008,** 112, 20241-20245.

[15]. Beckman, S. P.; Han, J.; Chelikowsky, J. R. *Physical Review B* **2006,** 74, 165314.

[16]. Black, M. R.; Lin, Y. M.; Cronin, S. B.; Rabin, O.; Dresselhaus, M. S. *Physical Review B* **2002,** 65, 195417.

[17]. Huang, M. H.; Mao, S.; Feick, H.; Yan, H.; Wu, Y.; Kind, H.; Weber, E.; Russo, R.; Yang, P. *Science* **2001,** 292, 1897-1899.

[18]. Choi, H.-J.; Johnson, J. C.; He, R.; Lee, S.-K.; Kim, F.; Pauzauskie, P.; Goldberger, J.; Saykally, R. J.; Yang, P. *The Journal of Physical Chemistry B* **2003,** 107, 8721-8725.

[19]. Duan, X.; Huang, Y.; Agarwal, R.; Lieber, C. M. *Nature* **2003,** 421, 241-245.

[20]. Zhong, X.; Han, M.; Dong, Z.; White, T. J.; Knoll, W. *Journal of the American Chemical Society* **2003,** 125, 8589-8594.

[21]. Bailey, R. E.; Nie, S. *Journal of the American Chemical Society* **2003,** 125, 7100-7106.

[22]. Jie, J.; Zhang, W.; Bello, I.; Lee, C.-S.; Lee, S.-T. *Nano Today* **2010,** 5, 313-336.

[23]. Zhai, T.; Fang, X.; Li, L.; Bando, Y.; Golberg, D. *Nanoscale* **2010,** 2, 168-187.

[24]. Yang, P.; Yan, H.; Mao, S.; Russo, R.; Johnson, J.; Saykally, R.; Morris, N.; Pham, J.; He, R.; Choi, H. J. *Advanced Functional Materials* **2002,** 12, 323-331.

[25]. Kar, S.; Chaudhuri, S. *Synthesis and Reactivity in Inorganic, Metal-Organic, and Nano-Metal Chemistry* **2006,** 36, 289-312.

[26]. Zhong Lin, W. *Journal of Physics: Condensed Matter* **2004,** 16, R829.

[27]. Fang, X.; Wu, L.; Hu, L. *Advanced Materials* **2011,** 23, 585-598.

[28]. Fang, X.; Zhang, L. *Journal of Materials Science and Technology* **2006,** 22, 721-736.

[29]. Zhuang, X.; Ning, C. Z.; Pan, A. *Advanced Materials* **2012,** 24, 13-33.

[30]. Wagner, R. S.; Treuting, R. G. *Journal of Applied Physics* **1961,** 32, 2490-2491.

[31]. Wagner, R. S.; Ellis, W. C. *Applied Physics Letters* **1964,** 4, 89-90.

[32]. Wu, Y.; Yang, P. *Journal of the American Chemical Society* **2001,** 123, 3165-3166.

[33]. Tan, T. Y.; Li, N.; Gosele, U. *Applied Physics Letters* **2003,** 83, 1199-1201.

[34]. Li, N.; Tan, T. Y.; Gösele, U. *Applied Physics A* **2007,** 86, 433-440.

[35]. Choi, Y. C.; Kim, W. S.; Park, Y. S.; Lee, S. M.; Bae, D. J.; Lee, Y. H.; Park, G. S.; Choi, W. B.; Lee, N. S.; Kim, J. M. *Advanced Materials* **2000,** 12, 746-750.

[36]. Guha, P.; Chakrabarti, S.; Chaudhuri, S. *Physica E: Low-dimensional Systems and Nanostructures* **2004,** 23, 81-85.

[37]. Han, S.; Li, C.; Liu, Z.; Lei, B.; Zhang, D.; Jin, W.; Liu, X.; Tang, T.; Zhou, C. *Nano Letters* **2004,** 4, 1241-1246.

[38]. Johnson, M. C.; Aloni, S.; McCready, D. E.; Bourret-Courchesne, E. D. *Crystal Growth & Design* **2006,** 6, 1936-1941.

[39]. Huang, M. H.; Wu, Y.; Feick, H.; Tran, N.; Weber, E.; Yang, P. *Advanced Materials* **2001,** 13, 113-116.

[40]. Zhang, J.; Jiang, F.; Yang, Y.; Li, J. *The Journal of Physical Chemistry B* **2005,** 109, 13143-13147.

[41]. Wang, Y.; Meng, G.; Zhang, L.; Liang, C.; Zhang, J. *Chemistry of Materials* **2002,** 14, 1773-1777.

[42]. Ma, C.; Wang, Z. L. *Advanced Materials* **2005,** 17, 2635-2639.

[43]. Wang, Y.; Zhang, L.; Liang, C.; Wang, G.; Peng, X. *Chemical Physics Letters* **2002,** 357, 314-318.

[44]. Li, Q.; Gong, X.; Wang, C.; Wang, J.; Ip, K.; Hark, S. *Advanced Materials* **2004,** 16, 1436-1440.

[45]. Moon, S. R.; Kim, J. H.; Kim, Y. *The Journal of Physical Chemistry C* **2012,** 116, 10368-10374.

[46]. Pan, A.; Yang, H.; Liu, R.; Yu, R.; Zou, B.; Wang, Z. *Journal of the American Chemical Society* **2005,** 127, 15692-15693.

[47]. Liu, Y.; Zapien, J. A.; Shan, Y. Y.; Geng, C. Y.; Lee, C. S.; Lee, S. T. *Advanced Materials* **2005,** 17, 1372-1377.

[48]. Venugopal, R.; Lin, P.-I.; Chen, Y.-T. *The Journal of Physical Chemistry B* **2006,** 110, 11691-11696.

[49]. Na, C. W.; Han, D. S.; Kim, D. S.; Kang, Y. J.; Lee, J. Y.; Park, J.; Oh, D. K.; Kim, K. S.; Kim, D. *The Journal of Physical Chemistry B* **2006,** 110, 6699-6704.

[50]. Fan, H. J.; Scholz, R.; Kolb, F. M.; Zacharias, M. *Applied Physics Letters* **2004,** 85, 4142-4144.

[51]. Zhu, Y.-C.; Bando, Y. *Chemical Physics Letters* **2003,** 377, 367-370.

[52]. Utama, M. I. B.; Peng, Z.; Chen, R.; Peng, B.; Xu, X.; Dong, Y.; Wong, L. M.; Wang, S.; Sun, H.; Xiong, Q. *Nano Letters* **2010,** 11, 3051-3057.

[53]. Lau, Y. K. A.; Chernak, D. J.; Bierman, M. J.; Jin, S. *Journal of the American Chemical Society* **2009,** 131, 16461-16471.

[54]. Bierman, M. J.; Lau, Y. K. A.; Jin, S. *Nano Letters* **2007,** 7, 2907-2912.

[55]. Pan, J.; Utama, M. I. B.; Zhang, Q.; Liu, X.; Peng, B.; Wong, L. M.; Sum, T. C.; Wang, S.; Xiong, Q. *Advanced Materials* **2012,** 24, 4151-4156.

[56]. Morales, A. M.; Lieber, C. M. *Science* **1998,** 279, 208-211.

[57]. Son, H. J.; Jeon, K. A.; Kim, C. E.; Kim, J. H.; Yoo, K. H.; Lee, S. Y. *Applied Surface Science* **2007,** 253, 7848-7850.

[58]. Meng, X. M.; Liu, J.; Jiang, Y.; Chen, W. W.; Lee, C. S.; Bello, I.; Lee, S. T. *Chemical Physics Letters* **2003,** 382, 434-438.

[59]. Jiang, Y.; Meng, X.-M.; Yiu, W.-C.; Liu, J.; Ding, J.-X.; Lee, C.-S.; Lee, S.-T. *The Journal of Physical Chemistry B* **2004,** 108, 2784-2787.

[60]. Duan, X.; Lieber, C. M. *Advanced Materials* **2000,** 12, 298-302.

[61]. Zapien, J. A.; Liu, Y. K.; Shan, Y. Y.; Tang, H.; Lee, C. S.; Lee, S. T. *Applied Physics Letters* **2007,** 90, 213114-3.

[62]. Liu, Y. K.; Zapien, J. A.; Shan, Y. Y.; Tang, H.; Lee, C. S.; Lee, S. T. *Nanotechnology* **2007,** 18, 365606.

[63]. Park, W. I.; Kim, D. H.; Jung, S. W.; Yi, G.-C. *Applied Physics Letters* **2002,** 80, 4232-4234.

[64]. Shan, C. X.; Liu, Z.; Hark, S. K. *Applied Physics Letters* **2005,** 87, 163108-3.

[65]. Li, Z.; Salfi, J.; De Souza, C.; Sun, P.; Nair, S. V.; Ruda, H. E. *Applied Physics Letters* **2010,** 97, 063510-3.

[66]. Zhang, X. T.; Liu, Z.; Leung, Y. P.; Li, Q.; Hark, S. K. *Applied Physics Letters* **2003,** 83, 5533-5535.

[67]. Wang, Z.; Liu, X.; Gong, J.; Huang, H.; Gu, S.; Yang, S. *Crystal Growth & Design* **2008,** 8, 3911-3913.

[68]. Liang, Y.; Xu, H.; Hark, S. *Crystal Growth & Design* **2010,** 10, 4206-4210.

[69]. Zhang, Z.; Wang, S. J.; Yu, T.; Wu, T. *The Journal of Physical Chemistry C* **2007,** 111, 17500-17505.

[70]. Nguyen, P.; Ng, H. T.; Meyyappan, M. *Advanced Materials* **2005,** 17, 1773-1777.

[71]. Wang, W.; Summers, C. J.; Wang, Z. L. *Nano Letters* **2004,** 4, 423-426.

[72]. Dai, Z. R.; Pan, Z. W.; Wang, Z. L. *Advanced Functional Materials* **2003,** 13, 9-24.

[73]. Blakely, J. M.; Jackson, K. A. *The Journal of Chemical Physics* **1962,** 37, 428-430.

[74]. Pan, Z. W.; Dai, Z. R.; Wang, Z. L. *Science* **2001,** 291, 1947-1949.

[75]. Zhou, J.; Xu, N. S.; Deng, S. Z.; Chen, J.; She, J. C.; Wang, Z. L. *Advanced Materials* **2003,** 15, 1835-1840.

[76]. Wang, Z. L. *Advanced Materials* **2003,** 15, 432-436.

[77]. Zhou, J.; Ding, Y.; Deng, S. Z.; Gong, L.; Xu, N. S.; Wang, Z. L. *Advanced Materials* **2005,** 17, 2107-2110.

[78]. Chueh, Y. L.; Lai, M. W.; Liang, J. Q.; Chou, L. J.; Wang, Z. L. *Advanced Functional Materials* **2006,** 16, 2243-2251.

[79]. Zhao, Y. M.; Li, Y. H.; Ahmad, I.; McCartney, D. G.; Zhu, Y. Q.; Hu, W. B. *Applied Physics Letters* **2006,** 89, 133116-3.

[80]. Zhou, J.; Deng, S. Z.; Xu, N. S.; Chen, J.; She, J. C. *Applied Physics Letters* **2003,** 83, 2653-2655.

[81]. Lilach, Y.; Zhang, J.-P.; Moskovits, M.; Kolmakov, A. *Nano Letters* **2005,** 5, 2019-2022.

[82]. Li, J.; Li, H. *Nanoscale Research Letters* **2008,** 4, 165 - 168.

[83]. Shen, G.; Bando, Y.; Golberg, D.; Zhou, C. *The Journal of Physical Chemistry C* **2008,** 112, 12299-12303.

[84]. Lin, Y.-F.; Song, J.; Ding, Y.; Lu, S.-Y.; Wang, Z. L. *Advanced Materials* **2008,** 20, 3127-3130.

[85]. Wang, Z. L.; Kong, X. Y.; Zuo, J. M. *Physical Review Letters* **2003,** 91, 185502.

[86]. Shen, G.; Chen, D.; Lee, C. J. *The Journal of Physical Chemistry B* **2006,** 110, 15689-15693.

[87]. Xu, H.; Liang, Y.; Liu, Z.; Zhang, X.; Hark, S. *Advanced Materials* **2008,** 20, 3294-3297.

[88]. Myung, Y.; Jang, D. M.; Sung, T. K.; Sohn, Y. J.; Jung, G. B.; Cho, Y. J.; Kim, H. S.; Park, J. *ACS Nano* **2010,** 4, 3789-3800.

[89]. Li, C.; Fang, G.; Liu, N.; Li, J.; Liao, L.; Su, F.; Li, G.; Wu, X.; Zhao, X. *The Journal of Physical Chemistry C* **2007,** 111, 12566-12571.

[90]. Fang, F.; Zhao, D. X.; Zhang, J. Y.; Shen, D. Z.; Lu, Y. M.; Fan, X. W.; Li, B. H.; Wang, X. H. *Nanotechnology* **2007,** 18, 235604.

[91]. Ho, S.-T.; Chen, K.-C.; Chen, H.-A.; Lin, H.-Y.; Cheng, C.-Y.; Lin, H.-N. *Chemistry of Materials* **2007,** 19, 4083-4086.

[92]. Ajayan, P. M.; Stephan, O.; Redlich, P.; Colliex, C. *Nature* **1995,** 375, 564-567.

[93]. Nagashima, K.; Yanagida, T.; Tanaka, H.; Seki, S.; Saeki, A.; Tagawa, S.; Kawai, T. *Journal of the American Chemical Society* **2008,** 130, 5378-5382.

[94]. Huang, X.; Wang, M.; Willinger, M.-G.; Shao, L.; Su, D. S.; Meng, X.-M. *ACS Nano* **2012,** 6, 7333-7339.

[95]. Chang, K.-W.; Wu, J.-J. *The Journal of Physical Chemistry B* **2005,** 109, 13572-13577.

[96]. Yang, Y.; Sun, X. W.; Tay, B. K.; Wang, J. X.; Dong, Z. L.; Fan, H. M. *Advanced Materials* **2007,** 19, 1839-1844.

[97]. Jin fan, H.; Knez, M.; Scholz, R.; Nielsch, K.; Pippel, E.; Hesse, D.; Zacharias, M.; Gosele, U. *Nat Mater* **2006,** 5, 627-631.

[98]. Zhang, Y.; Ram, M. K.; Stefanakos, E. K.; Goswami, D. Y. *Journal of Nanomaterials* **2012,** 2012, 22.

[99]. Chun, J.; Lee, J. *European Journal of Inorganic Chemistry* **2010,** 2010, 4251-4263.

[100]. Hu, Q. R.; Wang, S. L.; Jiang, P.; Xu, H.; Zhang, Y.; Tang, W. H. *Journal of Alloys and Compounds* **2010,** 496, 494-499.

[101]. Yu, H.; Li, J.; Loomis, R. A.; Gibbons, P. C.; Wang; Buhro, W. E. *Journal of the American Chemical Society* **2003,** 125, 16168-16169.

[102]. Grebinski, J. W.; Hull, K. L.; Zhang, J.; Kosel, T. H.; Kuno, M. *Chemistry of Materials* **2004,** 16, 5260-5272.

[103]. Hull, K. L.; Grebinski, J. W.; Kosel, T. H.; Kuno, M. *Chemistry of Materials* **2005,** 17, 4416-4425.

[104]. Wang, F.; Dong, A.; Sun, J.; Tang, R.; Yu, H.; Buhro, W. E. *Inorganic Chemistry* **2006,** 45, 7511-7521.

[105]. Onicha, A. C.; Petchsang, N.; Kosel, T. H.; Kuno, M. *ACS Nano* **2012,** 6, 2833-2843.

[106]. Law, M.; Greene, L. E.; Johnson, J. C.; Saykally, R.; Yang, P. *Nat Mater* **2005,** 4, 455-459.

[107]. Yue, G. H.; Yan, P. X.; Yan, D.; Fan, X. Y.; Wang, M. X.; Qu, D. M.; Liu, J. Z. *Applied Physics A* **2006,** 84, 409-412.

[108]. Bazarganipour, M.; Salavati-Niasari, M. *Micro & Nano Letters, IET* **2012,** 7, 388-391.

[109]. Lin, Y.-F.; Song, J.; Ding, Y.; Lu, S.-Y.; Wang, Z. L. *Applied Physics Letters* **2008,** 92, 022105-3.

[110]. Zhao, L.; Hu, L.; Fang, X. *Advanced Functional Materials* **2012,** 22, 1551-1566.

[111]. Yong, S.-M.; Muralidharan, P.; Jo, S. H.; Kim, D. K. *Materials Letters* **2010,** 64, 1551-1554.

[112]. Zhang, X.; Dai, J.; Ong, H. *Open Journal of Physical Chemistry* **2011,** 1.

[113]. Han, D.; Song, C.; Li, X. *Journal of Nanomaterials* **2010,** 2010.

[114]. Li, Y.; Meng, G. W.; Zhang, L. D.; Phillipp, F. *Applied Physics Letters* **2000,** 76, 2011-2013.

[115]. Ding, J. X.; Zapien, J. A.; Chen, W. W.; Lifshitz, Y.; Lee, S. T.; Meng, X. M. *Applied Physics Letters* **2004,** 85, 2361-2363.

[116]. Routkevitch, D.; Bigioni, T.; Moskovits, M.; Xu, J. M. *The Journal of Physical Chemistry* **1996,** 100, 14037-14047.

[117]. Xu, D.; Shi, X.; Guo, G.; Gui, L.; Tang, Y. *The Journal of Physical Chemistry B* **2000,** 104, 5061-5063.

[118]. Zhao, A. W.; Meng, G. W.; Zhang, L. D.; Gao, T.; Sun, S. H.; Pang, Y. T. *Applied Physics A* **2003,** 76, 537-539.

[119]. Hujdic, J. E.; Taggart, D. K.; Kung, S.-C.; Menke, E. J. *The Journal of Physical Chemistry Letters* **2010,** 1, 1055-1059.

[120]. Yang, Y.; Kung, S. C.; Taggart, D. K.; Xiang, C.; Yang, F.; Brown, M. A.; Güell, A. G.; Kruse, T. J.; Hemminger, J. C.; Penner, R. M. *Nano Letters* **2008,** 8, 2447-2451.

[121]. Kumar, S.; Vohra, A.; Chakarvarti, S. K. *Journal of Materials Science: Materials in Electronics* **2012,** 23, 1485-1491.

[122]. Shi, L.; Pei, C.; Li, Q. *CrystEngComm* **2010,** 12, 3882-3885.

[123]. Yoffe, A. D. *Advances in Physics* **2002,** 51, 799-890.

[124]. Yu, H.; Li, J.; Loomis, R. A.; Wang, L.-W.; Buhro, W. E. *Nat Mater* **2003,** 2, 517-520.

[125]. Zhang, Z.; Sun, X.; Dresselhaus, M. S.; Ying, J. Y.; Heremans, J. *Physical Review B* **2000,** 61, 4850-4861.

[126]. Nanda, K. K.; Kruis, F. E.; Fissan, H. *Nano Letters* **2001,** 1, 605-611.

[127]. Hu, Z.; Fischbein, M. D.; Querner, C.; Drndić, M. *Nano Letters* **2006,** 6, 2585-2591.

[128]. Smith, P. A.; Nordquist, C. D.; Jackson, T. N.; Mayer, T. S.; Martin, B. R.; Mbindyo, J.; Mallouk, T. E. *Applied Physics Letters* **2000,** 77, 1399-1401.

[129]. Liu, X.; Li, C.; Han, S.; Han, J.; Zhou, C. *Applied Physics Letters* **2003,** 82, 1950-1952.

[130]. Fan, Z.; Lu, J. G. *Applied Physics Letters* **2005,** 86, 032111-3.

[131]. Long, Y.; Chen, Z.; Wang, W.; Bai, F.; Jin, A.; Gu, C. *Applied Physics Letters* **2005,** 86, 153102-3.

[132]. Maeng, J.; Jo, G.; Kwon, S.-S.; Song, S.; Seo, J.; Kang, S.-J.; Kim, D.-Y.; Lee, T. *Applied Physics Letters* **2008,** 92, 233120-3.

[133]. Hong, W.-K.; Sohn, J. I.; Hwang, D.-K.; Kwon, S.-S.; Jo, G.; Song, S.; Kim, S.-M.; Ko, H.-J.; Park, S.-J.; Welland, M. E.; Lee, T. *Nano Letters* **2008,** 8, 950-956.

[134]. Duan, X.; Niu, C.; Sahi, V.; Chen, J.; Parce, J. W.; Empedocles, S.; Goldman, J. L. *Nature* **2003,** 425, 274-278.

[135]. Ma, R.-M.; Dai, L.; Qin, G.-G. *Nano Letters* **2007,** 7, 868-873.

[136]. Li, G.; Jiang, Y.; Wang, Y.; Wang, C.; Sheng, Y.; Jie, J.; Zapien, J. A.; Zhang, W.; Lee, S.-T. *The Journal of Physical Chemistry C* **2009,** 113, 17183-17188.

[137]. Djurišić, A. B.; Leung, Y. H. *Small* **2006,** 2, 944-961.

[138]. Yan, R.; Gargas, D.; Yang, P. *Nat Photon* **2009,** 3, 569-576.

[139]. Yang, P.; Yan, R.; Fardy, M. *Nano Letters* **2010,** 10, 1529-1536.

[140]. Chen, R.; Bakti Utama, M. I.; Peng, Z.; Peng, B.; Xiong, Q.; Sun, H. *Advanced Materials* **2011,** 23, 1404-1408.

[141]. van Vugt, L. K.; Piccione, B.; Cho, C.-H.; Aspetti, C.; Wirshba, A. D.; Agarwal, R. *The Journal of Physical Chemistry A* **2011,** 115, 3827-3833.

[142]. GuoZhang, D.; QingLin, Z.; ZhiWei, P.; WeiChang, Z.; MingXia, X.; Qiang, W.; AnLian, P.; BingSuo, Z. *Journal of Physics D: Applied Physics* **2008,** 41, 135301.

[143]. Utama, M. I. B.; Zhang, J.; Chen, R.; Xu, X.; Li, D.; Sun, H.; Xiong, Q. *Nanoscale* **2012,** 4, 1422-1435.

[144]. Woggon, U.; Hild, K.; Gindele, F.; Langbein, W.; Hetterich, M.; Grün, M.; Klingshirn, C. *Physical Review B* **2000,** 61, 12632-12635.

[145]. Tran, T. K.; Park, W.; Tong, W.; Kyi, M. M.; Wagner, B. K.; Summers, C. J. *Journal of Applied Physics* **1997,** 81, 2803-2809.

[146]. Sun, H. D.; Makino, T.; Tuan, N. T.; Segawa, Y.; Kawasaki, M.; Ohtomo, A.; Tamura, K.; Koinuma, H. *Applied Physics Letters* **2001,** 78, 2464-2466.

[147]. Pan, A.; Liu, R.; Wang, F.; Xie, S.; Zou, B.; Zacharias, M.; Wang, Z. L. *The Journal of Physical Chemistry B* **2006,** 110, 22313-22317.

[148]. Shafiq, I.; Sharif, A.; Sing, L. C. *Physica E: Low-dimensional Systems and Nanostructures* **2009,** 41, 739-745.

[149]. Fang, Z.; Huang, S.; Lu, Y.; Pan, A.; Lin, F.; Zhu, X. *Physical Review B* **2010,** 82, 085403.

[150]. Pan, A.; Wang, X.; He, P.; Zhang, Q.; Wan, Q.; Zacharias, M.; Zhu, X.; Zou, B. *Nano Letters* **2007,** 7, 2970-2975.

[151]. Liao, L.; Yan, B.; Hao, Y. F.; Xing, G. Z.; Liu, J. P.; Zhao, B. C.; Shen, Z. X.; Wu, T.; Wang, L.; Thong, J. T. L.; Li, C. M.; Huang, W.; Yu, T. *Applied Physics Letters* **2009,** 94, 113106-3.

[152]. Fang, X.; Bando, Y.; Liao, M.; Zhai, T.; Gautam, U. K.; Li, L.; Koide, Y.; Golberg, D. *Advanced Functional Materials* **2010,** 20, 500-508.

[153]. Lin, D. D.; Wu, H.; Pan, W. *Advanced Materials* **2007,** 19, 3968-3972.

[154]. Fang, X.; Bando, Y.; Liao, M.; Gautam, U. K.; Zhi, C.; Dierre, B.; Liu, B.; Zhai, T.; Sekiguchi, T.; Koide, Y.; Golberg, D. *Advanced Materials* **2009,** 21, 2034-2039.

[155]. Fang, X.; Xiong, S.; Zhai, T.; Bando, Y.; Liao, M.; Gautam, U. K.; Koide, Y.; Zhang, X.; Qian, Y.; Golberg, D. *Advanced Materials* **2009,** 21, 5016-5021.

[156]. Jiang, Y.; Zhang, W. J.; Jie, J. S.; Meng, X. M.; Fan, X.; Lee, S. T. *Advanced Functional Materials* **2007,** 17, 1795-1800.

[157]. Zhai, T.; Fang, X.; Liao, M.; Xu, X.; Zeng, H.; Yoshio, B.; Golberg, D. *Sensors* **2009,** 9, 6504-6529.

[158]. Young-Jin, C.; Kyung-Soo, P.; Jae-Gwan, P. *Nanotechnology* **2010,** 21, 505605.

[159]. Toshitake, T.; Patricia, N.; Kuniharu, T.; Alexandra, C. F.; Arash, J.; Ming, C. W.; Ning, C. Z.; Ali, J. *Nanotechnology* **2012,** 23, 045201.

[160]. Wong, J. I.; Yang, H. Y.; Li, H.; Chen, T.; Fan, H. J. *Nanoscale* **2012,** 4, 1467-1470.

[161]. Lee, J.-C.; Kim, T. G.; Lee, W.; Han, S.-H.; Sung, Y.-M. *Crystal Growth & Design* **2009,** 9, 4519-4523.

[162]. Caselli, D. A.; Ning, C. Z. *Optics Express* **2011,** 19, A686-A694.

[163]. Yao, B. D.; Chan, Y. F.; Wang, N. *Applied Physics Letters* **2002,** 81, 757-759.

[164]. Auston, D. H.; Cheung, K. P.; Valdmanis, J. A.; Kleinman, D. A. *Physical Review Letters* **1984,** 53, 1555-1558.

[165]. Fattinger, C.; Grischkowsky, D. *Applied Physics Letters* **1988,** 53, 1480-1482.

[166]. Han, J.; Wan, F.; Zhu, Z.; Liao, Y.; Ji, T.; Ge, M.; Zhang, Z. *Applied Physics Letters* **2005,** 87, 172107-3.

[167]. Kador, L. *Applied Physics Letters* **1995,** 66, 2938-2939.

[168]. Lim, K. Y.; Sow, C. H.; Lin, J.; Cheong, F. C.; Shen, Z. X.; Thong, J. T. L.; Chin, K. C.; Wee, A. T. S. *Advanced Materials* **2003,** 15, 300-303.

[169]. Lim, X.; Zhu, Y.; Cheong, F. C.; Hanafiah, N. M.; Valiyaveettil, S.; Sow, C.-H. *ACS Nano* **2008,** 2, 1389-1395.

[170]. Lu, S. H.; Ni Tun, M. H.; Mei, Z. J.; Chia, G. H.; Lim, X.; Sow, C.-H. *Langmuir* **2009,** 25, 12806-12811.

[171]. Lim, X.; Foo, H. W. G.; Chia, G. H.; Sow, C.-H. *ACS Nano* **2010,** 4, 1067-1075.

[172]. Lu, J.; Lim, X.; Zheng, M.; Mhaisalkar, S. G.; Sow, C.-H. *ACS Nano* **2012,** 6, 8298-8307.

[173]. Zhou, Y.; Bao, Q.; Varghese, B.; Tang, L. A. L.; Tan, C. K.; Sow, C.-H.; Loh, K. P. *Advanced Materials* **2010,** 22, 67-71.

[174]. Wang, M.; Fei, G. T.; Zhang, Y. G.; Kong, M. G.; Zhang, L. D. *Advanced Materials* **2007,** 19, 4491-4494.

[175]. Cooley, B. J.; Clark, T. E.; Liu, B. Z.; Eichfeld, C. M.; Dickey, E. C.; Mohney, S. E.; Crooker, S. A.; Samarth, N. *Nano Letters* **2009,** 9, 3142-3146.

[176]. Bhattacharyya, S.; Perelshtein, I.; Moshe, O.; Rich, D. H.; Gedanken, A. *Advanced Functional Materials* **2008,** 18, 1641-1653.

[177]. Kuno, M. *Physical Chemistry Chemical Physics* **2008,** 10, 620-639.

[178]. Yao, W.-T.; Yu, S.-H. *Advanced Functional Materials* **2008,** 18, 3357-3366.

[179]. Givargizov, E. I. *Journal of Crystal Growth* **1975,** 31, 20-30.

[180]. Seifert, W.; Borgström, M.; Deppert, K.; Dick, K. A.; Johansson, J.; Larsson, M. W.; Mårtensson, T.; Sköld, N.; Patrik T. Svensson, C.; Wacaser, B.

A.; Reine Wallenberg, L.; Samuelson, L. *Journal of Crystal Growth* **2004,** 272, 211-220.

[181]. Kodambaka, S.; Tersoff, J.; Reuter, M. C.; Ross, F. M. *Physical Review Letters* **2006,** 96, 096105.

[182]. Dubrovskii, V. G.; Sibirev, N. V.; Harmand, J. C.; Glas, F. *Physical Review B* **2008,** 78, 235301.

[183]. Young-Jin, C.; In-Sung, H.; Jae-Hwan, P.; Sahn, N.; Jae-Gwan, P. *Nanotechnology* **2006,** 17, 3775.

[184]. Pan, A.; Zhou, W.; Leong, E. S. P.; Liu, R.; Chin, A. H.; Zou, B.; Ning, C. Z. *Nano Letters* **2009,** 9, 784-788.

[185]. Vegard, L. *Zeitschrift für Physik* **1921,** 5, 17-26.

[186]. Lu, J.; Liu, H.; Sun, C.; Zheng, M.; Nripan, M.; Chen, G. S.; Subodh, G. M.; Zhang, X.; Sow, C. H. *Nanoscale* **2012,** 4, 976-981.

[187]. Junpeng, L.; Cheng, S.; Minrui, Z.; Mathews, N.; Hongwei, L.; Gin Seng, C.; Xinhai, Z.; Mhaisalkar, S. G.; Chorng Haur, S. *The Journal of Physical Chemistry C* **2011,** 115, 19538-19545.

[188]. Pan, A.; Liu, R.; Sun, M.; Ning, C.-Z. *Journal of the American Chemical Society* **2009,** 131, 9502-9503.

[189]. Qian, F.; Li, Y.; Gradecak, S.; Park, H.-G.; Dong, Y.; Ding, Y.; Wang, Z. L.; Lieber, C. M. *Nat Mater* **2008,** 7, 701-706.

[190]. Agarwal, R. *Small* **2008,** 4, 1872-1893.

[191]. Goebl, J. A.; Black, R. W.; Puthussery, J.; Giblin, J.; Kosel, T. H.; Kuno, M. *Journal of the American Chemical Society* **2008,** 130, 14822-14833.

[192]. Ouyang, L.; Maher, K. N.; Yu, C. L.; McCarty, J.; Park, H. *Journal of the American Chemical Society* **2006,** 129, 133-138.

[193]. Shan, C. X.; Liu, Z.; Ng, C. M.; Hark, S. K. *Applied Physics Letters* **2005,** 87, 033108-3.

[194]. Hsu, H.-C.; Wu, C.-Y.; Cheng, H.-M.; Hsieh, W.-F. *Applied Physics Letters* **2006,** 89, 013101-3.

[195]. Kwon, S. J.; Choi, Y.-J.; Park, J.-H.; Hwang, I.-S.; Park, J.-G. *Physical Review B* **2005,** 72, 205312.

[196]. Lorenz, M.; Kaidashev, E. M.; Rahm, A.; Nobis, T.; Lenzner, J.; Wagner, G.; Spemann, D.; Hochmuth, H.; Grundmann, M. *Applied Physics Letters* **2005,** 86, 143113-3.

[197]. Persson, A. I.; Björk, M. T.; Jeppesen, S.; Wagner, J. B.; Wallenberg, L. R.; Samuelson, L. *Nano Letters* **2006,** 6, 403-407.

[198]. Yoon, Y.-J.; Park, K.-S.; Heo, J.-H.; Park, J.-G.; Nahm, S.; Choi, K. J. *Journal of Materials Chemistry* **2010,** 20, 2386-2390.

[199]. Mang, A.; Reimann, K.; Rübenacke, S. *Solid State Communications* **1995,** 94, 251-254.

[200]. Klingshirn, C., *Semiconductor Optics*. Springer: Berlin, 2007.

[201]. Lipari, N. O. *Physical Review B* **1971,** 4, 4535-4538.

[202]. Birman, J. L. *Physical Review Letters* **1959,** 2, 157-159.

[203]. Liang, W. Y.; Yoffe, A. D. *Physical Review Letters* **1968,** 20, 59-62.

[204]. Reynolds, D. C.; Look, D. C.; Jogai, B.; Litton, C. W.; Cantwell, G.; Harsch, W. C. *Physical Review B* **1999,** 60, 2340-2344.

[205]. Chichibu, S. F.; Tsukazaki, A.; Kawasaki, M.; Tamura, K.; Segawa, Y.; Sota, T.; Koinuma, H. *Applied Physics Letters* **2002,** 80, 2860-2862.

[206]. Sun, H. D.; Makino, T.; Tuan, N. T.; Segawa, Y.; Tang, Z. K.; Wong, G. K. L.; Kawasaki, M.; Ohtomo, A.; Tamura, K.; Koinuma, H. *Applied Physics Letters* **2000,** 77, 4250-4252.

[207]. Weisbuch, C.; Nishioka, M.; Ishikawa, A.; Arakawa, Y. *Physical Review Letters* **1992,** 69, 3314-3317.

[208]. van Vugt, L. K.; Piccione, B.; Cho, C.-H.; Nukala, P.; Agarwal, R. *Proceedings of the National Academy of Sciences* **2011**.

[209]. Perna, G.; Pagliara, S.; Capozzi, V.; Ambrico, M.; Pallara, M. *Solid State Communications* **2000,** 114, 161-166.

[210]. Hill, R. *Journal of Physics C: Solid State Physics* **1974,** 7, 521.

[211]. Adachi, S., *Properties of Semiconductor Alloys: Group-IV, III-V and II-VI Semiconductors*. A John Wiley and Sons, Ltd: Chichester, U.K., 2009.

[212]. Hill, R.; Richardson, D. *Journal of Physics C: Solid State Physics* **1973,** 6, L115.

[213]. Liu, H. W.; Lu, J. P.; Fan, H. M.; Sow, C. H.; Tang, S. H.; Zhang, X. H. *Journal of Applied Physics* **2012,** 111, 073112-6.

[214]. Imada, A.; Ozaki, S.; Adachi, S. *Journal of Applied Physics* **2002,** 92, 1793-1798.

[215]. Seto, S.; Kuroda, T.; Suzuki, K. *physica status solidi (c)* **2006,** 3, 803-806.

[216]. Seto, S. *Japanese Journal of Applied Physics* **2005,** 44, 5.

[217]. Thomas, D. G.; Hopfield, J. J. *Physical Review Letters* **1961,** 7, 316-319.

[218]. Thomas, D. G.; Hopfield, J. J. *Physical Review* **1962,** 128, 2135-2148.

[219]. Ip, K. M.; Wang, C. R.; Li, Q.; Hark, S. K. *Applied Physics Letters* **2004,** 84, 795-797.

[220]. Malloy, T. F. *ACS Nano* **2011,** 5, 5-12.

[221]. Gourdon, C.; Lavallard, P.; Dagenais, M. *Physical Review B* **1988,** 37, 2589-2593.

[222]. Hoang, T. B.; Titova, L. V.; Jackson, H. E.; Smith, L. M.; Yarrison-Rice, J. M.; Lensch, J. L.; Lauhon, L. J. *Applied Physics Letters* **2006,** 89, 123123-3.

[223]. Anderson, P. W. *Physical Review* **1958,** 109, 1492-1505.

[224]. Zhang, J.; Zhang, X.; Zhang, J. Y. *The Journal of Physical Chemistry C* **2009,** 113, 9512-9515.

[225]. Xu, X.; Chuang, K.; Nicholas, R. J.; Johnston, M. B.; Herz, L. M. *The Journal of Physical Chemistry C* **2009,** 113, 18106-18109.

[226]. Gadd, S. E. The Picosecond Dynamics of Electron-Hole Pairs in Graded and Homogeneous CdS_xSe_{1-x} Semiconductors. University of California, 1995.

[227]. Hane, J. K. The Picosecond Dynamics of Electron-Hole Pairs in Graded and Homogeneous CdS_xSe_{1-x} Semiconductors. University of California, 1995.

[228]. Hane, J. K.; Prisant, M. G.; Harris, C. B.; Meyer, G. J.; Leung, L. K.; Ellis, A. B. *The Journal of Physical Chemistry* **1989,** 93, 7975-7977.

[229]. Garrett, M. D.; Dukes Iii, A. D.; McBride, J. R.; Smith, N. J.; Pennycook, S. J.; Rosenthal, S. J. *The Journal of Physical Chemistry C* **2008,** 112, 12736-12746.

[230]. Schmuttenmaer, C. A. *Chemical Reviews* **2004,** 104, 1759-1780.

[231]. Cooke, D. G.; MacDonald, A. N.; Hryciw, A.; Wang, J.; Li, Q.; Meldrum, A.; Hegmann, F. A. *Physical Review B* **2006,** 73, 193311.

[232]. Baxter, J. B.; Schmuttenmaer, C. A. *The Journal of Physical Chemistry B* **2006,** 110, 25229-25239.

[233]. Parkinson, P.; Lloyd-Hughes, J.; Gao, Q.; Tan, H. H.; Jagadish, C.; Johnston, M. B.; Herz, L. M. *Nano Letters* **2007,** 7, 2162-2165.

[234]. Titova, L. V.; Hoang, T. B.; Jackson, H. E.; Smith, L. M.; Yarrison-Rice, J. M.; Kim, Y.; Joyce, H. J.; Tan, H. H.; Jagadish, C. *Applied Physics Letters* **2006,** 89, 173126.

[235]. Jepsen, P. U.; Schairer, W.; Libon, I. H.; Lemmer, U.; Hecker, N. E.; Birkholz, M.; Lips, K.; Schall, M. *Applied Physics Letters* **2001,** 79, 1291-1293.

[236]. Ulbricht, R.; Hendry, E.; Shan, J.; Heinz, T. F.; Bonn, M. *Reviews of Modern Physics* **2011,** 83, 543-586.

[237]. Liu, H.; Lu, J.; Teoh, H. F.; Li, D.; Feng, Y. P.; Tang, S. H.; Sow, C. H.; Zhang, X. *The Journal of Physical Chemistry C* **2012**.

[238]. Liao, Z.-M.; Lu, Y.; Xu, J.; Zhang, J.-M.; Yu, D.-P. *Applied Physics A: Materials Science & Processing* **2009,** 95, 363-366.

[239]. Rajesh, T.; Binni, V.; Subodh, G. M.; Eng Soon, T.; Chorng Haur, S. *Nanotechnology* **2011,** 22, 115202.

[240]. Mondal, S. P.; Ray, S. K. *Applied Physics Letters* **2009,** 94, 223119-3.

[241]. Soci, C.; Zhang, A.; Xiang, B.; Dayeh, S. A.; Aplin, D. P. R.; Park, J.; Bao, X. Y.; Lo, Y. H.; Wang, D. *Nano Letters* **2007,** 7, 1003-1009.

[242]. Beard, M. C.; Turner, G. M.; Schmuttenmaer, C. A. *Physical Review B* **2000,** 62, 15764-15777.

[243]. Smith, N. V. *Physical Review B* **2001,** 64, 155106.

[244]. Lu, J.; Sun, C.; Zheng, M.; Nripan, M.; Liu, H.; Chen, G. S.; Zhang, X.; Subodh G, M.; Sow, C. H. *The Journal of Physical Chemistry C* **2011,** 115, 19538-19545.

[245]. Kaindl, R. A.; Carnahan, M. A.; Hagele, D.; Lovenich, R.; Chemla, D. S. *Nature* **2003,** 423, 734-738.

[246]. Stroscio, M. A.; Dutta, M., *Phonons in Nanostructures*. Cambridge University Press: 2001.

[247]. Piscanec, S.; Cantoro, M.; Ferrari, A. C.; Zapien, J. A.; Lifshitz, Y.; Lee, S. T.; Hofmann, S.; Robertson, J. *Physical Review B* **2003,** 68, 241312.

[248]. Adu, K. W.; Gutiérrez, H. R.; Kim, U. J.; Sumanasekera, G. U.; Eklund, P. C. *Nano Letters* **2005,** 5, 409-414.

[249]. Fan, H. M.; Ni, Z. H.; Feng, Y. P.; Fan, X. F.; Kuo, J. L.; Shen, Z. X.; Zou, B. S. *Applied Physics Letters* **2007,** 91, 171911-3.

[250]. Rao, A. M.; Richter, E.; Bandow, S.; Chase, B.; Eklund, P. C.; Williams, K. A.; Fang, S.; Subbaswamy, K. R.; Menon, M.; Thess, A.; Smalley, R. E.; Dresselhaus, G.; Dresselhaus, M. S. *Science* **1997,** 275, 187-191.

[251]. Yoffe, A. D. *Advances in Physics* **2001,** 50, 1-208.

[252]. RAMAN, C. V.; KRISHNAN, K. S. *Nature* **1928,** 121, 2.

[253]. Weber, W. H.; Merlin, R., *Raman Scattering in Materials Science*. Springer: Berlin, 2000.

[254]. Nusimovici, M. A.; Birman, J. L. *Physical Review* **1967,** 156, 925-938.

[255]. Beserman, R. *Solid State Communications* **1977,** 23, 323-327.

[256]. Kotkata, M. F.; Masoud, A. E.; Mohamed, M. B.; Mahmoud, E. A. *Physica E: Low-dimensional Systems and Nanostructures* **2009,** 41, 640-645.

[257]. Mlayah, A.; Brugman, A. M.; Carles, R.; Renucci, J. B.; Valakh, M. Y.; Pogorelov, A. V. *Solid State Communications* **1994,** 90, 567-570.

[258]. Roy, A.; Sood, A. K. *Physical Review B* **1996,** 53, 12127-12132.

[259]. Liu, L.; Xiao-Liang, X.; Wen-Tao, L.; Hai-Fei, L. *Journal of Physics: Condensed Matter* **2007,** 19, 406221.

[260]. Sernelius, B. E., *Surface Modes in Physics*. Wiley-VCH: Berlin, 2001.

[261]. Gupta, R.; Xiong, Q.; Mahan, G. D.; Eklund, P. C. *Nano Letters* **2003,** 3, 1745-1750.

[262]. Vinogradov, E. A.; Mavrin, B. N.; Novikova, N. N.; Yakovlev, V. A. *Physics of the Solid State* **2006,** 48, 1940-1946.

[263]. Chang, I. F.; Mitra, S. S. *Physical Review* **1968,** 172, 924-933.

[264]. Jin, C. X.; Ling, Z.; Wang, D. H.; Huang, D. M.; Hou, X. Y.; Wang, X. *Journal of Applied Physics* **1997,** 81, 3465-3467.

[265]. Parayanthal, P.; Pollak, F. H. *Physical Review Letters* **1984,** 52, 1822-1825.

[266]. Yamamoto, K.; Yamaguchi, M.; Tani, M.; Hangyo, M.; Teramura, S.; Isu, T.; Tomita, N. *Applied Physics Letters* **2004,** 85, 5194-5196.

[267]. Walther, M.; Fischer, B.; Schall, M.; H; Jepsen, P. U. *Chemical Physics Letters* **2000,** 332, 389-395.

[268]. Walther, M.; Fischer, B. M.; Uhd Jepsen, P. *Chemical Physics* **2003,** 288, 261-268.

[269]. Schall, M.; Walther, M.; Uhd Jepsen, P. *Physical Review B* **2001,** 64, 094301.

[270]. Han, J.; Zhang, W.; Chen, W.; Thamizhmani, L.; Azad, A. K.; Zhu, Z. *The Journal of Physical Chemistry B* **2006,** 110, 1989-1993.

[271]. Parrish, J.; Perry, C. H.; Brafman, O.; Chang, I. F.; Mitra, S. S., *Proceedings of the International Conference on the Physics of II-VI Semiconductors*. W. A. Benjamin, Inc.: New York, 1967.

[272]. Lieber, C. M. *MRS Bulletin* **2003,** 28, 486-491.

[273]. Li, Y.; Qian, F.; Xiang, J.; Lieber, C. M. *Materials Today* **2006,** 9, 18-27.

[274]. Sze, S. M., *Physics of Semiconductor DeVices*. 2nd ed.; Wiley: New York, 1981.

[275]. Jie, J. S.; Zhang, W. J.; Jiang, Y.; Lee, S. T. *Applied Physics Letters* **2006,** 89, 223117-3.

[276]. Jie, J. S.; Zhang, W. J.; Jiang, Y.; Lee, S. T. *Applied Physics Letters* **2006,** 89, 133118-3.

[277]. Meitl, M. A.; Zhu, Z.-T.; Kumar, V.; Lee, K. J.; Feng, X.; Huang, Y. Y.; Adesida, I.; Nuzzo, R. G.; Rogers, J. A. *Nat Mater* **2006,** 5, 33-38.

[278]. Xia, Y.; Whitesides, G. M. *Journal of the American Chemical Society* **1995,** 117, 3274-3275.

[279]. Juwan, K.; Sung, M.; Byeongju, K.; Dongjin, O.; Gyu Tae, K.; Seunghun, H. *Nanotechnology* **2008,** 19, 095303.

[280]. Sun, C.; Mathews, N.; Zheng, M.; Sow, C. H.; Wong, L. H.; Mhaisalkar, S. G. *The Journal of Physical Chemistry C* **2009,** 114, 1331-1336.

[281]. Fan, Z.; Ho, J. C.; Jacobson, Z. A.; Yerushalmi, R.; Alley, R. L.; Razavi, H.; Javey, A. *Nano Letters* **2007,** 8, 20-25.

[282]. Dattoli, E. N.; Wan, Q.; Guo, W.; Chen, Y.; Pan, X.; Lu, W. *Nano Letters* **2007,** 7, 2463-2469.

[283]. Vineet, S.; Anup, T.; Goyal, N.; Saini, G. S. S.; Tripathi, S. K. *Semiconductor Science and Technology* **2005,** 20, 103.

[284]. Khurana, P.; Vohra, A.; Srivastava, K. K. *Journal of Materials Science: Materials in Electronics* **1990,** 1, 175-181.

[285]. Behl, M.; Seekamp, J.; Zankovych, S.; Sotomayor Torres, C. M.; Zentel, R.; Ahopelto, J. *Advanced Materials* **2002,** 14, 588-591.

[286]. Pisignano, D.; Persano, L.; Raganato, M. F.; Visconti, P.; Cingolani, R.; Barbarella, G.; Favaretto, L.; Gigli, G. *Advanced Materials* **2004,** 16, 525-529.

[287]. Sun, Y.; Liu, Y.; Zhu, D. *Journal of Materials Chemistry* **2005,** 15, 53-65.

[288]. Zhang, F.; Nyberg, T.; Inganäs, O. *Nano Letters* **2002,** 2, 1373-1377.

[289]. Huang, L.; Braunschweig, A. B.; Shim, W.; Qin, L.; Lim, J. K.; Hurst, S. J.; Huo, F.; Xue, C.; Jang, J.-W.; Mirkin, C. A. *Small* **2010,** 6, 1077-1081.

[290]. Aldred, M. P.; Contoret, A. E. A.; Farrar, S. R.; Kelly, S. M.; Mathieson, D.; O'Neill, M.; Tsoi, W. C.; Vlachos, P. *Advanced Materials* **2005,** 17, 1368-1372.

[291]. Bharathan, J.; Yang, Y. *Applied Physics Letters* **1998,** 72, 2660-2662.

[292]. Babentsov, V.; Riegler, J.; Schneider, J.; Ehlert, O.; Nann, T.; Fiederle, M. *Journal of Crystal Growth* **2005,** 280, 502-508.

[293]. Jing, P.; Zheng, J.; Ikezawa, M.; Liu, X.; Lv, S.; Kong, X.; Zhao, J.; Masumoto, Y. *The Journal of Physical Chemistry C* **2009,** 113, 13545-13550.

APPENDIX

List of publications:

(1) Lu Junpeng, Yun Tao, Zheng Minrui and Sow Chorng Haur, Enhanced field emission properties of α-Fe_2O_3 nanostructures with the removal of adsorbed gas molecules. Journal of Physical Chemistry C, Vol 115, page 8816-8824, 2011.

(2) Lu Junpeng, Sun Cheng, Zheng Minrui, Nripan Mathews, Liu Hongwei, Chen Gin Seng, Zhang Xinhai, Subodh G. Mhaisalkar, and Sow Chorng Haur, Facile one-step synthesis of CdS_xSe_{1-x} nanobelts with uniform and controllable stoichiometry, Journal of Physical Chemistry C, Vol 115, page 19538-19545, 2011.

(3) Lu Junpeng, Liu Hongwei, Sun Cheng, Zheng Minrui, Nripan Mathews, Chen Gin Seng, Subodh G. Mhaisalkar, Zhang Xinhai, and Sow Chorng Haur, Optical and electrical applications of ZnS_xSe_{1-x} nanowires-network with uniform and controllable stoichiometry, Nanoscale, Vol 4, page 976-981, 2012.

(4) Hu Zhibin, Zhou Chenggang, Zheng Minrui, Lu Junpeng, Varghese Binni, Cheng Hansong and Sow Chorng Haur, K-enriched MoO_3 nanobundles: a layered structure with high electric conductivity, Journal of Physical Chemistry C, Journal of Physical Chemistry C, Vol 116, page 3962-3967, 2012.

(5) Liu Hongwei, Lu Junpeng, Fan Haiming, Sow Chorng Haur, Tang Sing Hai, and Zhang Xinhai, Temperature and composition dependence of photoluminescence dynamics in CdS_xSe_{1-x} ($0 \leq x \leq 1$) nanobelts, Journal of Applied Physics, Vol 111, page 073112,2012.

(6) Lu Junpeng, Lim Xiaodai, Zheng Minrui and Sow Chorng Haur, Direct Laser Pruning of CdS_xSe_{1-x} Nanobelts en Route to a Multicolored Pattern with Controlled Functionalities, ACS Nano, Vol 6, page 8298-8307, 2012.

(7) Liu Hongwei, Sun Cheng, Lu Junpeng, Zheng Minrui, Lim Kim Yong, Nripan Mathews, Subodh G. Mhaisalkar, Tang Sing Hai, Zhang Xinhai, and Sow

Chorng Haur, Electrical property characterization of Sb-doped SnO_2 nanonets via contact and non-contact approaches, RSC Advances, Vol 2, page 9590-9595 ,2012. (co-first author)

(8) Lu Junpeng, Sun Cheng, Zheng Minrui, Wang Yinghui, Nripan Mathews, Jeroen van Kan, Subodh G. Mhaisalkar and Sow Chorng Haur, Ultra-sensitive phototransistor based on K-enriched MoO_3 single-wires, Journal of Physical Chemistry C, Vol 116, page 22015-22020, 2012.

(9) Liu Hongwei, Lu Junpeng, Tang Sing Hai, Sow Chorng Haur, Zhang Xinhai, Defect engineering in CdS_xSe_{1-x} nanobelts: an insight into carrier relaxation dynamics via optical pump-terahertz probe spectroscopy, Journal of Physical Chemistry C, Vol 116, page 26036-26042, 2012. (co-first author)

(10) Zhang Zheng, Lu Junpeng, Yun Tao, Zheng Minrui, Pan Jisheng, Sow Chorng Haur and Tok Eng Soon, Desorption of Ambient Gas Molecules and Phase Transformation of α-Fe_2O_3 Nanostructures during Ultrahigh Vacuum Annealing, Journal of Physical Chemistry C, Vol 117, page 1509-1517, 2013.

(11) Liu Hongwei, Lu Junpeng, Tang Sing Hai, Sow Chorng Haur, and Zhang Xinhai, Terahertz spectroscopic study of topological insulator Bi_2Se_3 microcrystals and nanowires, submitted. (co-first author)

(12) Lu Junpeng, Liu Hongwei, Lim Xiaodai Tang Sing Hai, Sow Chorng Haur, Zhang Xinhai, Transient Photoconductivity of Ternary CdSSe nanobelts as measured by Time-Resolved Terahertz Spectroscopy, Journal of Physical Chemistry C, Vol 117, page 12379-12384, 2013.

(13) Lu Junpeng, Liu Hongwei, Zheng Minrui Tang Sing Hai, Sow Chorng Haur, Zhang Xinhai, Composition-Dependent Ultra-high Photoconductivity in Ternary CdS_xSe_{1-x} Nanobelts as Measured by Optical Pump-Terahertz Probe Spectroscopy, Nano Research, accepted.

(14) Liu Hongwei, Lu Junpeng, Tang Sing Hai, Sow Chorng Haur, and Zhang Xinhai, Composition dependence electron transport in CdS_xSe_{1-x} nanobelts: A

study using THz time-domain spectroscopy, to be submitted. (co-first author)

(15) Sun Cheng, Lu Junpeng, Nripan Mathews, Lydia H. Wong, Sow Chorng Haur and Subodh G. Mhaisalkar, The improvement of large-scale tin oxide nanonet transistors with antimony doping, to be submitted.

(16) Lu Junpeng, Liu Hongwei, Deng Suzi, Zheng Minrui, Wang Yinghui, van Kan, Jeroen, Tang Sing Hai, Zhang Xinhai, and Sow Chorng Haur, High-sensitive and multispectral responsive phototransistor using tungsten-doped VO_2 nanowires, to be submitted.

(17) Lu Junpeng, Liu Hongwei, Tang Sing Hai, Zhang Xinhai and Sow Chorng Haur, Ternary II-VI 1D nanostructures: synthesis, properties, and applications, to be submitted.

(18) Lu Junpeng, Liu Hongwei, Lim Xiaodai, Zheng Minrui, Zhang Xinhai and Sow Chorng Haur, A facile laser modification of ZnO-CdS_xSe_{1-x} core-shell nanowire arrays with improved optical properties en route to high-performance 3D photodetectors, to be submitted.

(19) Liu Hongwei, Lu Junpeng, Tang Sing Hai, Sow Chorng Haur, Zhang Xinhai, Unambiguous identification of recombination lines in ZnSSe nanowires, to be submitted. (co-first author)